Phreatic eruptions and the influence of hydrothermal alteration on their processes

Klaus Mayer

München 2016

This page was intentionally left blank

Phreatic eruptions and the influence of hydrothermal alteration on their processes

Klaus Mayer

Dissertation

an der Fakultät für Geowissenschaften

der Ludwig–Maximilians–Universität

München

vorgelegt von

Klaus Mayer

aus Vilsbiburg (Deutschland)

München, den 2. März 2016

This page was intentionally left blank.

Erstgutachter: PD. Dr. Bettina Scheu

Zweitgutachter: Prof. Dr. Donald B. Dingwell

Tag der mündlichen Prüfung: 25.07.2016

This page was intentionally left blank.

Abstract

Phreatic eruptions are possibly the most drastic surface expressions of hydrothermal activity within active epithermal systems (geothermal fields), and they are still poorly understood. Various phenomena, such as fumaroles, hot springs, mud pools, and soil encrustations represent further obvious features of the interaction between outgassing hydrothermal fluids and the host rocks. Investigation of rocks outcropping in the proximity of such phenomena aimed to provide insights concerning the effects of hydrothermal alteration on phreatic eruption dynamics within volcanic systems.

This dissertation presents the results of three individual case studies focusing on the influence of surficial hydrothermal alteration on petrophysical properties and in turn on phreatic eruption processes. Key question is, whether alteration increases the potential for such eruptions or not. Based on the findings of this study hydrothermal alteration changes the rock physical and mechanical properties and can have major effects on the permeability of surficial lithologies. The observed degradation processes were successfully related to the degree of alteration, which is represented by chemical weathering indices. The precipitation of secondary minerals and the formation of clay minerals can lead to the development of a mineralogical seal and a low permeable cap rock, respectively. Both processes might hinder the outgassing and favor the pressurization within the subsurface. Depending on the composition and temperature of fluids as well as on host rock composition and permeability, alteration can also be dominated by mineral dissolution resulting in an increased outgassing. The observed variability in alteration processes within very similar geological and hydrothermal settings highlights the complexity involved in the dynamics of hydrothermal systems. Furthermore the results showed that secondary mineralization induced by hydrothermal alteration might have a significant effect on the dynamics of phreatic eruptions and on the nature of phreatic ejecta. Surge deposits intensely affected by solfataric alteration generate abundant fine particles during fragmentation. Very fine ash, which possesses a silica- and alumina-rich composition due to alteration, may be a causative agent of respiratory diseases, and its dispersion could represent a serious health hazard on a local scale.

In addition to the effects of hydrothermal alteration this study furthermore highlighted the influence of fluid type (liquid vs. gaseous) within the pore space on the phreatic eruption dynamics. Under identical pressure and temperature conditions, eruptions accompanied by the process of liquid water flashing to steam are significantly more violent than those driven simply by gas or steam expansion.

Phase changes during decompression together with the type and degree of alteration are important fragmentation variables. Therefore they should be considered for hazard assessment and modeling of phreatic eruptions in hydrothermally active environments.

Kurzfassung

Phreatische Ausbrüche zählen zu den drastischsten Auswirkungen von hydrothermaler Tätigkeit in aktiven, epithermalen Regionen (Geothermalfelder). Weitere offensichtliche Merkmale der Wechselwirkungen zwischen austretenden hydrothermalen Fluiden und dem Nebengestein sind Fumarolen, heiße Quellen, Schlammlöcher und Bodeninkrustationen. Um Einblicke in den Vulkanismus, vor allem in die wenig erforschten Prozesse der phreatischen Ausbrüche zu bekommen, wurden die Gesteine in der nahen Umgebung solcher Erscheinungsbilder untersucht.

Im Rahmen dieser Dissertation werden die Ergebnisse aus drei eigenständigen Fallstudien vorgestellt. Untersucht wurden die Auswirkungen oberflächlicher, hydrothermaler Alteration auf gesteinsphysikalische Eigenschaften und folglich auf die Prozesse phreatischer Ausbrüche. Dabei stellt sich die Kernfrage, ob Alteration die Wahrscheinlichkeit derartiger Ausbrüche erhöht, oder nicht. Als Ergebnis dieser Studie kann festgehalten werden, dass hydrothermale Alteration die gesteinsphysikalischen und mechanischen Eigenschaften verändert sowie eine bedeutende Auswirkung auf die Permeabilität oberflächennaher Gesteine haben kann. Zusätzlich ist es gelungen, die Verschlechterung der Gesteinseigenschaften mit dem Grad der Alteration in Zusammenhang zu bringen, welcher von chemischen Verwitterungsindizes abgeleitet werden konnte. Die Ausfällung von Sekundärmineralen sowie die Bildung von Tonmineralen kann zur Ausbildung eines dichten Gesteinsverbandes bzw. einer geringdurchlässigen Deckschicht führen. Diese beiden Prozesse können die Entgasung behindern und damit zu einer Druckerhöhung im Untergrund führen. Alteration kann hingegen, abhängig von der Zusammensetzung und der Temperatur der Fluide, sowie des Mineralbestands und der Permeabilität des Nebengesteins, auch eine maßgebliche Lösung von Mineralen bewirken, was wiederum zu einer Erhöhung der Durchlässigkeit führen kann. Die Variabilität der Alterationsprozesse innerhalb sehr ähnlicher geologischer und hydrothermaler Umgebungen zeigt die Komplexität hydrothermaler Systeme und deren Abläufe auf. Des Weiteren verdeutlichen die Resultate, dass die Sekundärmineralisation signifikante Auswirkungen auf die Ausbruchsdynamik und die Eigenschaften phreatischer Auswurfmassen hat. Pyroklastische Dichtestromablagerungen, die intensiv von solfatarischer Alteration betroffen sind und fragmentiert werden, erzeugen eine immense Menge an Feinpartikeln. Sehr feine Aschepartikel, welche aufgrund der Alteration reich an Siliziumdioxid und/oder Aluminium sind, können Erkrankungen der Atemwege hervorrufen. Daher kann deren Freisetzung eine ernsthafte gesundheitliche Gefährdung im der Umgebung des Ausbruchs darstellen.

Zusätzlich zu den Auswirkungen hydrothermaler Alteration wurden die Einflüsse des Fluidtyps (flüssig bzw. gasförmig) im Porenraum, auf die Dynamik phreatischer Ausbrüche untersucht. Ausbrüche bei denen es zu explosionsartigem Verdampfen von überhitztem Wasser kommt, sind bedeutend energetischer als jene, die lediglich von Gas- oder Dampfausdehnung getrieben werden – Voraussetzung ist die Annahme identischer Druck- und Temperaturbedingungen.

Sowohl der Phasenübergang von Fluiden bei der Dekompression, als auch der Typ und Grad der Alteration, sind wichtige Parameter der Fragmentation. Daher sollten sie bei der Gefährdungsbeurteilung sowie der Modellierung von phreatischen Ausbrüchen in hydrothermalen Gebieten, berücksichtigt werden.

Preamble

Most of the content of this doctoral dissertation has been published in scientific journals, is in the state of a submitted manuscript in review, or in preparation for submission to a scientific journal. Detailed references are listed below. Modifications have only slightly been made, mainly in terms of formatting and style for incorporation into a consistent overall thesis design.

Mayer, K., Scheu, B., Gilg, H.A., Heap, M.J., Kennedy, B.M., Lavallée, Y., Letham-Brake, M., Dingwell, D.B. (2015). Experimental constraints on phreatic eruption processes at Whakaari (White Island volcano). Journal of Volcanology and Geothermal Research, 302, 150-162.

Mayer, K., Scheu, B., Montanaro, C., Yilmaz, T.I., Isaia, R., Aßbichler, D., Dingwell, D.B. Influence of hydrothermal alteration on phreatic eruption processes in Solfatara (Campi Flegrei). Journal of Volcanology and Geothermal Research (in review).

Mayer, K., Scheu, B., Yilmaz, T.I., Rott, S., Gilg, H.A., Dingwell, D.B. Phreatic activity in the Valley of Desolation, Dominica (Lesser Antilles) – estimates from field and lab investigations to experimental volcanology. Solid Earth (manuscript in preparation).

Heap, M.J., Kennedy, B.M., Pernin, N., Jacquemard, L., Baud, P., Farquharson, J.I., Scheu, B., Lavallée, Y., Gilg, H.A., Letham-Brake, M., Mayer, K., Jolly, A.D., Reuschlé, T., Dingwell, D.B., 2015. Mechanical behaviour and failure modes in the Whakaari (White Island volcano) hydrothermal system, New Zealand. Journal of Volcanology and Geothermal Research, 295, 26-42.

Carlino, S., Piochi, M., Tramelli, A., Troise, C., Mormone, A., Montanaro, C., Scheu, B., Mayer, K., Somma, R., De Natale, G. Small-to-large scale permeability and continuous gradient temperature monitoring of subsurface rocks in volcanic areas: new insights from borehole and laboratory analysis at the Campi Flegrei caldera (Southern Italy). International Journal of Rock Mechanics and Mining Sciences (in review).

Acknowledgements

Table of contents

List of figures

List of tables

1 Introduction

Figure 1.1: Surface expressions of hydrothermal activity in different environments.

This page was intentionally left blank.

1.1   Phreatic eruptions

Phreatic eruptions are one of the most common but also the least predictable type of eruptive volcanism (Barberi et al., 1992; Smith and McKibbin, 2000; Mastin, 1995). These eruptions are instigated by the direct input of mass and heat of magmatic origin, even though magma itself is not involved, and by definition only non-juvenile rock is ejected (Browne and Lawless, 2001). Several other terms have also been introduced to describe this type of eruption based on particular eruption and trigger mechanisms (Barberi et al., 1992; Browne and Lawless, 2001; Mastin, 1995). The most common nomenclature includes hydrothermal, steam-blast, boiling-point, and hydro-explosions (Barberi et al., 1992; Smith, 2000), but the meanings of the individual terms vary within the literature (Browne and Lawless, 2001; Fullard, 2011; Hardy, 2005). Therefore, a clear definition seems to be necessary to avoid further confusion.

Within this study, the term ˈ*phreatic eruption*ˈ is used for any eruptive event caused by the rapid expansion of mainly water in liquid or gas phase at shallow depth (Figure 1.2).
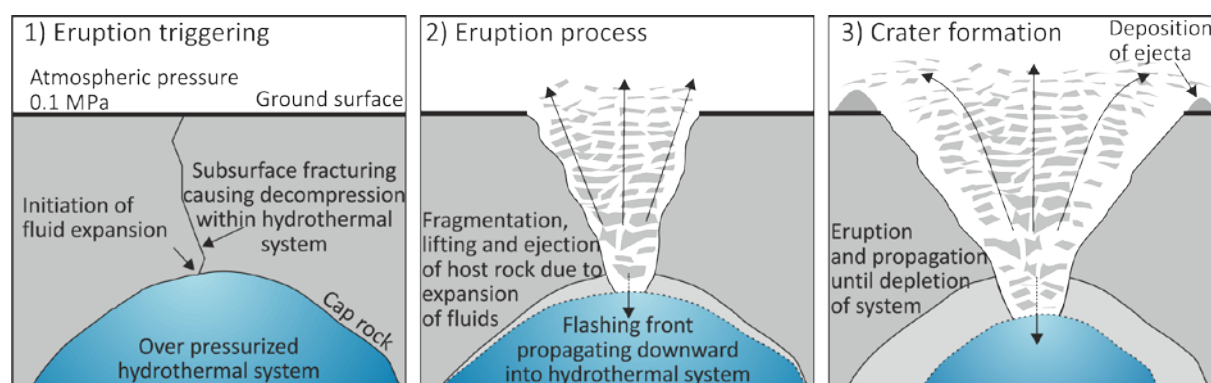
Figure 1.2: Simplified model for a phreatic eruption. 1) Initiation of fluid expansion and decompression triggered by subsurface pressure release. 2) Fragmentation and ejection during downward propagation of flashing front. 3) Crater formation and deposition of ejecta until depletion of the system (modified after Foote, 2011).

Phreatic eruptions often associated with confined hydrothermal systems (geothermal fields) occur due to the accumulation of fluids below a low-permeability cap rock (Barberi et al., 1992). The resulting pressure build-up can be caused by progressive self-sealing of the covering rock or by an increased fluid supply, which eventually exceeds the dissipation by permeable outgassing (Barberi et al., 1992; Wohletz and Heiken, 1992; Mastin, 1995; Brown and Lawless, 2001; Nairn et al., 2004). If an effective outgassing of the hydrothermal system is hindered, the resulting pressurization increases until the pressure in the system exceeds the sum of lithostatic and atmospheric pressure, and the tensile strength of the overlying rocks (Browne and Lawless, 2001; Seki et al., 2015; Montanaro et al., 2016). The rupture of the capping layer, and consequently a rapid decompression causing an eruption is inevitable.

Thus, brecciating and ejection of the overburden material will occur (Nelson and Giles, 1985; Browne and Lawless, 2001).

Several mechanisms have been suggested to trigger systems primed for phreatic eruptions. Earthquakes and minor seismic activity may produce pathways for upward migration of fluids, which in turn increases the pressure within the system (Barberi et al., 1992; Bixley and Browne, 1988; Smith, 2000; Browne and Lawless, 2001). Moreover, rapid decompression can be triggered by various processes reducing the pressure counteracting that within the system, such as a sudden drop in atmospheric pressure, landslides, or lake drainages (Barberi et al., 1992; Browne and Lawless, 2001; Montanaro et al., 2016). Decompression caused by drilling conducted within geothermal fields, may also lead to eruptions (Bixley and Browne, 1988; Hedenquist and Henley, 1985).

Even though, phreatic eruptions do not eject a large volume of tephra (<10^5 m^3, Browne and Lawless, 2001), they are frequently more violent than magmatic or phreatomagmatic eruptions (ejection velocity >130 m/s, Mastin, 1995; Kilgour et al., 2010; Rouwet and Morrissey, 2015). The duration and crater dimensions may vary depending on the amount of fluid and on the properties of the host rocks involved (Handal and Barrios, 2004). Phreatic tephra is composed of host-rock fragments, often characterized by signs of alteration and ranging in size from fine ash up to large blocks (Barberi et al., 1992). As this type of eruption is usually attributed by an absence of precursory signals, phreatic eruptions are almost unpredictable with respect to both time and magnitude (Barberi et al., 1992; Bromley and Mongillo, 1994; Hurst et al., 2014). Phreatic eruptions therefore can represent major hazards (Morgan et al., 2009; Foote et al., 2012).

Several studies have been conducted, which focused on I) physical characteristics of eruption deposits (Hedenquist and Henley, 1985; Collar and Browne, 1985; Morgan et al., 2009), II) analytical modelling of the eruption processes (Smith and McKibbin, 2000; Mastin, 2001; Thiéry and Mercury, 2009; Fullard, 2011; Fullard and Lynch, 2012), and III) experimental modelling of the physics driving phreatic eruptions (Rager et al., 2014; Mayer et al., 2015; Montanaro et al., 2016). Even though, these studies provide valuable information, further research is necessary to deepen the understanding in the dynamics of these violent and hazardous eruptions (e.g. to investigate the influence of hydrothermal alteration on phreatic eruptions).

1.2   Hydrothermal alteration

Hydrothermal alteration is a common feature observed in geothermal systems, which are defined by the distribution of laterally and vertically circulating fluids at variably elevated temperatures (~50 to >500 °C) in the Earth's subsurface (Pirajno, 2009). The igneous heat source provides energy, which causes the circulation of fluids of various origins (magmatic/juvenile, metamorphic, meteoric, connate waters or seawater) within the host-

rock reservoir (William-Jones and Heinrich, 2005). Alteration occurs as the mineral assemblages in the wall rocks are in physico-chemical disequilibrium with the hydrothermal fluids. Therefore, the system tends to re-equilibrate by forming new mineral assemblages that are stable under the new conditions (Pirajno, 2009). The changing physico-chemical conditions of both the fluids and the wall rocks dictate, whether dissolution, transport, or precipitation of minerals is the dominant mechanism of alteration (Fyfe, 2012). Therefore (a) temperature, (b) pressure, (c) host-rock mineralogy, (d) permeability, (e) fluid composition, (f) water/rock ratio, and (g) time scale of the processes are the main factors controlling hydrothermal alteration (Browne, 1978; Robb, 2005). Alteration comprises a complex series of processes involving chemical, mineralogical, and textural, as well as rock physical (porosity, density, permeability, elastic wave velocity) (Pola et al., 2012) and rock mechanical (e.g. strength) changes (Pirajno, 2009; Pola et al., 2013; Wyering et al., 2014).

Hydrothermal alteration has previously been investigated in numerous studies relating to many research topics, such as formation of ore minerals, submarine thermal systems, and intrusion-related or skarn hydrothermal systems (Browne, 1978; Pirajno, 2009, and references therein). But these processes are beyond the focus of this thesis. The influences of hydrothermal alteration investigated in this work are associated only with the shallow zone of active epithermal systems (geothermal fields), where many phreatic events have been documented to occur (Barberi et al., 1992). Solfataras, fumaroles and mineral springs are some of the characteristic surface expressions of convective fluid circulation powered by the heat of shallow intrusions in geothermal fields (Pirajno, 2009). Alteration in these zones is mainly characterized by acid-sulfate alteration (Figure 1.3).
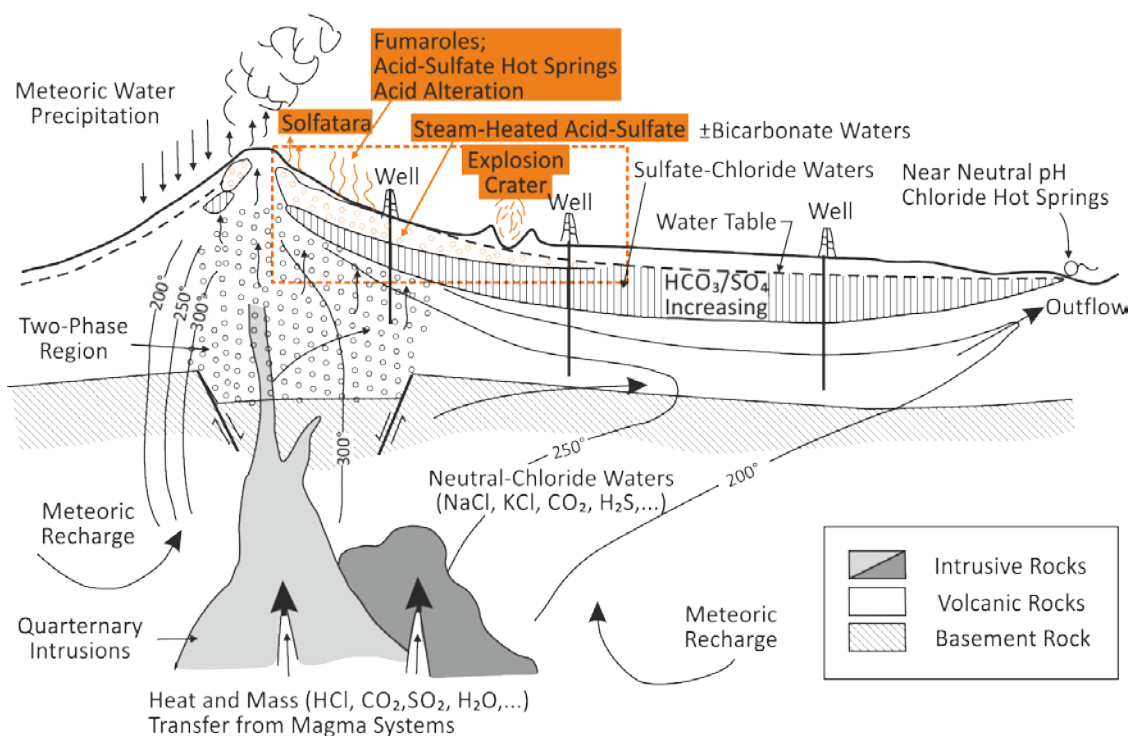
Figure 1.3: Conceptual model of a hydrothermal system. Hydrothermal processes and conditions investigated within this thesis are associated to the highlighted area (modified after Goff and Janik, 2000).

H_2SO_4, the main component of the fluids driving acid-sulfate alteration, may originate from three different processes (Rye et al., 1992): 1) *Supergene acid-sulfate alteration* due to weathering of sulfide-rich deposits where sulfuric acid is generated due to the oxidation of sulfide minerals (e.g. pyrite), 2) *steam heated acid-sulfate alteration* at or above the groundwater table, due to atmospheric oxidation of H_2S deriving from the hydrothermal system, and 3) *magmatic hydrothermal acid-sulfate alteration* due to the formation of H_2SO_4 by the disproportionation of magmatic SO_2 during condensation at intermediate depths. Distinguishing these three processes is difficult, as their respective geological setting and the alteration products formed, are similar to each other (Mutlu et al., 2005).

Alteration in active epithermal systems usually occurs at relatively low temperatures (<300 °C) and at shallow depth (<2 km) (White and Hedenquist, 1995). The distribution of hydrothermal minerals is mainly dictated by the variation in pH and temperature within this environment (Figure 1.4). Vuggy silica, a porous, amorphous residue resulting from extreme leaching and the dissolution of primary phenocrysts represents the endmember mineral phase in these systems, which subsequently recrystallizes to quartz (Hedenquist and Lowenstern, 1994; Stoffregen, 1987; Pirajno, 2009). The progressive neutralization of the hydrothermal fluids by the wall rocks results in an alteration sequence from vuggy silica to advanced argillic, to argillic, and finally to propylitic alteration (Steven and Ratté, 1960; Stoffregen, 1987; Hedenquist and Lowenstern, 1994; White and Hedenquist, 1995).
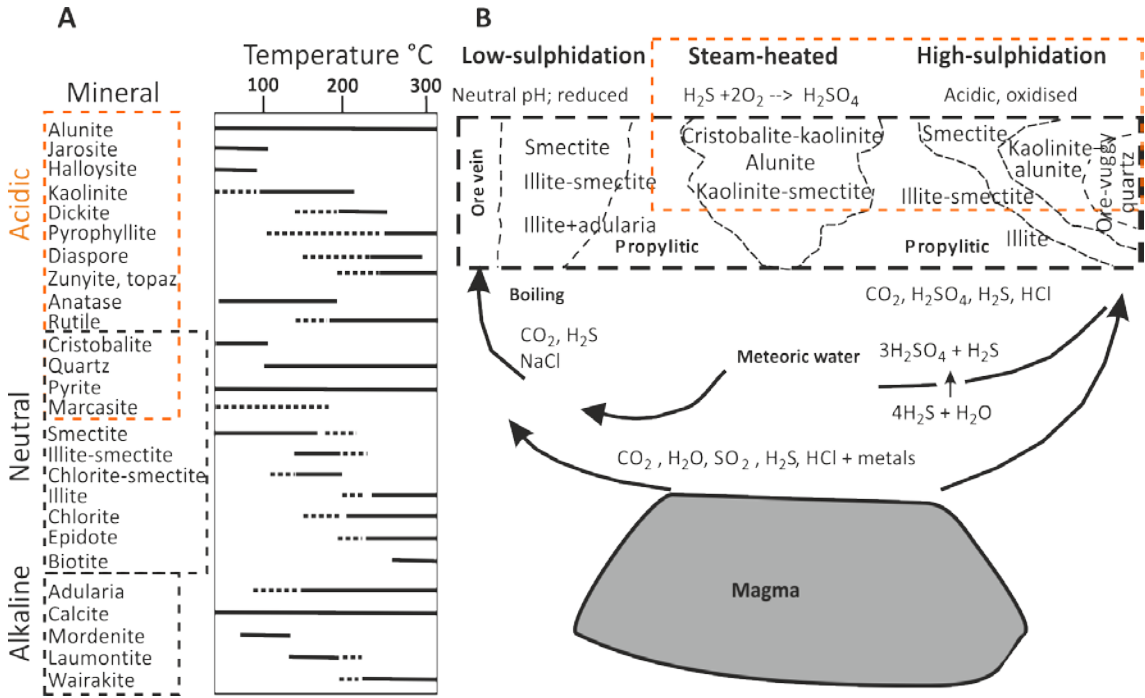
Figure 1.4: (A) Hydrothermal minerals listed with reference to their pH-environments (acidic, neutral, and alkaline). Additionally precipitation and stability of hydrothermal phases is controlled by temperature within the epithermal system. (B) Distribution of minerals formed by low- and high-sulfidation as well as the overprint of steam-heated alteration. Mineral assemblages and alteration types investigated in this study are highlighted (modified after Pirajno, 2009).

Solfataric alteration, also referred to alunitic alteration, is part of advanced argillic alteration and dominated by the formation of alunite in the presence of abundant sulphate ions and Al-rich host rocks (Bishop et al., 2007; Pirajno, 2009). Kaolinite, jarosite, pyrite, opal and cristobalite are further low-temperature acid-stable minerals, often associated to this type of alteration (Pirajno, 2009).

Based on the assumption that the distribution of chemical elements is controlled by the degree of alteration, several indices have been proposed (Pola et al., 2012, and references therein). Table 1.1 summarizes all indices used in this thesis, and shows that they are based on the ratio of ˈmobileˈ to ˈimmobileˈ elements during the alteration process (Pola, 2010). Furthermore they assume the immobility of aluminum and should therefore be carefully applied to heterogeneous samples, especially in environments of hydrothermal alteration (Arıkan et al., 2007; Pola et al., 2012). Nevertheless these indices represent a useful approach to estimate the degree of alteration and correlate well with the petrophysical properties observed for different investigated rocks (Duzgoren-Aydin et al., 2002; Arıkan et al., 2007; Pola et al., 2012, and references therein).

Table 1.1: Chemical alteration indices.

Index	Abbreviation	Formula (molecular ratio)	References
Chemical index of alteration	CIA	$\dfrac{(Al_2O_3) \times 100}{(Al_2O_3 + CaO + Na_2O + K_2O)}$	Nesbitt and Young (1982)
Alumina to calcium–sodium oxide ratio	ACN	$\dfrac{Al_2O_3}{(Al_2O_3 + CaO + Na_2O)}$	Harnois and Moore (1988)
Silica to alumina ratio	SA	$\dfrac{SiO_2}{Al_2O_3}$	Ruxton (1968)
Plagioclase index of alteration	PIA	$\dfrac{(Al_2O_3 - K_2O) \times 100}{(Al_2O_3 + CaO + Na_2O - K_2O)}$	Fedo et al. (1995)
Chemical index of weathering	CIW	$\dfrac{(Al_2O_3) \times 100}{(Al_2O_3 + CaO + Na_2O)}$	Harnois (1988)

The effects of hydrothermal alteration on rock physical and mechanical properties have been investigated in several studies (Pola et al., 2012, 2013; Mormone et al., 2011; 2015; Wyering et al., 2014; Heap et al., 2014, 2015; Mayer et al., 2015; Carlino et al., in review). In general they focused on the degradation of petrophysical properties as a result of alteration. Concerning the influence of alteration on volcanic (magmatic or phreatic) eruptions processes, only a minor amount of investigation have been conducted so far (Foote et al., 2011; Mayer et al., 2015). Alteration can cause the development of a sealing cap rock by 1) the precipitation of secondary minerals (Edmonds et al., 2003; Christenson et al., 2007), or 2) the formation of a low permeability clay-rich lithology (Barberi et al., 1992; Alvarado et al., 2010). Such processes may lead to hydrothermal paroxysms or even phreatic eruptive events (Christenson et al., 2010; Vignaroli et al., 2015). By contrast, rock alteration associated with leaching processes, the dissolution and removal of cations by acidic (pH <2) fluids, may increase porosity and permeability (Hedenquist and Lowenstern, 1994; Ladygin et al, 2014), eventually generating vuggy (residual) silica (Boyce et al., 2007; John et al.,

2008; Scher et al., 2013) and thereby facilitate gas escape in the shallow zone (Piochi et al., 2015).

The investigation of easily accessible surficial rocks outcropping within a hydrothermal system may help to unravel the processes and effects of hydrothermal alteration. Moreover, alteration mineral assemblages provide insights into the dynamics of volcanic system and show implications on their outgassing behavior.

1.3   Thesis objectives and structure

Phreatic eruptions generally occur in an environment affected by hydrothermal alteration (Barberi et al., 1992). Recent eruptions at Mt. Ontake in Japan, which resulted in the deaths of 57 climbers (Kato et al., 2015), as well as at Ruapehu and Te Maari in New Zealand (Breard et al., 2014), have sparked new awareness of their unpredictability with respect to time, eruption dynamics and magnitude. Frequently, alteration processes induced by the hydrothermal system, which change the host-rocks composition and properties, may create favorable conditions for phreatic eruptions (Christenson et al., 2007). This study therefore explores the effects of alteration on rock properties, which in turn may control the eruption dynamics of phreatic events. The course of this work follows a general trend in focus from phreatic eruption dynamics to hydrothermal alteration processes and its effects on both the trigger potential as the properties of material involved in such eruptions.

The investigated sites include 1) Whakaari (White Island volcano) in New Zealand, 2) Campi Flegrei in Italy, and 3) Valley of Desolation (Dominica) in the Lesser Antilles. All three locations are characterized by vigorous hydrothermal activity associated with intense rock alteration and exhibited several phreatic eruptions in the past. Such events are furthermore the most likely scenario for future volcanic activity at these locations. Therefore these sites constitute exemplary case studies.

Field campaigns have been conducted in order to investigate the main sites of hydrothermal activity within the studied locations. Mapping, sampling, and in situ measurements have permitted the collection of valuable information in the field (e.g. alteration conditions) and subsequent characterization of collected material was performed in the lab. Finally, rapid decompression experiments allowed to determine the fragmentation and ejection behavior of collected samples under various conditions. For the first time natural samples could be pressurized, fragmented, and ejected by pure steam expansion. The results based on this advanced technique together with experiments in the presence of steam flashing and argon gas expansion (at elevated pressures and temperatures) allowed the exploration of a large range of phreatic conditions.

The central purpose of this thesis was the comparison of the geochemical composition of collected rock material in the context of possible changes of their petrophysical properties. These properties were investigated with a focus on their behavior during rapid decompression experiments. Hence the collected rocks comprised materials

with varying degrees of consolidation and cementation. Moreover, sampling was carefully conducted based on observable differences in macroscopic texture, color, and particle size in order to collect material with a wide-ranging degree of alteration.

The key aims of this study were:

➢ *Investigation of the alteration type and its effects on the mineralogical composition of the host rock;*

➢ *Characterization of petrophysical properties changing as function of their degree of alteration.*

➢ *Investigation of the effects of fluid type (i.e. gas or liquid), pressure and temperature, on phreatic eruption processes;*

➢ *Analysis of the alteration effects on the fragmented particles shape and their size distribution.*

Those aims should finally be addressed by new conceptual models, which summarize and display the obtained results.

The five chapters of this thesis are structured around the central theme of investigating the influence of hydrothermal alteration on phreatic processes.

Chapter 1 provides a general introduction to phreatic eruptions and hydrothermal alteration processes, and explains the thesis objective and structure.

Chapter 2, **Chapter 3** and **Chapter 4** examine three individual case studies, including discrete and specific information of the alteration processes affecting the investigated sites. Each chapter builds progressively upon the findings of the previous chapters.

Chapter 5 presents a synthesis, which is summarizing the key findings and outlining the general conclusions from this dissertation. Finally, ongoing work and future perspectives, which arose during this PhD are presented.

This page was intentionally left blank.

2   Experimental constraints on phreatic eruption processes at Whakaari, New Zealand

Figure 2.1: Phreatic eruption on august 19th 2013 at Whakaari, New Zealand (Courtesy of GeoNet).

This page was intentionally left blank.

2.1 Introduction

Whakaari also known as White Island volcano, is New Zealand's most active volcano and characterized primarily by phreatic and phreatomagmatic eruptions, interspersed by occasional Strombolian events (Cole and Nairn, 1975; Simkin and Siebert, 1994). Its phreatic eruptions are associated with an increasing number of 1-5 Hz harmonic tremors (e.g., Nishi et al., 1996; Sherburn et al., 1998). Recent analysis has linked these events to progressive fracturing and fluid flow within the system (Chardot et al., 2015; Heap et al., 2015).

Phreatic events (28 phreatic eruptions since 1826) exhibited at Whakaari (Figure 2.2), the risk associated with the high number of tourists (>13,500 annual visitors; Letham-Brake, 2013) visiting the volcano island on a daily basis, and the relatively detailed knowledge of rock mechanics available (Moon et al., 2005; Heap et al. 2015) make Whakaari an exemplary case study for a detailed experimental investigation of phreatic processes.
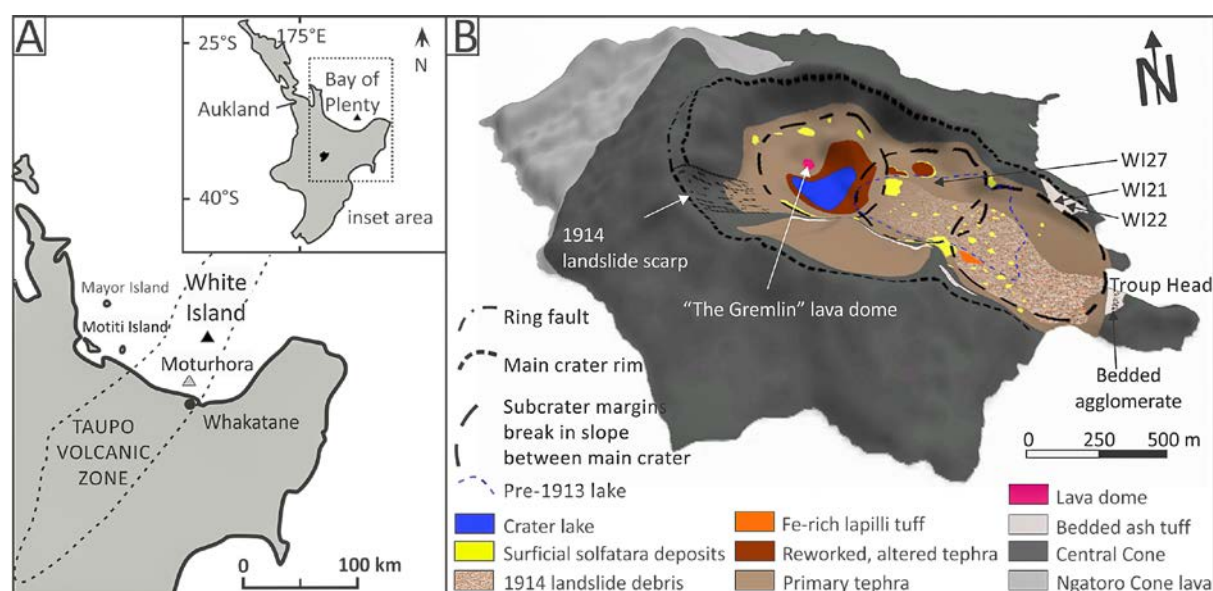
Figure 2.2: (A) Location map of Whakaari (White Island volcano) approximately 50 km offshore in the Bay of Plenty within the Taupo Volcanic Zone. The inset shows a map of the North Island of New Zealand (modified from Moon et al., 2009). (B) Geological map of Whakaari showing in detail the distribution of unconsolidated crater fill (modified from Letham-Brake, 2013) and sampling sites for this study.

A detailed survey of the literature revealed that >30 phreatic and phreatomagmatic eruptions (Figure 2.3) have been recorded at Whakaari since 1826 (Letham-Brake, 2013). The recent eruptive event of 5th August 2012, associated with phreatic eruptions, led to the formation of a spiny lava dome in the crater (Global Volcanism Program, 2014). Past studies at Whakaari have focused on the surveillance and the prediction of future eruptive activity via monitoring of seismicity (Jolly et al., 2012; Nishi et al., 1996; Sherburn et al., 1998) and ground deformation (Clark, 1982; Fournier and Chardot, 2012; Peltier et al., 2009) as well as

the emission (Werner et al., 2008; Bloomberg et al., 2014) and characterization of gases and fluids (Giggenbach et al., 2003). Furthermore, studies of the petrology (Graham and Cole, 1991), the origin and storage of magma (Cole et al., 2000), and the geotechnical characterization and geomorphic development of the edifice have been conducted (Moon et al., 2005, 2009; Heap et al., 2015).

Despite the abundance of previous phreatic eruptions at Whakaari and the preservation of deposits (e.g., Wood et al., 1996), no adequate constraints on the explosive parameters and mechanisms exist. Although the geological setting and hydrothermal system are relatively well-constrained, their interplay in general as well as in view of the mechanisms triggering phreatic eruptions, are not yet fully understood. Adding to this complexity is the fact that the physical properties and mechanical behavior of Whakaari rocks are highly altered due to the activity of the hydrothermal system (Pola et al., 2013; Wyering et al., 2014; Heap et al., 2015). Changes in state of alteration during thermal stressing, as is the case during shallow (~500 m below sea level) magma intrusion, commonly induce mineral breakdown, which leaves a skeletal porous rock with deteriorated mechanical strength (Peltier et al. 2009; Heap et al., 2012).

The porosity of a rock controls the amount of gas stored and therefore the energy available for release during fragmentation for a given decompression step (Spieler et al., 2004; Alatorre-Ibargüengoitia et al., 2010). Earlier studies have defined the fragmentation threshold (the minimum pore pressure differential required to fully fragment the sample) as being inversely proportional to the porosity (Spieler et al., 2004). Foote et al. (2011) and Rager et al. (2013) have presented results of experimental phreatic fragmentation induced by both inert gas overpressure and steam flashing in vesicular rocks, and made an initial evaluation of the influence of pressure, sample alteration and sample saturation on these processes. Here, the results of a systematic experimental campaign employing a shock-tube apparatus (Aldibirov and Dingwell, 1996a) to perform decompression experiments on both hydrothermally altered consolidated and loose deposits, inferred to reflect those deposits existing at depth at Whakaari (Heap et al., 2015), are presented. Specifically, the influence of sample type and fragmentation mechanism (steam flashing versus gas expansion) on grain size and shape and on fragmentation and ejection velocities was investigated.

2.2   Geological setting

Whakaari located 50 km offshore from the North Island of New Zealand (Figure 2.2A), is an andesitic-dacitic, stratovolcano exhibiting strong fumarolic activity and outgassing (Bloomberg et al., 2014) interspersed by eruptive events. It is the northernmost active volcano within the Taupo Volcanic Zone (TVZ), which is itself a 250-km-long belt of mainly rhyolitic and andesitic, Quaternary to present volcanism (Black, 1970). The northeast-southwest-trending TVZ extends 200–270 km west of the trench resulting from the convergence of the Pacific and Australian plates (Nishi et al., 1996).

The island occupies an area of approximately 3.3 km² with a maximum elevation of 321 m above sea level and represents the emergent summit of the much larger White Island Massif (Nishi et al., 1996) whose basal extent of 16 km × 18 km yields a total volume of ~78 km³ (Duncan, 1970; Cole et al., 2000). The edifice consists of two overlapping composite cones, comprised of major lava flow units, and minor tuff and tephra units. The older Ngatoro cone only outcrops in the west, whereas the younger and active central cone forms most of the island (Black, 1970; Duncan, 1970; Cole et al., 2000; Cole and Nairn, 1975). The NW−SE elongated main crater (1.2 km × 0.4 km) is a complex of three coalesced prehistoric subcraters, infilled with unlithified deposits from historical eruptions, which have been confined to the western subcrater and the western half of the central subcrater (Houghton and Nairn, 1989a; 1991). Due to the occurrence of a large (210×10^6 m³) prehistoric, eastward-trending sector collapse (Moon et al., 2009), the horseshoe-shaped, flat-floored crater is breached to the sea in three locations in the southeast (Cole et al., 2000). The collapse of the main crater wall in the southeast caused a debris avalanche of 2.5×10^5 m³, which has covered parts of the main crater floor (Ward, 1922; Bartrum, 1926 in: Hamilton and Baumgart, 1959).

Magma has been hypothesized to exist transiently at shallow depths (<500 m) as well as extending to deeper chambers at 1–2 km and 2–7 km (Cole et al., 2000; Houghton and Nairn, 1989a in: Werner et al., 2008). This most shallow magma is believed to be the source for large ground deformation and seismicity episodes and, ultimately, the large acidic, volcano-hydrothermal system (Giggenbach, 1987).

2.2.1 Hydrothermal setting

Fumarole and spring discharge analyses have indicated that the hydrothermal system of Whakaari has been active for more than 10.000 years (Giggenbach and Glasby, 1977; Giggenbach et al., 2003). Hot fluids released from the magma condense in contact with meteoric groundwater and circulate within the conduit-hosted, volcano-hydrothermal system that has been interpreted to occur in isolated, chemically-sealed zones around the volcano (Giggenbach, 1987). More recent isotopic studies show that, there is less seawater component in the fumarolic output of the western and central subcraters than the eastern subcrater (Giggenbach et al., 2003; Bloomberg et al., 2014).

The hydrothermal system finds its expression in the form of numerous fumaroles, steaming ground areas, hot springs, and a crater lake. Fumarole temperatures vary between 100 and 800 °C in response to outgassing fluctuations of the magma, yielding cooling and heating stages (Giggenbach et al., 2003). These fluctuations further correlate with variations in the discharge of fluids (H_2O, CO_2, HCl) (Pirajno, 2009). The low pH of the crater lake (1.2–2.4) (Werner et al., 2008), the acid springs (0.7–1.4), and the pools (0.7–0.8) as well as the strong H^+ activity of the hydrothermal system results from ingress of HCl and H_2S, which are the dominant acids in the fluids (Pirajno, 2009; Giggenbach et al., 2003). These acidic fluids promote mineral dissolution and corrosion leading to substructure weakening and an

increased susceptibility for further alteration (Houghton and Nairn, 1989a, 1991). The very high sulfate content in the magmatic gas (75,000 ppm) favors the formation of alunite amongst other mineral assemblages which are formed by acid alteration (Giggenbach et al., 2003).

Geophysical evidence suggests that the hydrothermal fluid flow is focused primarily in the thermally weakened zones, such as proximity of former and newly-formed eruption craters as well as in the 200–650 °C fumarole fields (Clark and Otway, 1982; Christoffel, 1989; Hurst et al., 2004; Peltier et al., 2009; Fournier and Chardot, 2012). The semi-regular cycling (2–10 years) of the hydrothermal fluid flow causes a cycling in ground inflation (≤ 250 mm) due to increases in pore pressure as well as to thermal expansion of the reservoir rocks at depths of ~200–600 m, both interpreted as evidence of the presence of magma below the central and western subcraters (Peltier et al., 2009; Fournier and Chardot, 2012).

2.2.2 Eruption history

At Whakaari, the interplay of hydrological factors and magmatic activity helps to determine the nature of hydrothermal processes and the characteristics of associated eruptions. (Houghton and Nairn, 1991). A prehistoric sector collapse (<3.4 ka) may have induced a fundamental change in the hydrothermal fluid flow field by eradicating low permeability cone lavas and thereby allowing the infiltration of meteoric water (Letham-Brake, 2013). This may, in turn, have favored the change from at least 19 prehistoric, magmatic lava-flow producing eruptions (Cole et al., 2000) to long periods of continuous fumarolic and hydrothermal activity interspersed by a minimum of 2 small (VEI 1–3) phreatic and phreatomagmatic eruptions recorded since 1826 (Figure 2.3). The main crater-forming eruptions occurred in 1933, 1947, 1965-1966, 1968, 1971, 1976-1982 and 1986–1991. The long, 1976–1982 period of unrest was characterized by strombolian and phreatomagmatic eruptions (Houghton and Nairn, 1989b, 1991; Clark and Otway, 1982). All historic activity has occurred within the western subcrater and the western part of the central subcrater (Houghton and Nairn, 1991).
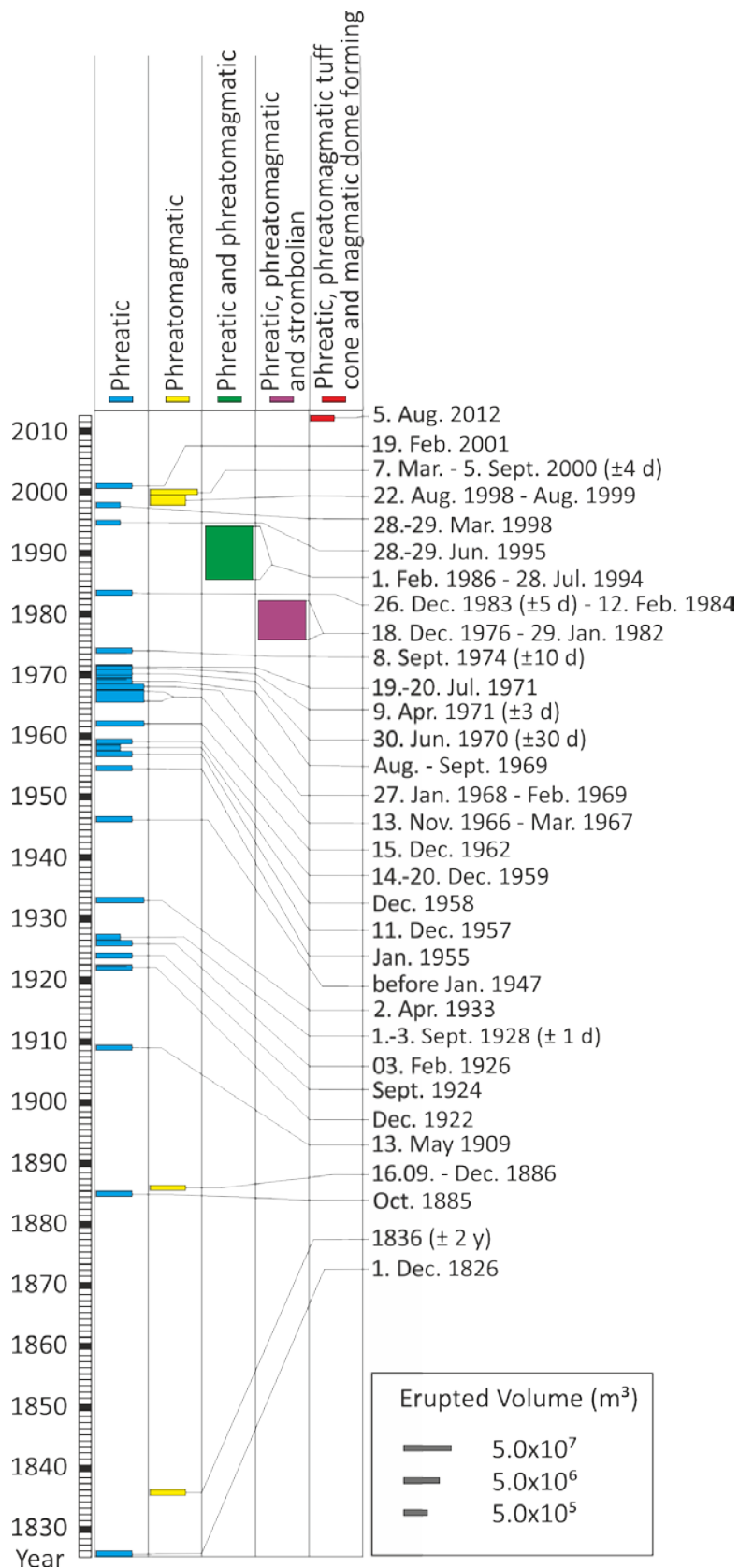
Figure 2.3: Timeline of historic eruptions at Whakaari from 1826 to 2012. Single events as well as periods of activity are classified based on the dominant activity reported in literature. A table (modified after Letham-Brake, 2013) listing the events as well as the used literature can be found in Appendix A. Type of eruption and estimated erupted volume are indicated in the figure.

2.3 Investigated lithologies

This study focuses on three volcaniclastic rocks from lithostratigraphic units at Whakaari. Two consolidated ash tuff units (WI21, WI22) were collected from the scree at the foot of the eastern crater wall (Figure 2.2B), estimated to originate from approximately 70 m beneath the current cliff top (Heap et al., 2015). One recent, unconsolidated tephra (WI27) typical of the main crater fill deposit has been sampled at 1-m depth within the central subcrater (Figure 2.2B). X-ray fluorescence analysis (XRF) of the bulk geochemical composition of each sample was conducted using a Philips Analytical Magix Pro WDX-spectrometer at the Ludwig-Maximilians-Universität München (LMU). Results of analyses on pressed powder tablets are presented in Table 2.1. Mineralogical analysis of the samples was carried out using X-ray powder diffraction analysis (XRD) conducted at the Technische Universität München (Table 2.2). For XRD analysis, the samples were disaggregated, mixed with an internal standard (10% ZnO), and ground for 8 min with 10 ml of isopropyl alcohol in a McCrone Micronising Mill using agate cylinder elements. The powder mounts of the samples were analyzed with a Philips PW 1800 X-ray diffractometer (CuKα, graphite monochromator, 10 mm automatic divergence slit, step-scan 0.02° 2θ increments per second, counting time 1 s per increment, 40 mA, 40 kV). Quantification of the crystalline and amorphous phases in the whole rock powders was performed by using the Rietveld program BGMN (Bergmann et al., 1998). A comparison of chemical compositions measured by XRF with those calculated based on XRD results and the chemical composition of the involved phases allowed us to distinguish if the amorphous phase was predominantly opal-A or volcanic glass.

Table 2.1: Average bulk geochemical composition of studied samples based on X-ray fluorescence analyses.

Sample	WI21	WI22	WI27
SiO_2	59.70	79.60	62.67
Fe_2O_3	0.90	1.65	6.84
Al_2O_3	13.14	7.03	12.84
MnO	0.01	0.01	0.07
CaO	0.71	0.85	3.94
MgO	0.06	0.32	2.65
K_2O	3.37	1.07	2.11
Na_2O	1.57	0.48	1.28
TiO_2	1.19	1.06	0.70
P_2O_5	0.10	0.05	0.09
LOI	18.46	7.79	6.36
Sum	99.21	99.91	99.55

The ash tuffs (WI21 and WI22) consist of altered crystal fragments and devitrified glass shards (Figures 2.4–2.5), which are composed primarily of hydrated amorphous silica (opal-A). Alunite and minor opal-A cement the crystal-vitric ash tuffs (Figure 2.5), in which the original shards and crystal fragments are hard to distinguish from one another due to massive opalisation. The maximum particle sizes of the ash tuffs are on the order of 0.2 mm (WI21) and 0.3 mm (WI22) and the dominant pore size diameters are on the order of several

hundred microns (Figures 2.4–2.5). The white/grey ash tuff (WI21) consists of amorphous phases, predominantly opal-A (66%), alunite (32%) and minor amounts of gypsum, cristobalite and quartz (Table 2.2). The grey, ash tuff (WI22) is more heterogeneous, showing a distinct bedding of approximately 10 mm-thick layers of low and high porosity.
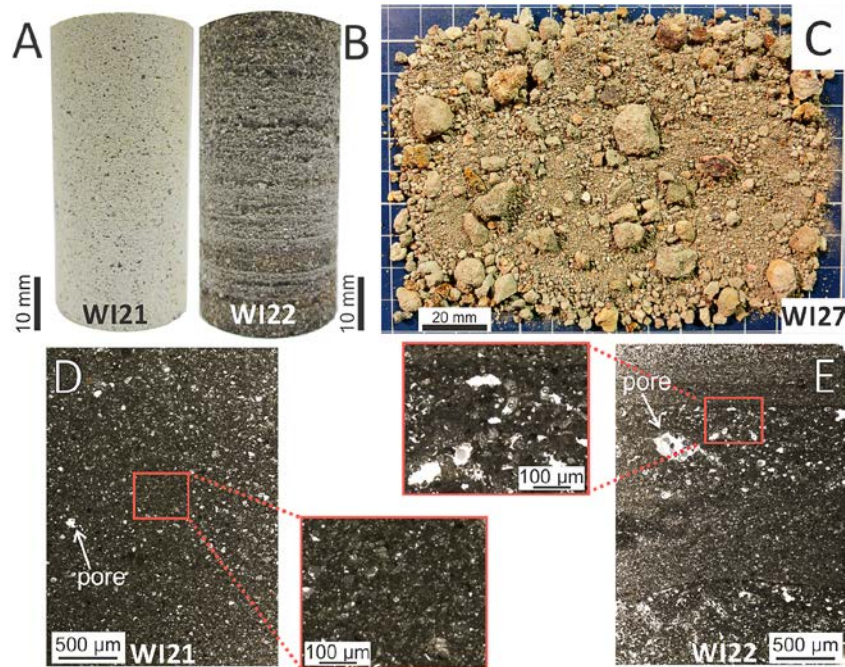
Figure 2.4: Photographs and thin section scan images of the Whakaari ash tuff WI21 (A and D),WI22 (B and E) and the loose ash/lapilli sampleWI27 (C). The insets show close-up images of the samples. WI22 samples are less homogenous and contain larger pores; the distribution of fine and coarse particles generates a clearly visible layering of the sample.

XRD analysis and chemical data shows that it is mainly composed of opal-A (90%), alunite (6%), cristobalite (3%), and minor quantities of gypsum and quartz (Table 2.2). The brown, unconsolidated, poorly-sorted primary tephra (Figure 2.4) comprising 80% coarse ash and 20% lapilli (hereafter referred to as 'ash/lapilli') is composed of amorphous volcanic glass (59%), plagioclase (15%), pyroxene (9%), alunite (8%), and minor quantities of gypsum and cristobalite.

Table 2.2: Mineral composition of studied samples based on X-ray diffraction analyses.

Sample	WI21	WI22	WI27
Opal-A	66 ± 6	90 ± 3	
Plagioclase			15 ± 2
Pyroxene*			9 ± 2
Alunite**	32 ± 3	6 ± 3	8 ± 2
Gypsum	1 ± 1	1 ± 1	2 ± 1
Cristobalite	1 ± 1	3 ± 1	7 ± 1
Quartz	<1	<1	
Sum	100	100	100

* includes ortho- and clinopyroxene

** includes Na- and K- dominated alunites
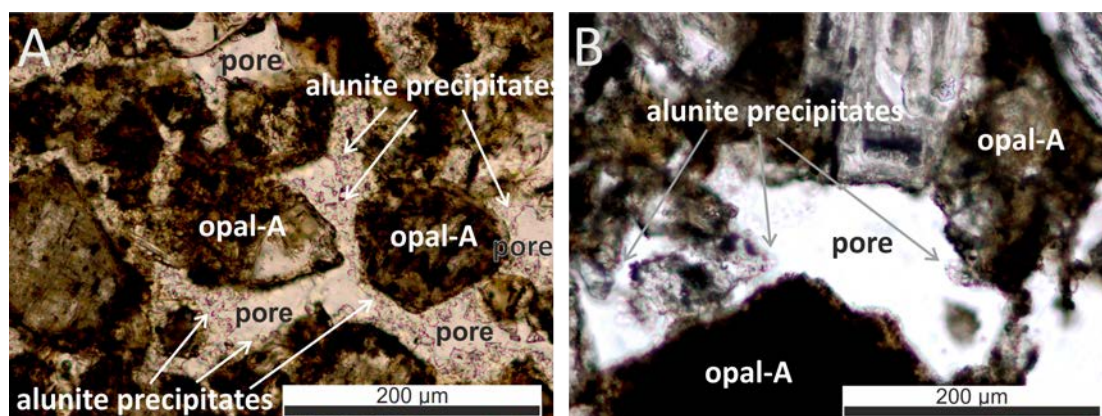
Figure 2.5: Photomicrographs (taken under transmitted cross-polarized light) show amorphous opal particles cemented by alunite. Alunite precipitated within the pores, on opal particles. (A)WI21 shows smaller pores with a higher amount of alunite precipitates compared with (B) showing WI22. Main components of pores, alunite precipitates, and opal-A are identified on the figures.

2.4   Methods

Rapid decompression experiments were performed using a 'fragmentation bomb' apparatus (Alidibirov and Dingwell, 1996a,b; Martel et al., 2000; Spieler et al., 2003, 2004; Mueller et al., 2005, 2008; Kueppers et al., 2006; Scheu et al., 2006, 2008; Rager et al., 2013; Richard et al., 2013). The device in its present configuration permits the accurate control of temperature, gas overpressure and decompression rate in order to best represent variable volcanic and hydrothermal conditions. It is, in essence, a shock-tube apparatus, consisting of a stainless steel low-pressure tank (l=3.0 m; d=0.4 m) at ambient pressure and temperature to collect the experimentally generated pyroclasts, and a high-temperature steel autoclave, in which the sample is mounted (Figure 2.6). The sample (either dry or water saturated) is inserted in the autoclave (l = 450 mm; d = 25 mm), which is externally heated up to 400 °C and pressurized up to 25 MPa using argon gas; when the sample is water saturated, water turns into a supercritical fluid. The pressure and temperature in the system are monitored at rates of 1000 Hz and 2 Hz, respectively. A dynamic pressure sensor and a thermocouple are located at the bottom of the sample; the second pressure sensor sits at the upper end of the autoclave, 225 mm above the sample (Figure 2.6). The autoclave and low-pressure tank are separated by a set of two diaphragms that enable triggering of decompression by a controlled failure of the uppermost diaphragm. The rupture leads to instantaneous failure of the other diaphragm, and rapid decompression of the high-pressure autoclave. Upon diaphragm failure, a shock wave travels upwards into the low-pressure collector tank and a rarefaction wave propagates downwards into the autoclave traveling through the sample. The sample fragments in a brittle manner in a layer-by-layer fashion (Aldibirov and Dingwell, 2000; Fowler et al., 2010) and the particles are ejected into and stored in the collector tank.
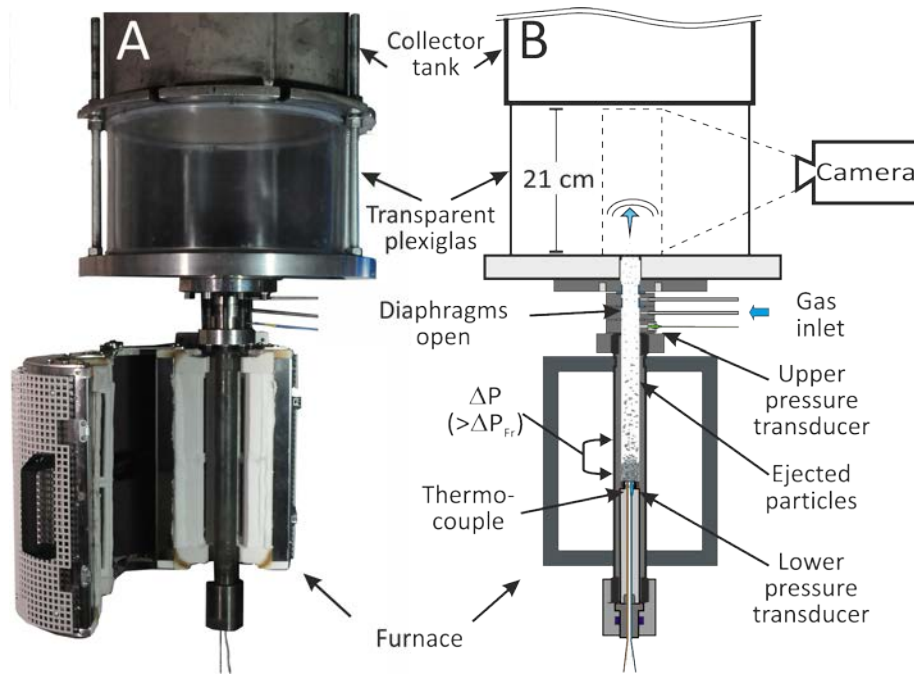
Figure 2.6: Photograph (A) and schematic drawing (B) of the experimental setup used during this study. The high pressure autoclave is separated from the low pressure tank by a set of two diaphragms. Pressure and temperature within the autoclave are monitored by transducers and a thermocouple (adapted from Scheu et al., 2006). Particles fragmented during decompression are ejected into the ambient pressure collector tank. Particle ejection is monitored by a high speed camera through a transparent plexiglass.

All three sample series experiments were conducted on both dry and fully water-saturated samples. For consolidated samples (WI21, WI22) cylindrical samples, 25 mm in diameter and 60 mm in length, were cored, ground flat and parallel. All cylinders as well as the loose ash/lapilli samples were dried in an oven at 65 °C for at least 24 h until fully dry. Prior to the rapid decompression experiments, porosity and bulk density of each sample were determined using a helium pycnometer (Ultrapyc 1200e®, Quantachrome, USA); the results are in good agreement with the triple-weight water saturation technique (Table 3; Heap et al., 2015). The two ash tuff samples (WI21, WI22) used for fragmentation experiments have mean porosities of 32 and 49%, respectively, whereas the loose ash/lapilli (WI27) has a porosity of 51% (Table 2.3). Gas permeability of selected samples was determined using a benchtop (nitrogen) permeameter (Figure 2.7).
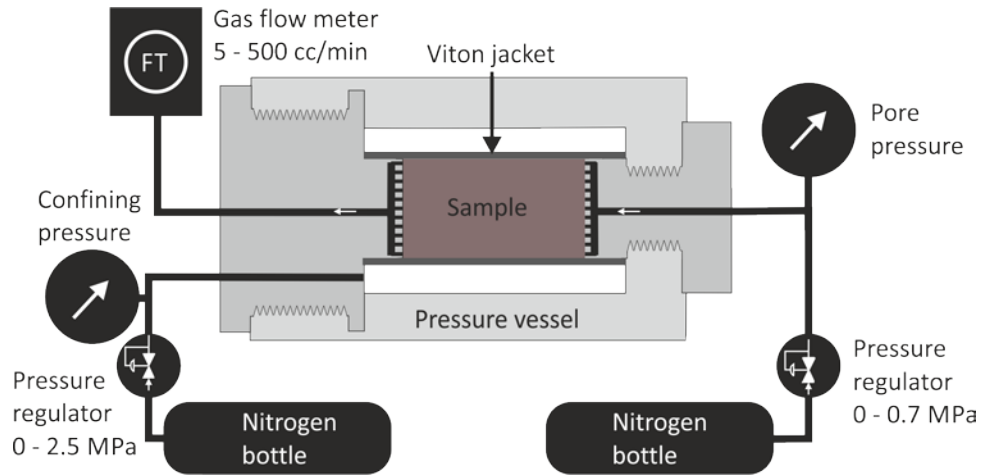
Figure 2.7: Schematic drawing of the benchtop lab permeameter at the École et observatoire des sciences de la Terre (EOST)–Université de Strasbourg.

For the ash tuffs WI21 and WI22, permeability was measured under a confining pressure of 1 MPa and was found to be 1.5×10^{-16} and 3.5×10^{-14} m^2 respectively (Table 2.3). For the loose ash/lapilli (WI27), material (excluding the lapilli larger than about 5 mm) was poured into a rubber jacket (20 mm in diameter and about 40 mm length) and its permeability under a confining pressure of 0.3 MPa was measured. The permeability of WI27 resulted to be 3.4×10^{-12} m^2 (Table 2.3).

Table 2.3: Summary of the rock physical properties of investigated samples. Porosity measurements from Heap et al. (2015) by using the triple-weight water saturation technique and permeability of the ash/lapilli at a confining pressure of 0.3MPa are also included. Permeability measurements of WI21 and WI22 were collected under a confining pressure of 1 MPa. (Note: Given values for density and porosity are averaged on all samples and might therefore differ from values shown in figures).

Sample	Density (g/cm^3)	Porosity (connected) (%)	Porosity (closed) (%)	Porosity Heap et al., (2015) (%)	Gas Permeability (m^2)
WI21 ash tuff	2.3	32	3.8	29	1.5×10^{-16}
WI22 ash tuff	2.2	49	3.2	46	3.5×10^{-14}
WI27 ash / lapilli	2.5	51	3.0	n.m.	3.4×10^{-12}

For rapid decompression experiments the samples were mounted into a steel sample holder and directly placed inside the autoclave ready for dry fragmentation experiments. For experiments in the presence of steam-flashing, samples (already mounted into a sample holder) were submerged in water and placed under a vacuum for at least 72 h to facilitate water to be absorbed into the connected porosity assuring maximum water saturation. By contrast, unconsolidated samples were poured into sample holders with effort made to ensure that their particle size distribution was not misrepresented (i.e., undisturbed from laboratory manipulation and water-saturated in the same manner).

2.4.1 Fragmentation threshold

The fragmentation threshold was first determined for both ash tuff sample series at room temperature (dry condition); for this purpose, a series of tests was done where the applied pore pressure was successively increased (from 2 MPa) until complete fragmentation of the samples was achieved. In cases where the sample did not fragment, the same sample was tested again with the initial pressure raised by an increment of 0.5 MPa. This procedure was continued until the removal of a few millimeters of the sample surface occurred. This fragmentation initiation is usually 0.5–1.5 MPa below the complete fragmentation of the sample, which is defined as the fragmentation threshold (Scheu et al., 2006).
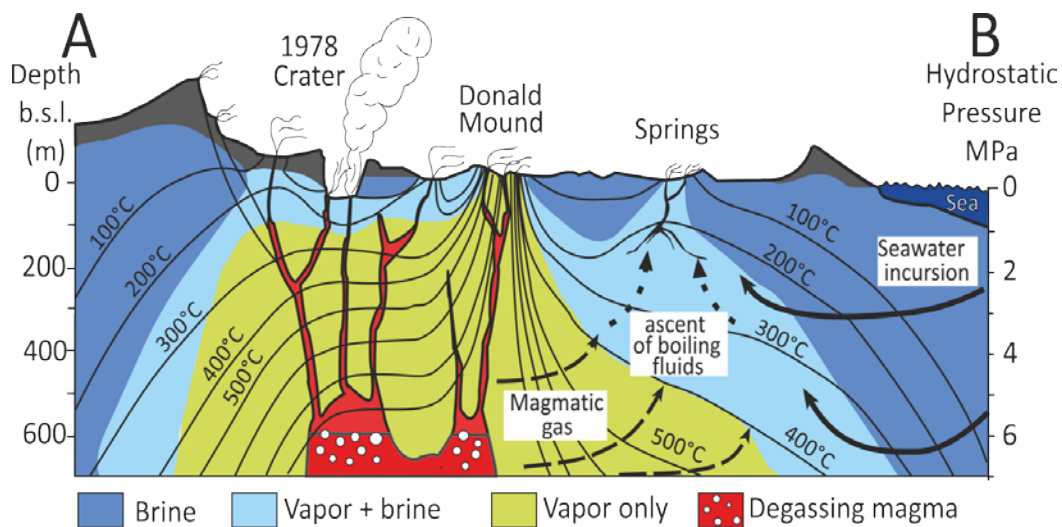
Figure 2.8: Schematic cross section through Whakaari hydrothermal system. The dashed, dashed–dotted and solid arrows indicate flows of the magmatic gas, boiling brines and seawater, respectively (modified after Giggenbach et al., 2003). The subsurface of the highly active strato volcano is characterized by regimes of liquid and gaseous fluids.

2.4.2 Fragmentation and ejection speed

Giggenbach (2003) estimates the temperatures in the proximity of the fumaroles, within the uppermost 200 m below the western subcrater, in the range from 200 to 300 °C (Figure 2.8). In order to compare fragmentation initiated by steam flashing following rapid decompression, with fragmentation initiated by argon gas expansion, both water-saturated and dry samples were heated to 270 °C and pressurized to 6.5 MPa. The temperature was chosen in agreement to the temperatures estimated by Giggenbach (2003); the applied pressure was fixed to 6.5 MPa in order to allow decompression from the liquid phase slightly above the boiling curve but still at a reasonable pressure condition for Whakaari. For a precise acquisition of the dwell condition for the experiments performed on dry samples, samples were initially pressurized to about 4 MPa. The target temperature of 270 °C was reached after a heating time of 45 minutes whereas during the last stage of heating, the

remaining pressurization required for a dwell pressure of 6.5 MPa was applied. Holding these final conditions for a dwell time of 10 minutes ensured temperature and pressure equilibration over the entire sample before triggering the fragmentation.

For the experiments performed on water-saturated samples, the autoclave was first pressurized with argon gas to 4.0 MPa before heating (Figure 2.9), thereby holding the water in the liquid state throughout the experiments. Shortly before approaching the final temperature of 270 °C, the autoclave was pressurized further with argon to the target dwell conditions. The final dwell condition was held constant for a further 10 minutes to ensure equilibrated conditions within the autoclave and the sample, before the controlled opening of the diaphragms was initiated. During the decompression of the system, the phase transition from liquid water to water vapor is crossed (Figure 2.9).
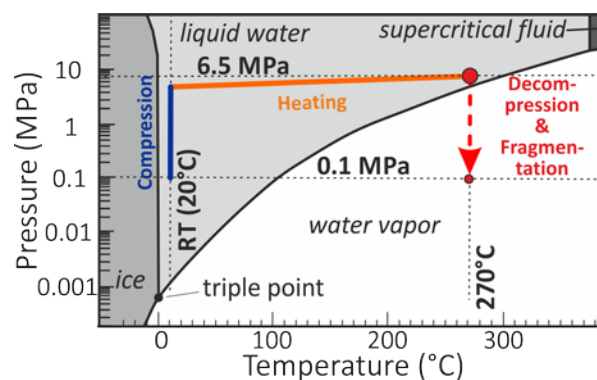
Figure 2.9: Experimental pressure and temperature conditions. Both dry and water saturated samples were initially pressurized to about 4 MPa, then heated to 270 °C and further pressurized to 6.5 MPa during the last stage of heating. Water within the pores of saturated samples immediately flashes to steam during decompression when crossing the phase transition from liquid water to water vapor.

Analysis of the pressure sensor and high speed camera recording allowed to quantify the fragmentation speed and ejection speed of particle front. Particle-size distribution as well as particle shape was investigated by recollection of the experimentally generated pyroclasts from the low-pressure tank.

2.5   Results

2.5.1   Fragmentation threshold

In order to account for sample heterogeneities, the determination of the fragmentation threshold was repeated three times for each ash tuff. The low porosity (Φ = 31–33 %, WI21) and the high porosity (Φ = 44–47 %, WI22) ash tuffs fully fragment at initial pressures ranging between 4.3–5.3 MPa and 3.8–4.0 MPa, respectively (Figure 2.10). The results are fully in accordance with the fragmentation threshold defined in previous studies (e.g., Spieler et al., 2004) and in agreement with the fragmentation criterion of Koyaguchi et al. (2008).
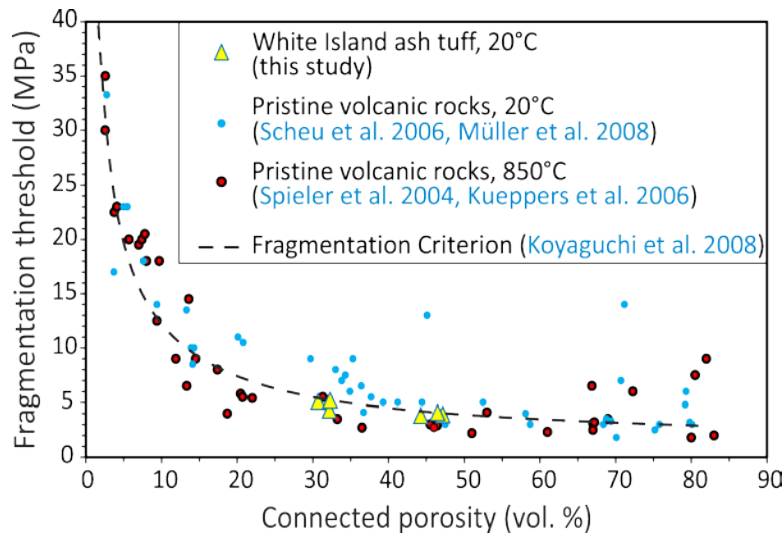
Figure 2.10: Fragmentation threshold of Whakaari ash tuffs (triangles) at 20 °C during rapid decompression. Fragmentation thresholds for pristine volcanic rocks at 850°C and 20 °C also are compiled. The dashed line corresponds to the fragmentation criterion proposed by Koyaguchi et al. (2008). Samples with a higher porosity fragment at a lower initial pore pressure. Whakaari samples confirm the criterion plotting slightly below the dashed line.

2.5.2   Fragmentation speed

Rapid decompression experiments at 270 °C and an initial applied pressure of 6.5 MPa were performed for all three sample series under both dry and water-saturated conditions in order to determine the fragmentation speed. Figure 2.11 illustrates the following dependencies of the fragmentation speed: (1) for identical conditions (dry argon or steam flashing), the fragmentation speed of the consolidated ash tuffs increases with porosity. For the dry experiments, samples with ~ 32 % porosity have fragmentation speeds between 10 – 28 m/s, and at ~ 52 %, porosity fragmentation speeds increase to 53 – 83 m/s. Fragmentation speed in the presence of steam flashing increased with increasing porosity in the ash tuffs (~ 34 % samples 75–130 m/s and ~ 51 % samples 160–180 m/s). Within a samples series (given mean porosity), the presence of steam flashing significantly increases the speed of fragmentation. Ash tuffs where steam flashing occurred led to increased fragmentation speeds for WI21 (Φ = 33 %) from 10–28 m/s to 75–130 m/s and for the highly porous tuffs WI22 (Φ = 51 %) from 53–83 m/s to 160–180 m/s, respectively. (3) The unloading speed of loose ash/lapilli samples (WI27) is increased for both, dry and steam flashing conditions, compared to a consolidated ash tuff of comparable porosity (WI22). Dry ash/lapilli samples were unloaded at a speed of 167–203 m/s whereas steam flashing led to an unloading speed of 305 – 353 m/s (Figure 2.11).
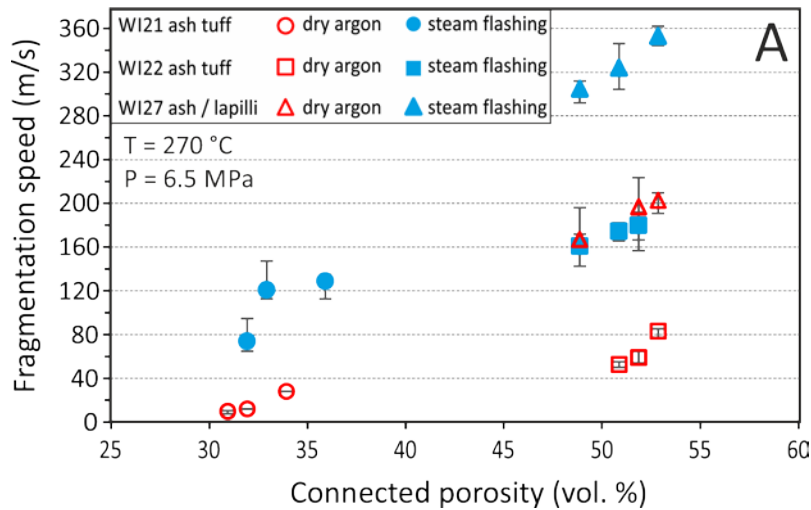
Figure 2.11: Fragmentation speeds of Whakaari samples due to dry argon gas expansion and steam flashing. All experiments were conducted at 270 °C and 6.5 MPa initial pressures. Fragmentation speed increases with porosity as well as steam flashing. The speeds obtained for the ash/lapilli samples correspond to the unloading of the sample out of the autoclave, thus termed unloading speed. In these experiments, further fragmentation of the particles may occur; however, it is not necessary. (Note: The error bars indicate the uncertainties in the determination of the fragmentation onset. Errors for the dry experiments with the ash tuffs are small leading to error bars smaller than the symbols used.).

2.5.3   Ejection speed of the particle front

The duration of the entire gas-particle ejection is on the order of 0.15 s to 0.25 s for the experiments with the ash tuffs and on the order of 0.10 s to 0.15 s for the ash/lapilli (Table 2.4). The velocity of the gas-particle mixture was measured by high-speed videography for each experiment (except WI22-6). Velocities of the particles travelling at the front of the ejected plumes were estimated by considering the average of several (≥ 5) particle velocities (Figure 2.12). The determination of the ejection speed is limited by the visibility of single particles within the plume of either argon gas and dust or steam and fine dust, respectively (Figure 2.12). Therefore the maximum velocity of particles ejected in steam flashing experiments, obtained by the technique of high-speed video analysis, is an approximation to the true maximum velocity. In addition, the fastest particles, if visible at all, are hard to track in two consecutive still frames.
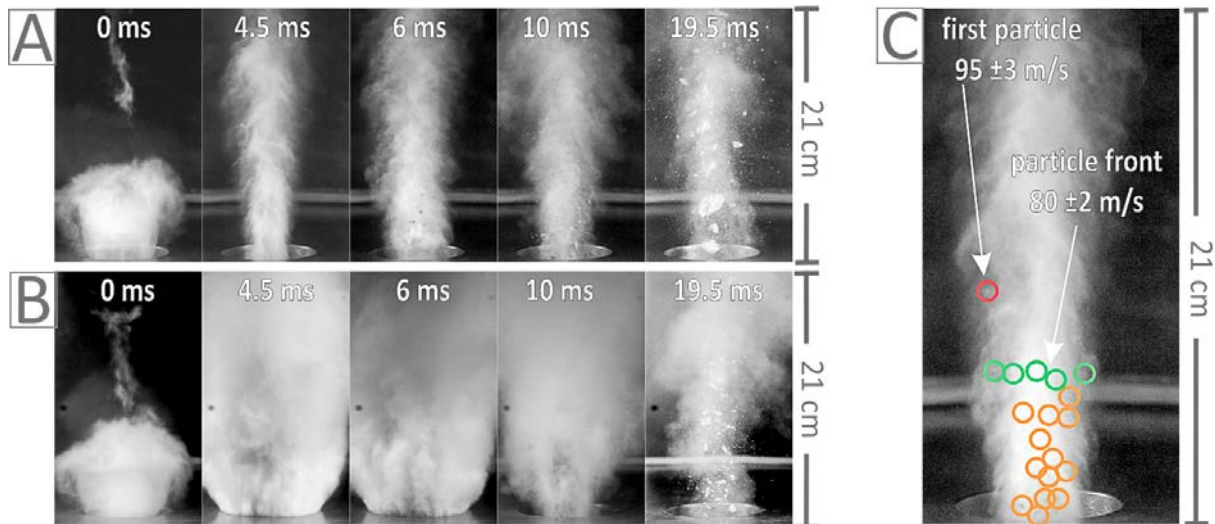
Figure 2.12: Sequence of still frames from high-speed camera recordings. (A) Images showing the front of the argon gas and argon–gas–particle mixture after fragmentation of a dry WI21 sample at 6.5 MPa and 270 °C. The narrow plume of argon gas contains large particles with a diameter of up to 1.5 mm. (B) Sequence showing the front of the argon gas followed by the dense and almost opaque steam and steam–particle mixture of a saturated WI21 sample fragmented in the presence of steam flashing at 6.5 MPa and 270 °C. Note: 19.5 ms after decompression, the particles within the steam jet are significantly smaller than particles produced in the dry experiment (A). (C) Still frame showing a single particle ejected at a higher speed ahead of the particle front. Note: Tracking of first particles arriving in the field of view is partly hindered by the opacity/poor visibility caused by steam, dust, and very fine particles.

The obtained ejection speeds of all three sample series (Table 2.4) are illustrated in Figure 2.13 showing the following dependencies: (1) at identical conditions (dry argon or steam flashing), the ejection speed of the ash tuff particle front increases with porosity. In case of dry fragmentation from 80–85 m/s for WI21 (Φ=32 %) to 122–133 m/s for WI22 (Φ=52 %) and for fragmentation dominated by steam flashing, ejection speed of particle front was enhanced from 125–162 m/s (Φ=34 %) to 181–195 m/s (Φ=50 %). (2) Within a samples series ejection speed is significantly increased in the presence of steam flashing. From 80–85 m/s to 125–162 m/s for WI21 and from 122–133 m/s to 181–195 m/s for WI22 respectively. (3) For both, dry argon and steam flashing conditions, ejection speed of loose ash/lapilli samples (WI27) are higher, compared to a consolidated ash tuff of comparable porosity (WI22). Ash/lapilli samples were ejected at a speed of 150–161 m/s under dry conditions and at a speed of 208–221 m/s in the presence of steam flashing.

For both ash tuffs, the ejection velocity of the gas-particle mixture is higher than the fragmentation speed in each experiment (Figures 2.11 and 2.13). In contrast, the maximum ejection speed of the loose ash/lapilli is lower than the unloading speed.
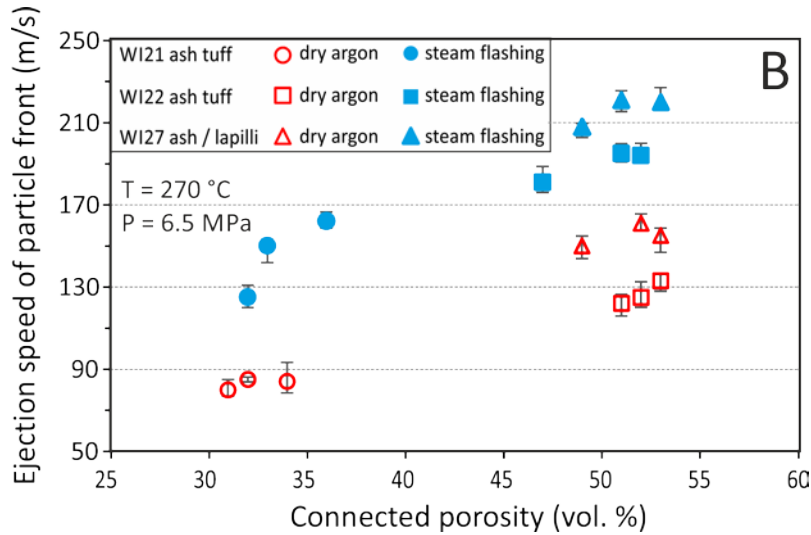
Figure 2.13: Ejection speed of the particle front in the presence of argon gas expansion and steam flashing. The ejection speed values correspond to the average of the velocities of several particles (≥ 5) traveling at the front of the gas–particle mixture. The ejection speed of the ash tuff increases with porosity and is lower than for the unconsolidated ash/lapilli. Steam flashing significantly enhances the ejection speed for all sample types (Note: The error bars reflect the extrema of each data point.).

Table 2.4: List of samples used for fragmentation experiments with experimental condition and porosity to quantify the fragmentation speed and the ejection speed of particles front. $\Delta t_{ejection}$ corresponds to the total duration (s) over which particle ejection occurs. Note: unloading speeds of WI27 samples are given under column fragmentation speeds ($V_{fragmentation}$).

Sample	Experimental condition	Porosity (%)	$V_{fragmentation}$ (m/s)	$V_{ejection}$ (m/s)	$\Delta t_{ejection}$ (s)
WI21-1	dry argon	34	28	84	0.24
WI21-2	dry argon	32	12	85	0.25
WI21-3	dry argon	31	10	80	0.25
WI21-4	steam flashing	36	129	162	0.20
WI21-5	steam flashing	32	74	125	0.22
WI21-6	steam flashing	33	121	150	0.20
WI22-2	dry argon	51	53	122	0.19
WI22-3	dry argon	52	59	125	0.20
WI22-4	dry argon	53	83	133	0.19
WI22-5	steam flashing	47	no record	181	0.16
WI22-6	steam flashing	49	161	no video	no video
WI22-7	steam flashing	52	180	194	0.15
WI22-8	steam flashing	51	174	195	0.16
WI27-1	dry argon	53	203	155	0.14
WI27-2	dry argon	49	167	150	0.15
WI27-3	dry argon	52	197	161	0.14
WI27-5	steam flashing	49	305	208	0.12
WI27-6	steam flashing	51	324	221	0.11
WI27-7	steam flashing	53	353	220	0.10

2.5.4 Particle size and shape

The evaluation of the particle-size distribution of the experimentally generated pyroclasts is shown in Figure 2.14. Due to the sealing between the plexiglass cylinder and the collector tank, as well as the adhesion of very fine particles on the lid and along the rim of the tank, a complete recovery of the very finest fraction was not possible; however, a minimum weight yield of 95 % was achieved. WI21 ash tuffs showed a peak in the particle-size distribution at phi = – 0.5 *(1.5 mm)* when fragmented dry with argon (Figure 2.14A). The samples fragmented by steam flashing exhibit a peak at a smaller phi-value between 0 and 1 *(1 – 0.5 mm)*. Dry argon fragmented WI22 samples demonstrate the highest particle fraction at phi-values between -3 and -1.5 *(8 – 3 mm)*, whereas the steam-flashing experiments enhanced the generation of fine particles, shifting the peak to phi = 1 *(0.5 mm)* (Figure 2.14B). The unconsolidated WI27 ash/lapilli particles showed grain size peaks at phi = 1 *(0.5 mm)*. In contrast to WI21 & WI22 a grain size distribution prior to experimentation (raw) was determined for the loose ash/lapilli, which is biased by a few coarser particles leading to a peak at phi = -3 *(8 mm)*. The shift of the grain size distribution curve from prior to post experimentation is evidence of fragmentation despite their lack of consolidation (Figure 2.14C). Fragmentation dominated by steam flashing increases the proportion of fine particles.
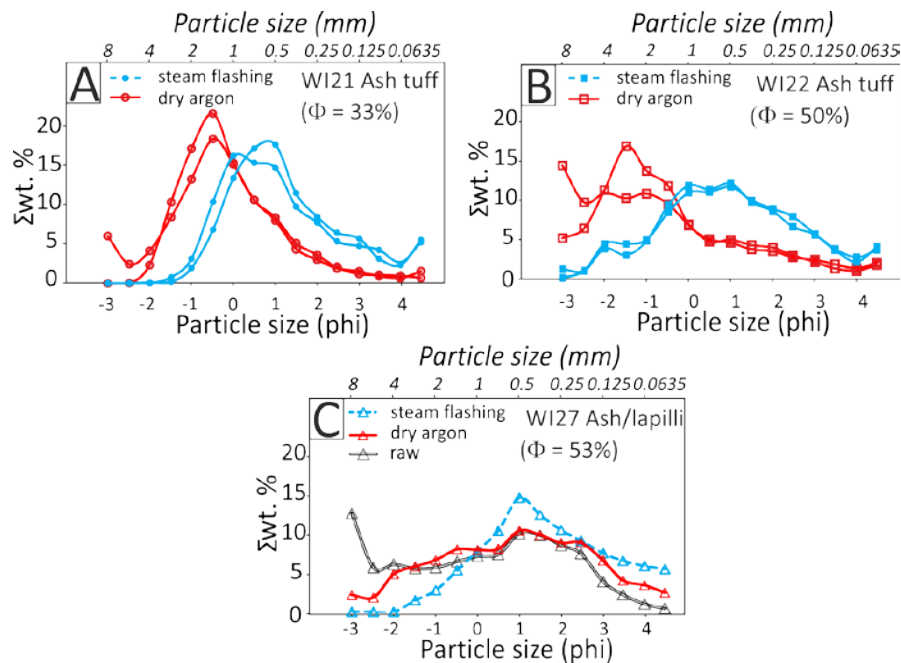
Figure 2.14: Particle size distribution plots showing the relation of weight percentage and particle size (phi, phi=−log2d, with d=particle diameter in mm) of rapid decompression experiments at 270 °C and 6.5 MPa. Fragmentation of ash tuffs with (A) 33% porosity and (B) 50% porosity as well as ash/lapilli (C) with 53% porosity due to dry argon gas expansion and in the presence of steam flashing. The grain size is decreasing to the right in all three plots, showing a shift to more fines with increasing porosity and a significant shift for fragmentation in the presence of steam flashing. For the unconsolidated ash/lapilli, the grain size distribution prior experimentation (raw) is also plotted (Note: Given porosities (Φ) refer to average values of experiments shown in the figure and might therefore deviate from average values given in Table 3.).

To quantify variations in particle shape, the three axes of the generated particles from experiments on WI21 and WI22 were measured and used to plot the S/L ratio and [(L-I)/(L-S)] form index with the standard deviation (Figure 2.15). In total, 134 particles with phi sizes ranging from -2.5 to -1.5 were used for the analysis of the particle shape as these phi sizes have been produced in every experiment and were measureable with a set of calipers. The shape of particles fragmented by steam flashing for sample WI21 was slightly different to particles fragmented by gas expansion, and also slightly different than any particles generated in the experiments on the sample WI22 (Figure 2.15). Nevertheless, the shape of the particles from the different experiments/conditions is not significantly different as the standard deviation bars of the individual samples show significant overlap.
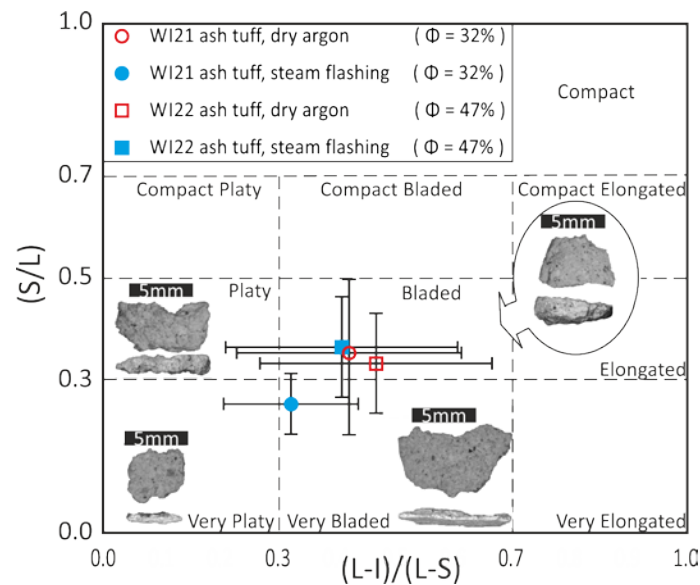
Figure 2.15: Particle shape of ash tuffs fragmented by argon gas expansion and in the presence of steam flashing plotted within grain shape fields developed by Sneed and Folk (1958). The grain shape was determined for particles ranging from −2.5 > phi > −1.5 (5.6 > phi > 28mm). Photomicrographs of particles showing the long versus intermediate and long versus small axes are additionally presented as a reference for all shape fields occupied by investigated ash tuff particles. (Note: Error bars indicate the standard deviation of the measurements. Given porosity values (Φ) are averaged on the samples investigated for the grain shape and might therefore deviate from the values given in Table 2.3).

2.6   Discussion

The presented results show that, under identical pressure and temperature conditions, eruptions accompanied by the process of liquid water flashing to steam are significantly more violent that those driven simply by gas expansion. Thus, steam flashing changes the conditions for and the progression of fragmentation.

2.6.1 Fragmentation threshold

The pressure applied during the fragmentation experiments of this study was set above the pressure determined in the experiments designed to delineate the fragmentation threshold in order to ensure full fragmentation and complete ejection. As noted above, the fragmentation threshold of WI21 and WI22 follows the well-defined trend of fragmentation threshold and porosity (Figure 2.10), and plots slightly below the fragmentation criterion postulated by Koyaguchi et al. (2008) based on experiments with pristine volcanic rocks from Spieler et al. (2004), Kennedy et al. (2005) and Scheu et al. (2006). The microstructure of these altered ash tuffs, is characterized by shards and fragments, cemented mainly by alunite and opal-A (Figure 2.5; Heap et al., 2015). This complex microstructure containing altered particles bound by secondary precipitated minerals exhibits a slightly lower tensile strength than that of pristine volcanic rocks and subsequently, fragment slightly below the classically defined fragmentation threshold of Spieler et al. (2004), still obeying the fragmentation criterion.

2.6.2 Fragmentation and ejection speed

The fragmentation and ejection speed obtained in the experiments is controlled by the initial overpressure within the pores, the connected porosity, the permeability, and the strength of the sample (Scheu et al., 2006; Richard et al., 2013). In addition, the state of the decompressing fluid is an important control, as clearly demonstrated. Both, the fragmentation and ejection speed increases significantly for those samples fragmented in the presence of steam flashing. The connected porosity allows us to quantify the amount of gas or superheated water stored within the sample. Indeed, Scheu et al., (2006) demonstrated that fragmentation speed is highly influenced by porosity using fragmentation experiments on samples containing different porosities. They showed that fragmentation speeds of 20 and 43 m/s respectively were achieved, when fragmenting samples with 33 and 54 % porosity at an initial pressure differential of 10 MPa. These results, for the case of fragmentation by pure argon gas expansion are similar to those for dry argon experiments with WI21 and WI22 in this study. In contrast, during the decompression from 6.5 MPa to ambient pressure, the isothermal expansion of water within the pores and the instantaneous flashing to steam causes a 30-fold larger volume increase compared to pure argon gas expansion under these conditions. Thereby, this process is significantly more violent and energetic (Wohletz, 1983) leading to a faster fragmentation of the sample (as shown in Figure 2.11). As the fragmentation process controls the velocity of the gas particle mixture (Alatorre-Ibargüengoitia et al., 2011), the ejection speed of the particle front increases with an increase in the fragmentation speed. Therefore, ejection speed increases with porosity and is significantly higher during steam flashing than for simple gas expansion.

During decompression, the potential energy of gas trapped in pores is converted into kinetic energy as gas expands (Aldibirov and Dingwell, 2000). In this process, part of the energy is consumed by fragmentation and the remaining kinetic energy is left to expel the

fragments (Alatorre-Ibargüengoitia et al., 2010). During steam flashing experiments, the scenario is slightly modified as a change in phase is additionally responsible for the gas volume increase powering the fragmentation and ejection processes; yet, the balance in energy used by fragmentation and particles expulsion remains.

In the experiments with loose ash/lapilli (WI27), a grain size reduction was observed, which is assumed to be caused by fragmentation, fracturing, and/or comminution. As a consequence of only very minor energy consumed by fragmentation, a higher amount of energy is available for the main energy sinks: namely, the lofting, acceleration, and ejection of the particles. This leads to faster unloading speeds for unconsolidated WI27 compared with the fragmentation speeds of WI22, even though these two samples exhibit similar values of connected porosity. Further, the surplus energy also leads to higher ejection speeds of the particle front for the unconsolidated WI27 samples compared to the cemented WI21 and WI22 samples for both dry and steam flashing experiments (Figure 2.13). Alatorre-Ibargüengoitia et al. (2011) observed that the ejection velocity of the gas-particle mixture is higher than the fragmentation speed of rock samples fragmented by gas expansion. The results for the ash tuff experiments are in agreement with this observation. Ejection speed of particles in the presence of steam flashing may even be still faster than reported here, as the highest speeds might not have been estimated due to poor visibility during initial phase of ejection of the fastest particles.

The experiments with loose material (WI27) showed that the ejection speed of the first trackable particles is higher than the ejection speed of the ash tuffs but lower than the unloading speeds. In addition, the unloading of the ash/lapilli (in both dry argon and steam flashing experiments) is faster than the ejection speed of particles front.

2.6.3   Particle size analysis

The production of fine particles in the experiments quantified by the particle size distributions of all fragmented samples are in agreement with the trend identified by Kueppers et al. (2006): an increased production of fine particles results from higher fragmentation energy as a consequence of higher gas volume stored in high porosity samples. Our work shows a similar effect is induced by steam flashing as the gas volume increases significantly during the phase change. The results support previous assumptions by Wohletz (1983) and Cronin et al. (2003) that steam flashing reduces the particle size in natural eruptions and in shock-tube experiments (e.g., Rager et al., 2013; Foote et al., 2011). Rager et al. (2013) investigated the effect of steam flashing on the production of fine particles during the fragmentation of sandstones with an average connected porosity of 27 %. The grain size distribution of saturated sandstone fragmented at 300 °C and 15 MPa showed a clear increase in the production of fine particles compared to the control samples fragmented by pure gas expansion.

Particle size analysis prior to and post fragmentation showed that fragmentation processes also occur in experiments with loose samples (WI27) (Figure 2.14). The few coarse

particles responsible for the peak in the particle size distribution plot (phi = -3) fragmented during decompression as they could not be observed in the high-speed camera recordings. In addition, the peaks in the particle size plot of fragmented ash tuffs (WI21 and WI22) (Figures 2.14A, B) are not predetermined by the initial particle sizes of the shards and fragments, which are cemented by alunite and opal-A (Figure 2.5). In fact, there seems to be no correlation between the dominant particle size of the original clastic rock and the dominant size of fragments. Indeed, most particles generated by fragmentation are aggregates of several cemented particles (Figure 2.15).

2.6.4 Particle shape analysis

The shape analysis of investigated particles showed that for the Whakaari ash tuffs neither sample type nor fragmentation fluid state has a significant influence on the shape (i.e., they plot within the same shape fields; Figure 2.15). Here, fragmentation both with and without steam flashing involves fracturing parallel to the decompression front and generate particles with platy or bladed shapes consistent with previous experimental studies (Rager et al., 2013). Although the mean shape of the WI21 particles generated by steam flashing plots within the field of very bladed particles, no significant difference (considering the standard deviation) exists within the investigated particles. Results of the grain shape analysis slightly contrast with the findings by Rager et al. (2013) who investigated the shape of volcaniclastic sandstone particles produced by fragmentation experiments with a different degree of sample saturation at 177 °C and 300 °C, respectively. Their study showed that, according to the (S/L) and (L-I)/(L-S) ratio, particles generated by fragmentation at 15 MPa are characterized by a bladed shape and plot within or close to the 'bladed' field. However, they showed that full sample saturation (steam flashing) caused a change of the particle shape in comparison to partial sample saturation, as it leads to the generation of compact bladed particles. This effect is not supported by the analysis of Whakaari ash tuff particles that were fragmented at 6.5 MPa.

Most likely the shape could be controlled by the initial pressure as well as sample microstructure and inhomogeneity. As a result, caution should be exercised here on the subject of using the shape of particles to distinguish between phreatic or gas blast eruptions. Further studies are needed to shed more light on this complex relation.

2.6.5 Eruption scenarios

Due to its active hydrothermal system, Whakaari's subsurface is characterized by intense fluid migration, storage, and emission. Hydrothermal fluids exist in both liquid and gaseous states within the hydrothermal system at Whakaari and the obtained results have implications for both types of eruption (liquid and gaseous).

Both eruption scenarios envisaged pressurization of the hydrothermal system to occur if the volume of the uprising fluid supply exceeds the volume of fluids emitted at the surface. One of the main controlling factors here is the permeability of the rocks within the

hydrothermal system. Our permeability data (Table 2.3) highlights that the rocks comprising the hydrothermal system at Whakaari can vary by at least two orders of magnitude. This difference in permeability is likely related to the differences in rock microstructure (Figures 2.4–2.5): WI21 is less porous and contains a higher amount of secondary minerals precipitated within the pores (Figure 2.5). Hydrothermal sealing has been discussed in several studies (Edmonds et al., 2003; Christenson et al., 2010; Vignaroli et al., 2014; Wyering et al., 2014). Sealing occurs by the deposition of silica and other hydrothermal minerals within the pore and fracture network. Such precipitation is likely to reduce the porosity and permeability of the deposits and will eventually lead to the pressurization of the hydrothermal system. Likewise, dissolution during hydrothermal alteration can increase the permeability of rocks (Wyering et al., 2014).

Eruptions, with or without steam flashing, occur when the pore pressure exceeds the combination of lithostatic and hydrostatic pressure plus the tensile strength of the surrounding rock (Browne and Lawless, 2001). Several triggers may cause the breaking of a mineralogical seal and lead to decompression and hence the expansion of fluids leading to an eruption (Figure 2.16).

Here the events following full fragmentation and ejection of the sample (i.e. after the decompression of the fluid within the pore network) are focused. In the case of gaseous fluids, the expansion and therefore the explosivity of an eruption is less violent than for steam flashing of fluids that are initially liquid and change to a gaseous phase during decompression. Thermodynamics dictate that water at 270 °C and 6.5 MPa will increase in volume 30 times when changing phase into a gas at atmospheric pressure. This volume increase due to the phase transition of water is the crucial reason for the differences in the fragmentation and ejection dynamics of the investigated experiments. Steam flashing causes higher fragmentation speeds, higher ejection speeds and an increased production of fine particles. The hazard potential of such eruptions is therefore much greater than that of gas eruptions, in terms of energy, trajectory distances of ballistics, and size of the area affected by ejecta. Large amounts of very fine particles in a plume represent a persistent, long-lived hazard for the surrounding area. Moreover, eruptions at Whakaari are likely to involve high amounts of unconsolidated material (Figure 2.2B). As our results showed, the ash/lapilli (WI27) was ejected at higher speeds and, thus, the probability of ejecta reaching greater distances and spreading over wider areas is increased. Steam flashing phreatic eruptions, which may prove to be the least predictable of all eruptions, are apparently also those containing the highest specific energies for fragmentation and its consequences not only at Whakaari but also at any other hydrothermal system worldwide.
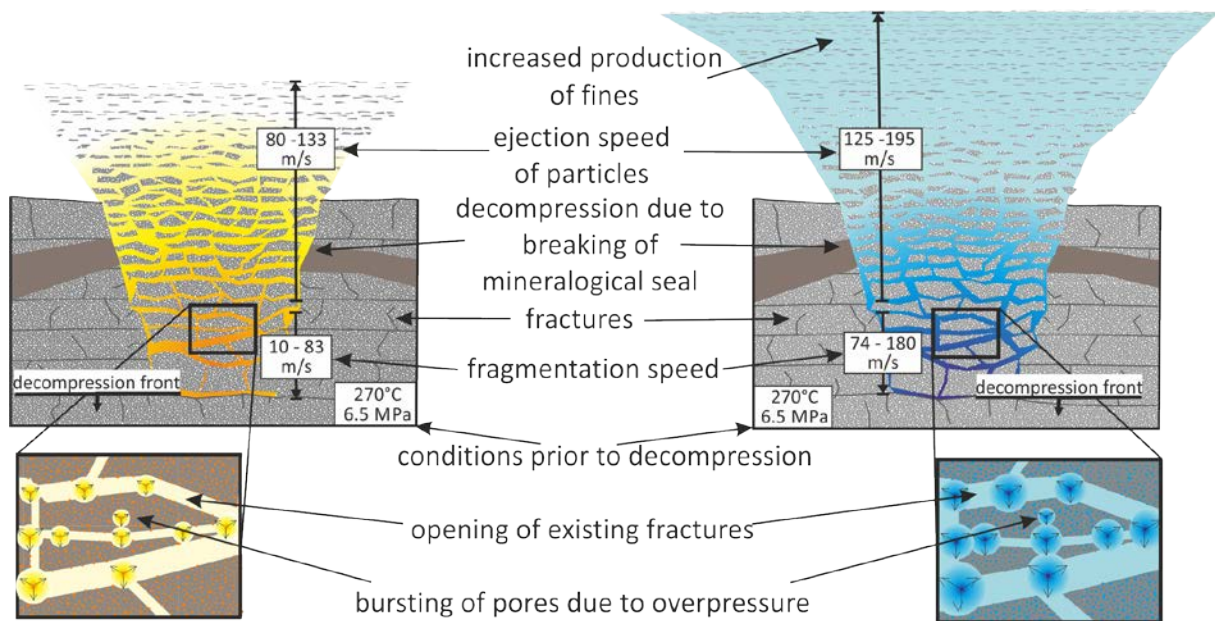
Figure 2.16: Schematic model of eruptions driven by gas expansion (left) and steam flashing of liquid water (right). A mineralogical seal allows pressurization of the system; breaking this seal triggers the eruption and leads to a sudden pressure drop. The expansion of gas or liquid water flashing to steam within the pore and fracture network is fragmenting and ejecting the rocks. Initiated at identical pressure and temperature condition the two processes cause differences in the explosivity and therefore violence of the eruption manifested in significantly higher fragmentation and ejection speeds, as well as higher amounts of fines in the presence of steam flashing.

2.7   Summary and conclusions

Rapid decompression experiments on hydrothermally altered samples (ash tuffs and unconsolidated ash/lapilli) from Whakaari have been conducted. The experiments, designed to mimic phreatic eruptions, explore the effect of different fluids (dry argon gas versus superheated liquid water) on the fragmentation behavior. The initial conditions were set at 270 °C and 6.5 MPa; rapid decompression to atmospheric pressure triggered fluid expansion, fragmentation and ejection of particles. Our results show the influence of argon expansion versus steam flashing as well as sample type and secondary hydrothermal alteration (among others alunite precipitation) on the fragmentation threshold and speed as well as the particles size, shape and ejection velocities.

(1) The rapid decompression experiments revealed that fragmentation and ejection speeds of two ash tuffs, cemented by alunite and amorphous opal, increase with increasing porosity and that both are significantly enhanced in the presence of steam flashing;

(2) The energy consumption by fragmentation leads to reduced ejection speeds of cemented tuffs in comparison to unconsolidated samples;

(3) Fragmentation dominated by steam flashing also results in increased fragmentation energy and increased proportion of fine particles;

(4) For the investigated Whakaari samples the phase of the fluid just prior to fragmentation showed no significant influence on the particle shape as revealed by analysis before and after fragmentation. Both steam flashing and pure gas expansion produce platy or bladed particles from fracturing parallel to the decompression front.

In summary, under identical pressure and temperature conditions, eruptions accompanied by the process of liquid water flashing to steam are significantly more violent than those driven simply by gas expansion. Phase changes during decompression together with the type and amount of cementation are important fragmentation variables and should therefore be considered for hazard assessment and modeling of eruptions in hydrothermally active environments.

3 Influence of hydrothermal alteration on phreatic eruptions in Campi Flegrei, Italy

Figure 3.1: Vigorous degassing at Pisciarelli fumarole, Campi Flegrei (Italy).

This page was intentionally left blank.

3.1   Introduction

Solfatara crater and the adjacent fumarole in Pisciarelli are located within the Campi Flegrei (CF) caldera to the west of Naples (Italy). This area shows one of the largest fumarolic manifestations known, and the surrounding rocks are affected by intense hydrothermal alteration (Caliro et al., 2007). Campi Flegrei caldera (Figure 3.2) hosts a large, complex hydrothermal system, active (at least) since historic times (Mormone et al., 2011), which is characterized by periods of ground uplift (bradyseism) accompanied by seismic events.
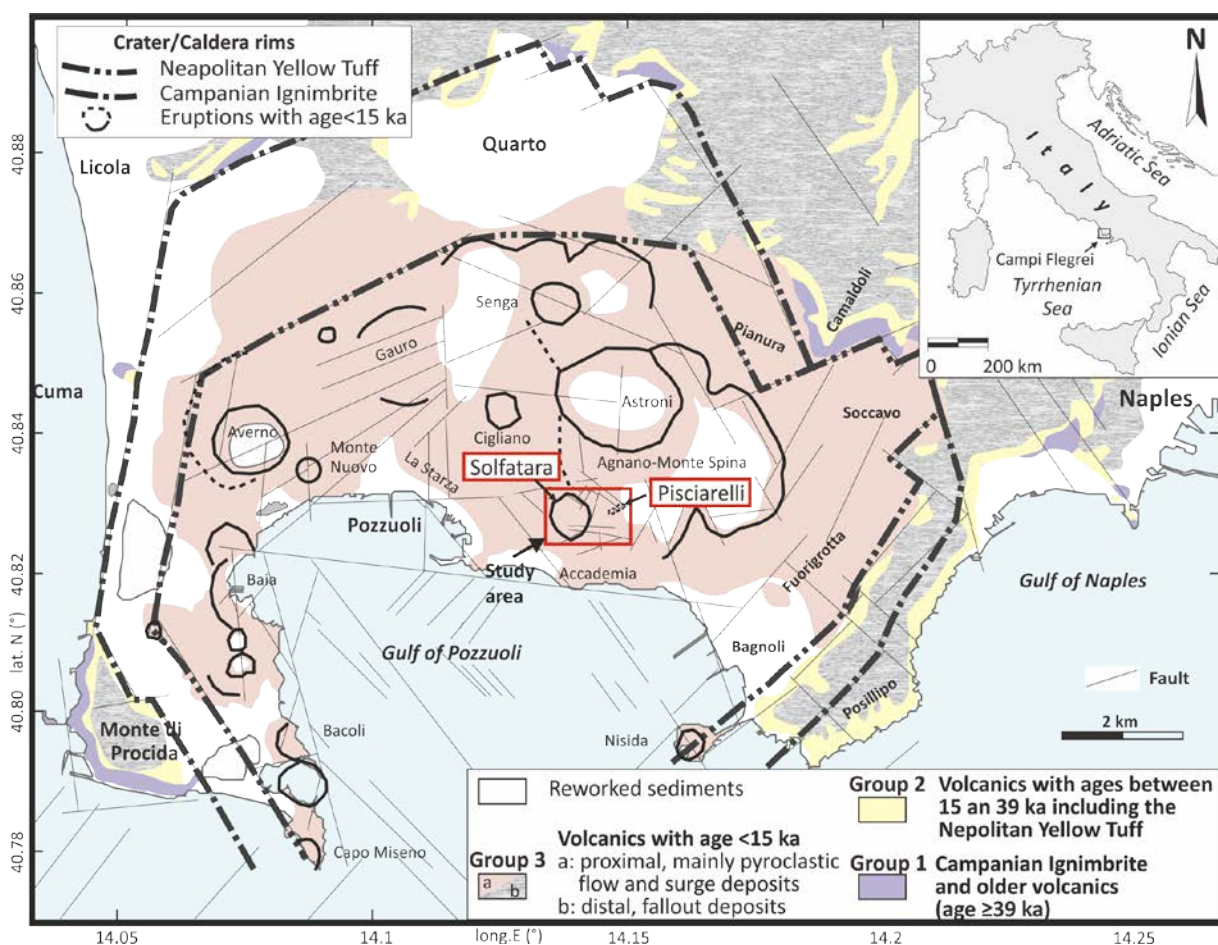
Figure 3.2: Structural-geological map of Campi Flegrei showing the location of Solfatara and Pisciarelli (modified after Isaia et al., 2015).

At depth it can be assumed that magmatic gases mix with hydrothermal liquids and form a rising gas plume (Caliro et al., 2014). At the top of the rising plume, a single phase gas zone at shallow depth (300–100 m) develops (Caliro et al., 2007), where fluid circulation and fluid-induced alteration of the host rock are believed to influence pressurization events (Bruno et al. 2007). Permeability decrease due to the alteration process, could however cause pressurization and, in turn, result in phreatic eruptions at depths of a few hundred meters. The risk of such events was analyzed by Italiano et al. (1984) who constructed a

thermodynamic model based on the gas emission rates at Solfatara. A similar scenario was recently reconstructed by Isaia et al. (2015) on the base of stratigraphic field analysis of ejected material. Their study indicates a multiphase eruptive evolution of the Solfatara crater derived from an early phreatic phase excavating the pre-eruption basement, followed by phreatomagmatic events. Alteration could however also enhance permeability, thereby hindering the pressurization in the subsurface and, in turn, reducing the risk of an eruption. A recent mineralogical and isotope study by Piochi et al. (2015) concluded that the CF caldera represents a low sulfidation system grading in its most active centers (Solfatara-Pisciarelli) into the high sulfidation regime. They additionally proposed, that the increasing CO_2-degassing-surface area results from fracturing of the surficial rocks with major leaching of gas favoring increased outgassing.

The aim of this study is to investigate the influence of hydrothermal alteration on rocks, outcropping at the sites of the main hydrothermal activity within the CF caldera (Solfatara and Pisciarelli; Figure 3.3). Collected samples have been geochemically and mineralogically investigated in particular with respect to their degree of alteration. The effects of alteration on rock physical and mechanical properties have been measured and experimentally determined. This analysis included rapid decompression experiments at elevated temperatures to simulate possible phreatic eruption conditions whereby eruptive processes of this type of event and the fragmentation behavior of the involved rocks were studied. For the first time fragmentation experiments in the presence of steam expansion are presented and compared with control experiments, driven by pure argon gas expansion in order to best mimic the possible conditions at the investigated sites. Additionally, the size of experimentally-generated pyroclasts, as well as the amount and composition of fine particles have been analyzed and evaluated

3.2 Geological setting

Campi Flegrei is a densely-inhabited area located west of Naples characterized by an active resurgent caldera system (e.g. Vitale and Isaia, 2014, and reference therein) . Since the second major caldera collapse, which formed the Neapolitan Yellow tuff ~15 ka ago, a high level of volcanic activity has produced more than 70 explosive eruptions, separated by rest periods of variable length (e.g. Di Vito et al., 1999; Orsi et al., 2004; Isaia et al., 2009). These eruptions, were predominantly phreatomagmatic with minor magmatic events occurring along the structural boundaries of the caldera as well as along faults inside the caldera, producing several tuff cones and tuff rings (Di Vito et al., 1999; Orsi et al., 2004; Costa et al., 2009; Smith et al. 2011). A historic eruption formed the Monte Nuovo tuff cone (1538; Guidoboni and Ciuccarelli, 2011). Intra-caldera collapses of variable size followed such events with minor volumes of erupted magma (e.g. Agnano-Monte Spina, AMS) (de Vita et al., 1999; Di Vito et al., 2011; Isaia et al., 2004, 2015). The volcanism has also included phreatic events and the formation of maar-diatreme structures, as recently postulated for

the Solfatara crater (Isaia et al., 2015). Solfatara volcano is part of a cluster of vents within less than 2 km^2, located at the southwestern rim of the AMS caldera (Figure 3.2), (Isaia et al., 2009). The reactivated volcanic activity started after the AMS Plinian eruption (~4.5 ka; Smith et al., 2011) after a refilling of the reservoir at a depth of less than 3 km and generated vents in the central area of the caldera including Solfatara crater (Isaia et al., 2009). Solfatara crater developed during a maar-diatreme evolution 4200 yr. B.P. and presently hosts very intense hydrothermal and fumarolic activity both inside the crater as well as on the eastern flanks towards Via Antiniana and the Pisciarelli area. The latter has exhibited a significant increase in degassing activity over the past 10 years marked by i) a widening of the hydrothermal area, ii) an increase in temperature and gas emissions and iii) the formation of new vents (Chiodini et al., 2012, 2015; Troiano et al., 2014; Isaia et al., 2015). The majority of the wall rocks affected by alteration at both sites represent pre-Agnano-Monte Spina (pre-AMS) and Agnano-Monte Spina (AMS) volcanic deposits (Isaia et al., 2009, 2015).

3.2.1 Hydrothermal system

The level of historical knowledge surrounding the history of the CF hydrothermal system is unsatisfactory. Currently the Solfatara area, including Pisciarelli and Via Antiniana, is the hydrothermally most active part of one of the largest fumarolic manifestations worldwide. It consists of a) a deeper-seated zone and b) a shallow zone; interacting with each other (Caliro et al., 2007).

Changes within the deeper-seated hydrothermal system have been caused by repeated injections of magmatic fluids in the past (Chiodini et al., 2012), where mixing with liquids of meteoric origin occurred (Caliro et al., 2014). These injections led to the pressurization of the system resulting in periods of ground uplift (Orsi et al., 1999; Vilardo et al., 2010) accompanied by increased seismicity (Orsi et al., 1999; D'Auria et al., 2011). The magmatic fluids appear to derive from two sources: (1) a deep stable magma chamber at approximately 8 km depth, which has fed volcanism over the last several thousand years (Mangiacapra et al., 2008; Arienzo et al., 2010), and (2) a shallower magma reservoir, intruded approximately at 4 km depth during the unrest episode occurring from 1982 to 1984 (Moretti et al., 2013, and references therein). The mixing of these fluids occurs at high temperature (>350 °C) at the base of the hydrothermal system (2.0–2.5 km), from which the rise of a plume (gas and liquid) to shallow depths is largely controlled by a volcano-tectonic system of a complex collapsed maar-diatreme structures (Isaia et al., 2015). According to Caliro et al. (2007) a single-phase gas zone exists at shallow depth (100–300 m). But recent geophysical (ERT) studies have revealed the existence of a two-phase system represented by liquid- and gas-dominated zones in the subsurface of Fangaia mud pool and the fumaroles of Bocca Grande (BG) and Bocca Nuova (BN) (Figure 3.3–3.4), respectively (Byrdina et al., 2015).

The thermal energy release associated with the surficial gas emissions represents a major proportion of the energy balance of the CF caldera (Cardellini et al., 2003; Chiodini et

al., 2001, 2011). The fumarole temperatures measured at the surface range up to 165 °C and 160 °C for BG and BN, respectively and up to ~115 °C for Pisciarelli (Valentino et al., 1999; Chiodini et al., 2015). The main components of the fumarolic effluents are H_2O and CO_2, followed by H_2S, H_2, N_2 and CH_4 (Caliro et al., 2007). Due to the buffering of magmatic fluids by the large hydrothermal system, components like SO_2, HCl and HF are not detected at the surface (Chiodini et al., 2001; Moretti et al., 2013). Sulfate concentrations in the Pisciarelli mud pool are relatively high and reach up to 4,600 ppm (Cennamo et al., 2002). The substantial release of CO_2 by both fumarolic and diffuse degassing within the Solfatara-Pisciarelli area is anomalously high (>2000 ton d^{-1}), and is typical of volcanoes in eruptive phases (Caliro et al., 2014, and references therein).

3.2.2 Hydrothermal alteration

Deep system

In the geothermal exploration program of the Agip-Enel Joint Venture several deep drillings (e.g. San Vito 1) have been conducted in the Campi Flegrei caldera since the 1970's. These were located beyond the high-outgassing zone investigated in this study (Agip, 1987). Drill log information was used to analyze the fluid-rock interaction at depth (<2800 m) that has produced a suite of hydrothermal alteration minerals leading to increasing rock density and a corresponding decrease in porosity (Mormone et al., 2011) as well as an increase in shear and tensile strengths of the rocks (Vanorio and Kanitpanyacharoen, 2015). The formation of argillic phases, especially in the shallow alteration zones of these drillings and accompanied by a decrease in rock permeability, favors the interpretation of the creation of a cap rock within the hydrothermal system (Todesco et al., 2003; Bruno et al., 2007). Rock samples from the drill cores obtained during the Campi Flegrei Deep Drilling Project (CFDDP), located in the eastern sector of the caldera, have been investigated recently (De Natale and Troise, 2011). Drill log analysis has shown a hydrothermal alteration-induced rock mineralization leading to the filling of voids and veins (Mormone et al., 2015) and a reduction of rock permeability (Carlino et al., in review). In general, the mineralogy detected in these drill holes is characteristic for a neutral-pH, low-sulfidation system (Piochi et al., 2015).

Surficial system

Steam-heated environments, in the upper portions of hydrothermal systems, in which sulfuric acid is created at or above the water table by the oxidation of H_2S ($H_2S + 2O_2 = H_2SO_4$), lead to an advanced argillic alteration (Rye et al., 2005). This type of alteration is characterized by acidic fluids and the formation of amorphous silica and alunite (Pirajno, 2009), which is a very common feature in surficial regions of high-sulfidation epithermal systems, often referred to as solfataric alteration (Bishop et al. 2007). In the presence of abundant sulphate ions and Al-rich protoliths, alunite forms veins, lenticular

bodies and may even replace entire rock masses (Pirajno, 2009). The formation of alunite from K-feldspar follows the reaction:

$$3K(AlSi_3O_8) + 3H_2SO_4 \rightarrow KAl_3(OH)_6(SO_4)_2 + 9SiO_2 + K_2(SO_4)_2$$
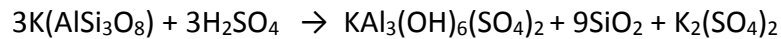
(Höller, 1967). During the transition from K-feldspar to alunite, SiO_2 is released (Hedenquist et al., 2000). This release in combination with the residual SiO_2, caused by the extreme leaching of the alkali cations by acidic fluids (pH 1.3–2.5) at high temperature, may lead to the formation of vuggy silica (Bruno et al., 2007; Boyce et al., 2007). As a result, the K-feldspar and mafic silicate phases within the trachytic host rocks are completely altered (Pirajno, 2009).

The Solfatara-Pisciarelli area is characterized by the surficial formation of alunite and amorphous silica (De Gennaro et al., 2000; Bruno et al., 2007; Pinto et al., 2007). A recent study based on SEM and isotope analysis confirms the genesis of alunite at Solfatara and Pisciarelli via hydrolysis of K-feldspar (Piochi et al., 2015). In contrast, the low pH of fluids hinders the formation of kaolinite (Zimbelman et al., 2005) at Pisciarelli (Valentino et al., 1999) and at the highly degassing vents at Solfatara (Bruno et al., 2007). Due to the lack of wells in the proximity of Solfatara crater, a detailed distribution of hydrothermal alteration minerals in the subsurface is not yet possible (Bruno et al., 2007). Piochi et al. (2015) have developed a conceptual model of the Campi Flegrei hydrothermal system, based mainly on geochemical and mineralogical data as well as on input from drilling studies. They propose an acid sulfate environment along the SW–NE section from Solfatara crater to the Pisciarelli area at shallow depth of a few hundred meters and high-sulfidation zones associated to the hydrothermal vents of Solfatara and Pisciarelli. Previous studies examined the effects of surficial alteration on rocks from the Solfatara crater walls (lavas and pyroclastic rocks) by investigating rock physical and rock mechanical properties (Pola et al., 2012, 2014). Those results indicate that an increasing degree of alteration leads to an increase in porosity causing a decrease of elastic wave velocities, as well as tensile and compressive strengths.

3.3 Investigated lithologies

In order to investigate the influence of hydrothermal alteration on rock properties, and as a consequence to infer implications for possible phreatic eruptive processes, two areas of intense hydrothermal activity (Solfatara crater and Pisciarelli area) were chosen as sampling sites (Figures 3.3–3.4).

Rock samples from AMS and pre-AMS lithostratigraphic units, exhibiting variable degrees of alteration have been collected (Figure 3.5). These sequences represent the oldest rocks exposed in the Solfatara-Pisciarelli area (Figure 3.4–3.5) and consist of pyroclastic fallout, coarse to fine-ash beds, and pyroclastic density current deposits (Isaia et al., 2015). Post-depositional processes and alteration have led to the consolidation and compaction of the deposits, which have been transformed thereby from loose deposits to solid rocks.
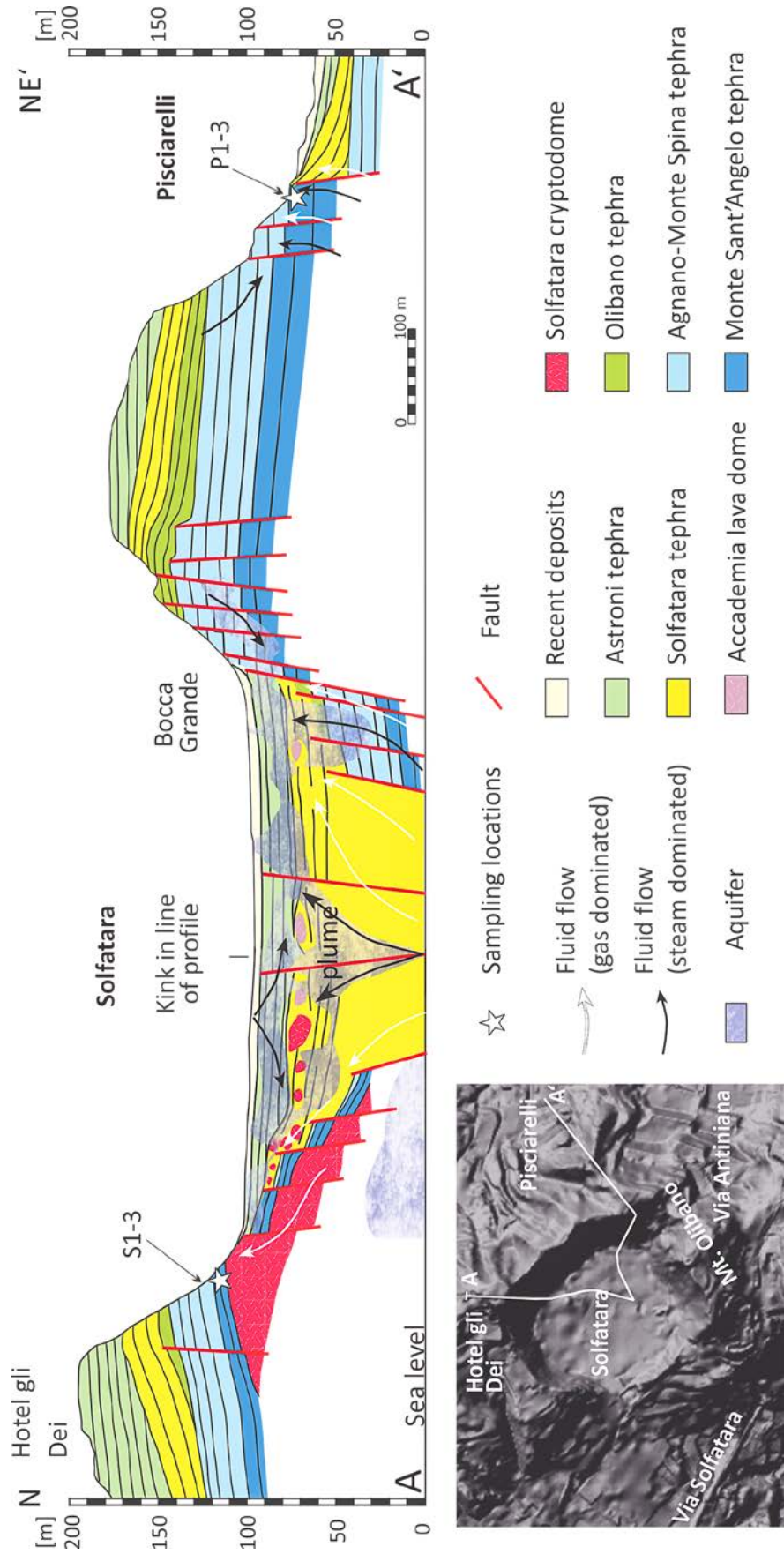
Figure 3.3: Geological cross section (2x vertical exaggeration) of the study area showing stratigraphic units, shallow fluid flow and sampling locations (modified after Isaia et al., 2015).

Samples were selected based on observable differences in macroscopic texture, color and particle size after the removal of surficial encrustations and weathering effects. Two blocks from the vicinity of the Solfatara cryptodome were collected (Figure 3.4; see also Isaia et al., 2015): one block of a pyroclastic current deposit comprising a lesser altered core (S1) and a more altered rim (S2), and a heavily altered block from a second current deposit (S3) (Figure 3.5). Within the Pisciarelli area, three blocks from a several-meter-thick consolidated ash fall sequence were collected (P1, P2, P3) (Figure 3.5).
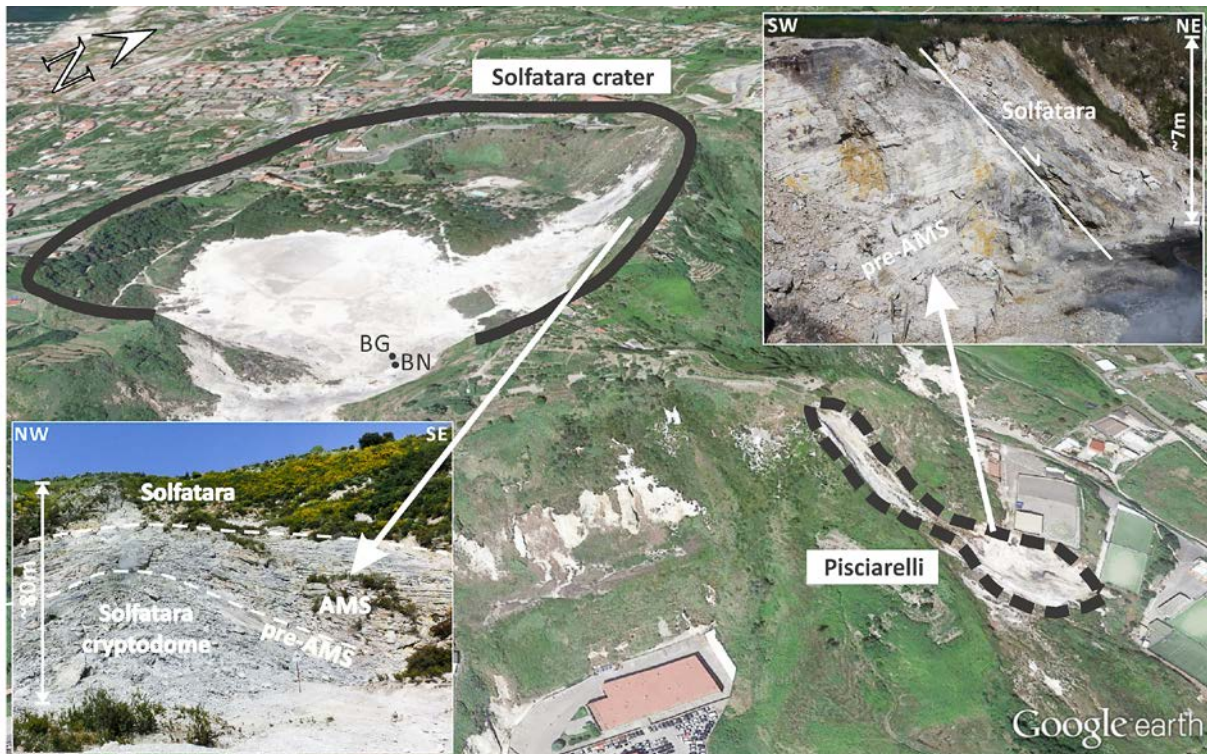
Figure 3.4: Google Earth™ image of Solfatara crater and Pisciarelli fumarole. Insets show details of the sampling locations.
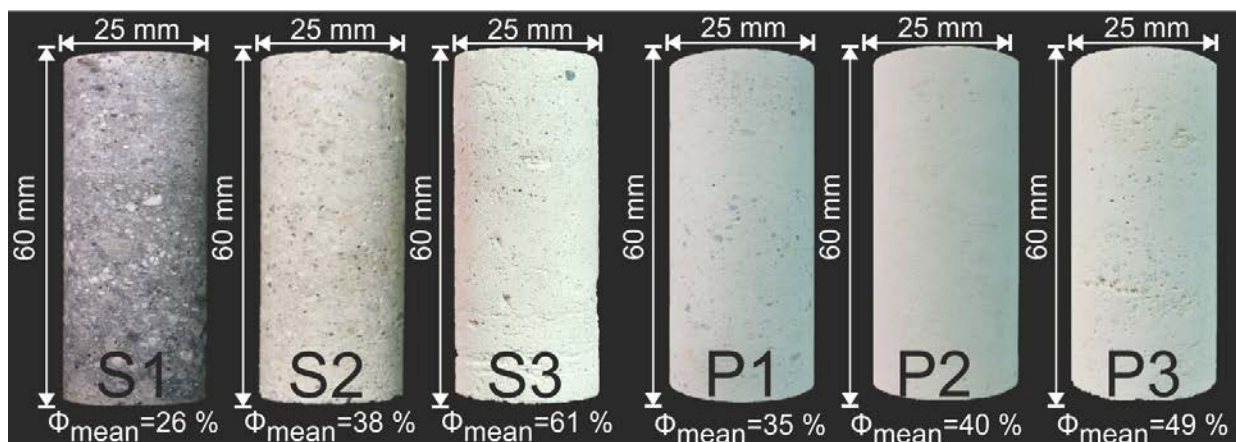
Figure 3.5: Photographs of the investigated sample series from Solfatara (S1-S3) and Pisciarelli (P1-P3). Samples show differences in macroscopic texture, color and particle size in respect to alteration.

3.4 Methods

3.4.1 Mineralogical and geochemical characterization

Mineralogical and geochemical analysis was conducted by optical microscopy as well as by wavelength dispersive X-ray fluorescence (WD-XRF) and X-ray powder diffraction (XRD). To further investigate the intensely-altered samples electron probe micro analysis using an energy-dispersive system (EPMA-EDS) was employed.

XRD analysis was conducted using a General Electric XRD 3003 TT diffractometer (CuKα, graphite monochromator, step-scan 0.0013° 2θ increments per second, counting time 100s per increment, 30 mA, 40 kV). For this analysis samples were disaggregated and ground for 8 minutes with 10 ml of isopropyl alcohol in a McCrone Micronising Mill using agate cylinder elements. Phase identification was conducted with the interface Rayflex ANALYZE (Putz and Brandenburg, 2003). The whole rock element compositions were determined by WD-XRF analysis (Philips, MagiX Pro). Major and minor elements were measured using glass beads prepared by fusion of 1 g sample and 9 g SPECTROMELT A12 (66% di-lithium tetraborate, 34% lithium metaborate) in a Panalytical Eagon 2 furnace fusion system. SO_3 was measured by XRF analysis of powder tablets. Therefore 8 g of the sample powder was mixed with 2 g of Merck Hoechst wax C micropowder ($C_{38}H_{76}N_2O_2$), homogenized and pressed with P=15 bar for >1 minute. Additional geochemical information was attained by a Cameca SX 100 (EMPA) equipped with a Bruker AXS XFlash Detector 3001. Chemical composition resulting from WD-XRF analysis allowed determination of the CIA, which is one of several indices proposed in literature to characterize the alteration degree of different rocks (Pola et al., 2012, 2014, and references therein). The index, based on the weight percentage ratios of major elements, is applied to correlate the degradation trend exhibited by rock physical and mechanical properties. For further information concerning formula and references of the index, please refer to Chapter 1.2.

3.4.2 Rock physical properties

Throughout this study, cylinders of all blocks sampled were cored perpendicular to the layering for the determination of rock physical properties. Bulk density, matrix density, and connected porosity of dry (oven-dried at 65 °C for 24 h), cored cylinders were measured using a helium pycnometer (Ultrapyc 1200e®, Quantachrome, USA) at the LMU. A portable air permeameter was used to measure the permeability of samples in the field (New England Research, TinyPerm III). This handheld device calculates the Darcian permeability based on the monitored response function of the transient vacuum at the interface between the nozzle and the rock during the evacuation of air from the rock (Possemieurs et al., 2012; Vignaroli et al., 2015; Farquharson et al., 2015, Figures 3.6). Additionally gas permeability measurements of selected cylindrical samples (40 mm length; 20 mm diameter) were conducted under a confining pressure of 1.0 MPa at the École et observatoire des sciences

de la Terre (EOST)–Université de Strasbourg. Further, benchtop P-wave velocity of dry, cylindrical samples (60 mm length; 25 mm diameter) was determined at the LMU.

Figure 3.6: (A) Portable permeameter TinyPerm III during field measurement and (B) TinyPerm app on an Android device permitting wireless data collection.

3.4.3 Ultrasonic wave velocity and strength tests

Experiments to determine the rock mechanical properties were performed on dry and saturated (i.e., complete, vacuum-saturation of samples with distilled water) samples (Figure 3.7). P wave velocities were measured along the long axis of the cylindrical samples which were later used for the strength tests. The unconfined compressive strength (UCS) experiments (i.e., $\sigma 1 > \sigma 2 = \sigma 3$; $\sigma 2 = \sigma 3 = 0$) as well as the indirect tensile strength (ITS) experiments of this study were performed at the Technische Universität München, on all sample types under a constant strain rate of 3.3×10^{-4} s^{-1} and a constant deformation rate of 0.03 kNs^{-1} respectively. Axial strain and stress were continuously monitored during deformation, by displacement transducers and by a load cell, until failure. Samples for UCS tests were cored with a diameter of 25 mm and with their end-faces ground flat and parallel to a nominal length of 50 mm (length-diameter-ratio of 2:1). For the ITS tests the same sample preparation was applied however the nominal length was shortened to 25 mm ensuring a length-diameter-ratio of 1:1. The load applied to the standing sample disc, perpendicular to the coring orientation was transmitted by a hardwood fiber stripe above and below the sample along the entire sample length.
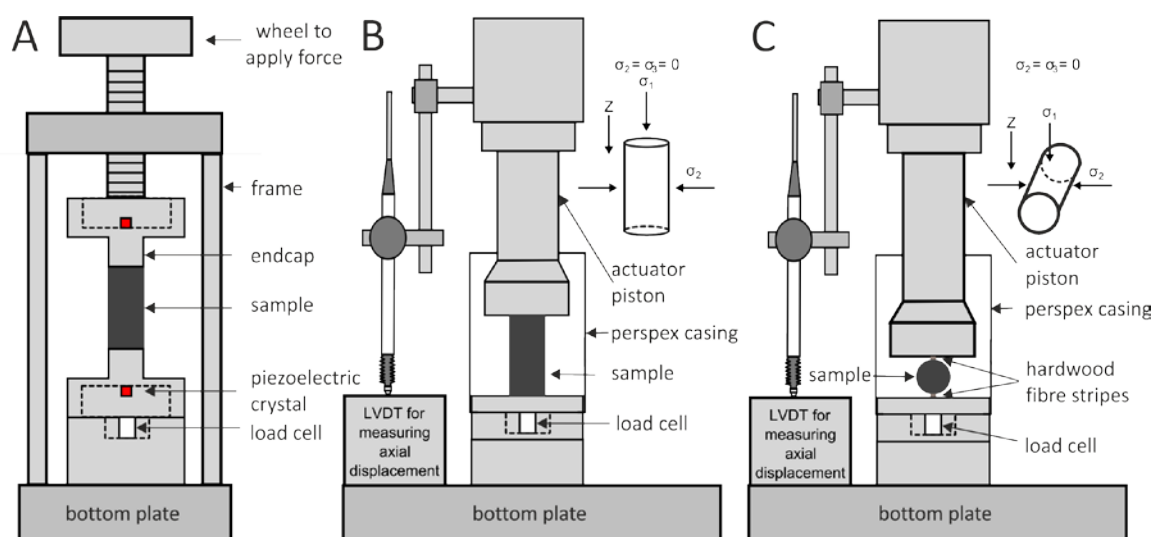
Figure 3.7: Schematic diagram of the experimental arrangement used to determine (A) benchtop elastic wave velocity (Vp), (B) uniaxial compressive strength (UCS), and (C) indirect tensile strength (ITS) (modified after Heap et al., 2014).

3.4.4 Fragmentation experiments

Use of a shock-tube apparatus (Aldibirov and Dingwell, 1996a, b; Martel et al., 2000; Spieler et al., 2003; 2004 Kueppers et al., 2006; Scheu et al., 2006, 2008; Mueller et al., 2005, 2008; Richard et al., 2013; Rager et al., 2013; Mayer et al., 2015) yielded the determination the fragmentation threshold, as well as the fragmentation- and particle ejection-speeds of all samples. The experimental procedures and details are described in Mayer et al. (2015) and references therein. In its present configuration this device permits the accurate control of temperature, gas overpressure and decompression rate in order to best represent variable volcanic and hydrothermal conditions (Mayer et al., 2015). The stainless steel low-pressure tank (l = 3.0 m; d = 0.4 m) at ambient pressure and temperature to collect the experimentally generated pyroclasts, is located above a high-temperature steel autoclave, in which the sample is mounted (Figure 3.8A). First, fragmentation threshold experiments on dry samples at room temperature, determined by rapid decompression of argon gas, were performed on all samples series. A further series of experiments was conducted in order to determine the fragmentation speed, as well as the ejection speed of the gas-particle mixture front in the presence of steam expansion (phreatic experiments) at a target temperature of 260°C and hence a dwell pressure of 4 MPa. These conditions are close to those indicated by gas geoindicators (Chiodini et al., 2011) and also in the range of conditions independently simulated by a physical numerical approach (Todesco et al., 2003) for the single-phase gas zone in the shallow part of the hydrothermal system. Water vapor is the main component of the degassing fluids at Solfatara and Pisciarelli (Caliro et al., 2007).

An additional series of control experiments, in which fragmentation and ejection speed was initiated solely by argon gas expansion (at identical pressure and temperature conditions), was performed. The PVT properties of argon gas are very similar to those of CO_2,

which is the second largest contributor to the fumarolic gases. For the latter experiments, the dry samples were inserted in the autoclave (l = 450 mm; d = 25 mm) and initially pressurized to about 2 MPa before the target temperature of 260°C was reached after a heating time of 45 minutes. The remaining pressurization required for a dwell pressure of 4 MPa was applied during the last stage of heating. These final conditions were maintained for a dwell time of 10 minutes to ensure temperature- and pressure-equilibration over the entire sample before triggering the fragmentation. For the experiments at 'phreatic conditions' the samples were saturated with a calculated amount of distilled water, which led to a pressurization of the system during the vaporization. This enabled to obtain the targeted overpressure solely by the expansion of liquid water to steam within the connected pore space and adjacent volume within the autoclave above the sample (Figure 3.8A) based on the PVT properties of water.
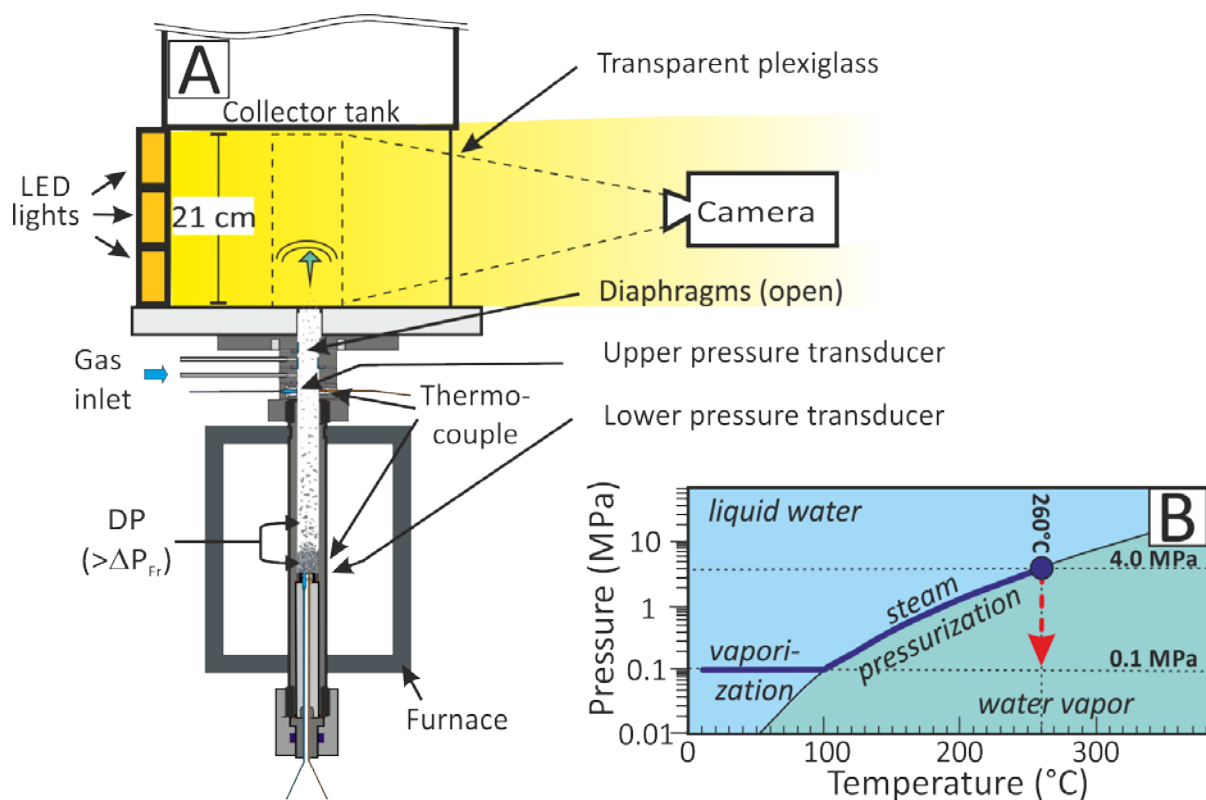
Figure 3.8: Schematic drawing (A) of the experimental setup as well as temperature and pressure condition (B) during the phreatic fragmentation experiments.

Temperature and pressure within the system rose along the boiling curve of water (Figure 3.8B) until targeted dwell conditions of 4 MPa at 260 °C were reached after a heating time of 60 minutes. Before triggering the fragmentation an equilibration time of 10 minutes was occupied. Throughout all experiments, pressure and temperature in the system were monitored at rates of 1000 Hz and 2 Hz, respectively. For this a sensor pair consisting of a dynamic pressure sensor and a thermocouple was located at the bottom of the sample, whereas a second pair sits at the upper end of the autoclave, 225 mm above the sample (Figure 3.8A). The low-pressure tank and the autoclave are separated by a set of two

diaphragms that allow triggering of decompression by a controlled failure of the uppermost diaphragm (Mayer et al., 2015). The decompressing, expanding fluid fragments the sample brittlely in a layer-by-layer fashion (Aldibirov and Dingwell, 2000; Fowler et al., 2010) and the particles are ejected into and stored in the collector tank (Mayer et al., 2015). Evaluation of the travel time of the rarefaction wave from the upper pressure sensor to the top of the sample and analyzing the pressure decay monitored by the dynamic pressure transducers, provided a quantification of the fragmentation speed, according to the procedures developed by Scheu et al. (2006). For each experiment the ejection of the gas-particle mixture was recorded by a high-speed camera (Phantom V710®, Vision Research) at 10.000 frames per second through a transparent plexiglass at an area (h = 21.0 cm, w = 12.5 cm) at the base of the collector tank, just above the diaphragms (Figure 3.8A). The fragmentation setup was equipped with LED lights, facing towards the high-speed camera, in order to facilitate the tracking of very fine particles ejected within the gas-steam-particle mixture. Analysis of the footage by tracking of fragmented particles allowed measurements of their ejection velocities.

3.4.5   Analysis of experimentally generated pyroclasts

In order to investigate the experimentally-generated pyroclasts, all particles of each experiment were collected from the low-pressure tank. Particle size distribution (PSD) analyses of the fragments were carried out by dry-sieving of coarse particles (≥63 µm). Based on PSD data the geometric mean particle size for each sample series was calculated (Folk and Ward, 1957). Laser refraction techniques, using a Coulter LS230 (measuring range 0.375–2000 µm, wave length 750 µm) were applied for the PSD analysis of the fine fraction (<63 µm). Further, the size range and composition of fine particles (<63 µm) from selected samples was investigated by scanning electron microscope equipped with an energy-dispersive system (SEM-EDS) at the LMU using a Bruker AXS DSM 960 A. Additional WD-XRF analysis allowed to quantify the mineralogical composition of the fine fraction (<63 µm), generated during phreatic experiments.

3.5   Results

3.5.1   Mineralogical composition of hydrothermally altered samples

The investigated rocks subjected to intense surficial solfataric alteration consists mainly of i) amorphous silica and ii) alunite. In addition, the Solfatara (S) samples S1 and S2 contain remnants of pristine sanidines. Amorphous silica occurs as pseudomorphs after primary minerals or mineral fragments such as amphibole, pyroxene and feldspar (30–500 µm) indicated by euhedral crystal habits and preserved growth zonations (Figures 3.9A–D) and as silicified accretionary lapilli (100–600 µm) (Figures 3.9E–F).
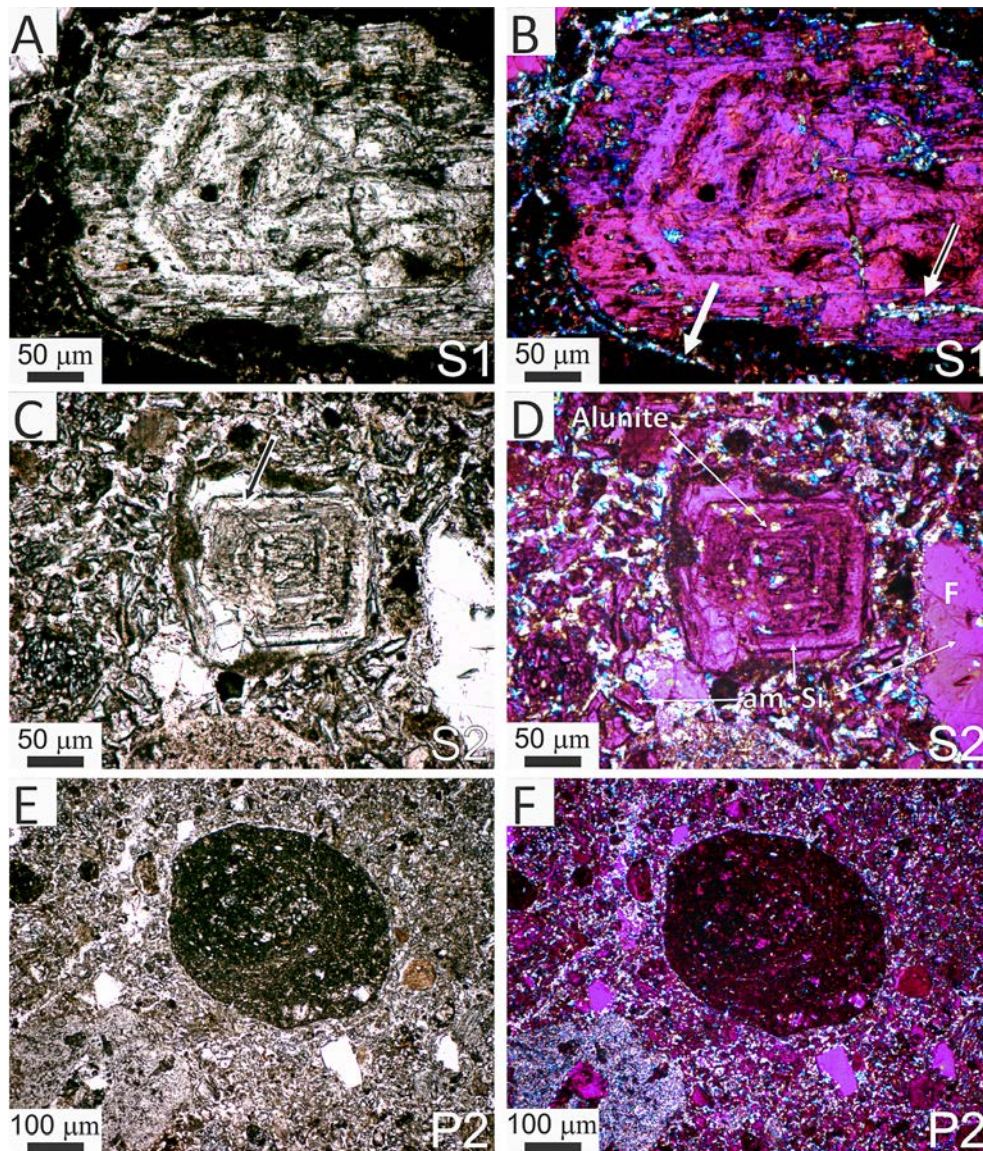
Figure 3.9: Photomicrographs, of investigated samples. (A) Photomicrograph (II pol) of a euhedral crystal with primary growth zonations (most possibly sanidine) marked by fluid inclusions. (B) Photomicrograph (γ+X pol) of the same position as Figure 6A reveals that alunite occurs as fine rims surrounding the pseudomorph (single arrow) and enclosed within the replaced primary mineral (double arrow). (C) Photomicrograph (II pol) of a euhedral crystal with primary growth zonations (most possibly sanidine) and surrounded by a fine-grained matrix. (D) Photomicrograph (γ+X pol) of the same position as Figure 6C reveals that the primary mineral and most of the fine-grained matrix was replaced by amorphous silica. (Note that some alunite crystals are enclosed within the amorphous silica as well as in the fine-grained matrix) Sample S2 contains a higher amount of alunite compared to S1. Amorphous silica fragments (F) are also occurring. (E) Photomicrograph (II pol) of an accretionary lapilli surrounded by a fine-grained matrix consisting of fragments, fluid inclusions and dark granules. (F) Photomicrograph (γ+X pol) of the same position as Figure 6E reveals that most of the accretionary lapilli as well as the surrounding matrix consists of amorphous silica and alunite.

EPMA-EDS analysis reveals that locally core zones of crystals are not yet completely replaced by amorphous silica (Figure 3.10A). XRD whole rock analysis indicates opal-A as the main amorphous silica phase (Figure 3.10B) (Rodgers et al., 2004; Lynne et al., 2005) whereas volcanic glass may also occur, however probably only as minor amount. XRD difractorams of all samples can be found in Appendix B. Alunite (5–10 µm) occurs as i) replacement of matrix (Figures 3.9D, F), ii) alteration rims around silica pseudomorphs, and around silicified accretionary lapilli (Figures 3.9B, F), iii) single crystals enclosed within these pseudomorphs and silicified accretionary lapilli (Figures 3.9D, F) but also along fractures of primary minerals replacing sanidine (Figure 3.10C). XRD and WD-XRF analysis suggest that the alteration affecting the block of samples S1 and S2 led to the formation of amorphous silica and a substantial amount of alunite (increasing from S1 to S2) whereas leaching occurred as the dominant process for S3 resulting in only minor amounts of alunite. Pisciarelli (P) samples showed a more homogenous mineralogy caused by the alteration effects, which resulted in both leaching and alunite formation. WD-XRF analysis supports a slightly higher amount of alunite in P2 compared to P1 and P3. The CIA, based on the WD-XRF analysis (Table 3.1), nevertheless increases from S1 (67.8) to S2 (74.4) and S3 (79.8) and from P1 (73.7) to P2 (75.8) and P3 (77.8) respectively.
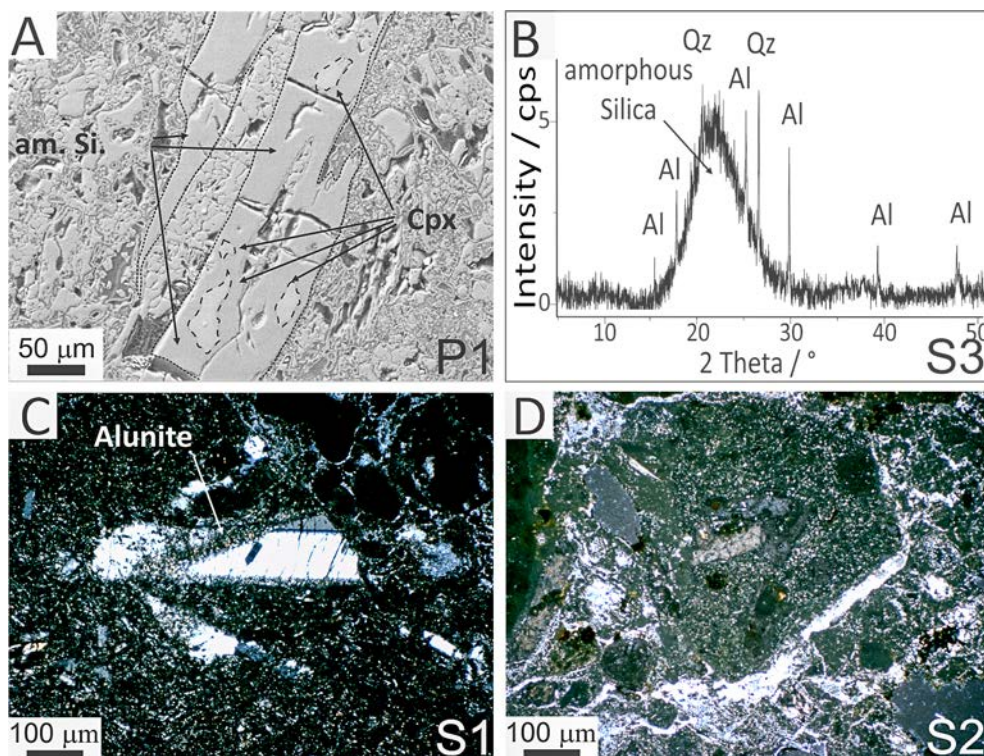
Figure 3.10: BSE image, X-ray diffractogram and photomicrographs of samples. (A) BSE image of a subhedral clinopyroxene (Cpx) crystal almost entirely replaced by amorphous silica (am. Si.). Remnants of Cpx are indicated by dashed lines. (B) Bulk rock X-ray diffractogram showing that the sample S3 consists mainly of amorphous silica, minor alunite (Al) and very minor quartz (Qz). (C) Photomicrograph (X pol) reveals sanidine twinning features and the replacement of sanidine by alunite. (D) Photomicrograph (II pol) of a sub-rounded fragment consisting of mineral fragments in a fine-grained matrix surrounded by a thin rim of alunite.

Table 3.1: Bulk geochemical analysis of investigated samples showing the major element composition and the degree of alteration (CIA).

Sample series	SiO_2 (%)	Al_2O_3 (%)	Fe_2O_3 (%)	MgO (%)	CaO (%)	Na_2O (%)	K_2O (%)	TiO_2 (%)	P_2O_5 (%)	SO_3 (%)	LOI-SO_3 (%)	Sum (%)	CIA
S1	46.5	18.6	2.4	0.1	0.1	0.2	8.5	0.6	0.3	15.5	7.4	100.1	67.8
S2	52.4	12.4	1.5	0.1	0.1	0.1	4.1	0.7	0.2	21.4	7.2	100.2	74.4
S3	88.3	1.8	0.2	0.1	0.1	0.1	0.3	1.1	0.0	3.1	4.6	99.6	79.8
P1	47.0	17.8	0.9	0.1	0.1	0.4	5.9	0.7	0.3	18.6	8.9	100.6	73.7
P2	41.3	19.7	0.2	0.0	0.1	0.3	5.9	0.6	0.2	20.1	12.2	100.7	75.8
P3	52.8	16.2	1.3	0.1	0.1	0.5	4.0	0.6	0.2	18.0	6.5	100.3	77.8

3.5.2   Bulk density, connected porosity and gas permeability

Figure 3.11 illustrates the relation of the CIA and the rock physical properties obtained for dry samples at room temperature. The density decreases with increasing degree of alteration from 2.44 to 2.21 g/cm^3 and from 2.45 to 2.36 g/cm^3 for S and P samples, respectively (Figure 3.11A). By contrast, connected porosity (Figure 3.11B) and gas permeability (Figure 3.11C) increase from 26.6 to 61.3 % and from 4.4 x 10^{-17} to 2.8 x 10^{-14} m^2 for S samples as well as from 34.9 to 48.5 % and 2.2 x 10^{-16} to 1.8 x 10^{-15} m^2 for P samples, respectively (Table 3.2).
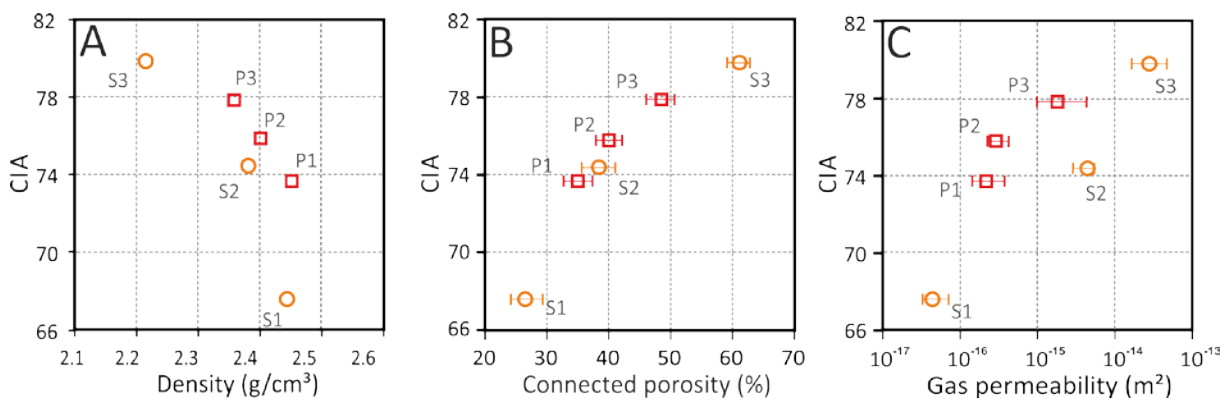
Figure 3.11: Density (A), connected porosity (B) and gas permeability (C) in relation to the CIA of dry samples from Solfatara (circles) and Pisciarelli (squares). (Note: Figure 3.11C displays mean gas permeability values obtained by Tiny PermIII and benchtop lab permeameter, measured in the field and in the lab at the EOST, respectively.)

Table 3.2: Average rock physical properties.

Sample series	Matrix density (g/cm^3)	Bulk density (g/cm^3)	Connected porosity (%)	Gas permeability (m^2)
S1	2.4	1.8	26.6	4.4×10^{-17}
S2	2.4	1.5	38.4	4.5×10^{-15}
S3	2.2	0.9	61.3	2.8×10^{-14}
P1	2.5	1.6	35.0	2.2×10^{-16}
P2	2.4	1.5	40.0	2.9×10^{-16}
P3	2.4	1.3	48.5	1.8×10^{-15}

3.5.3 Elastic wave velocity, UCS and ITS

The relationship between rock mechanical properties and the connected porosity is shown in Figure 3.12 and summarized in Table 3.3. P-wave velocities of dry and water saturated samples decrease with increasing connected porosity from 2.5 to 0.6 km/s and 4.0 to 0.8 km/s (Figure 3.12A). As a further consequence, the UCS (Figure 3.12B) as well as the ITS (Figure 3.12C) of dry samples decreases from 34.8 to 5.5 MPa and from 4.4 to 0.6 MPa. Water-saturated samples exhibit both lower UCS and ITS values ranging between 33.5–4.0 MPa and between 3.7–0.5 MPa, respectively.
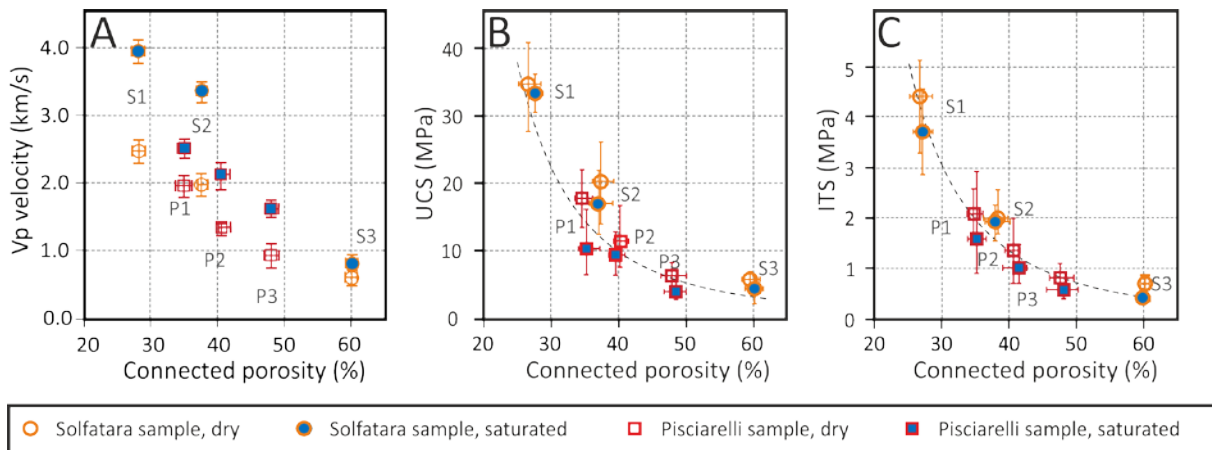
Figure 3.12: Ultrasonic P wave velocity (A), UCS (B) and ITS (C) as a function of the connected porosity of studied samples from Solfatara (circles) and Pisciarelli (squares). Generally the displayed rock mechanical properties decrease with increasing porosity.

3.5.4 Fragmentation threshold, speed and ejection speed

Experiments to determine the fragmentation threshold have been repeated three times in order to account for sample heterogeneities. Investigated samples fully fragment during decompression at initial pressures ranging from 4.2–2.0 MPa (Figure 3.13; Table 3.4). The results follow the trend defined in previous studies (e.g. Mayer et al., 2015, and references therein) and plot slightly below the fragmentation criterion of Koyaguchi et al. (2008) derived from experiments with pristine volcanic rocks.
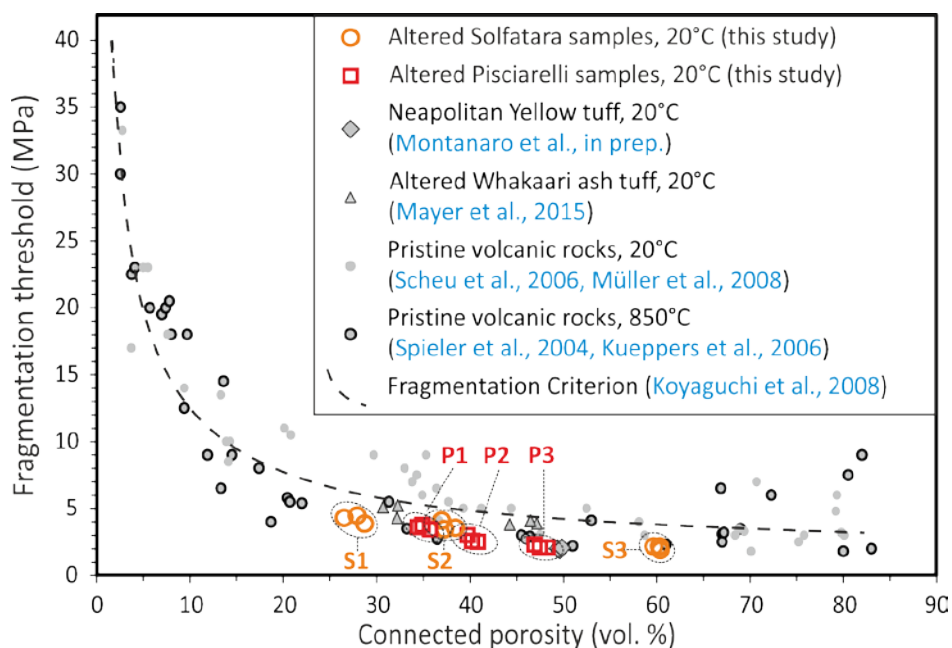
Figure 3.13: Fragmentation threshold of investigated samples at 20 °C during rapid decompression experiments. Fragmentation threshold for several rocks obtained in other studies are also compiled. The dashed line corresponds to the fragmentation criterion proposed by Koyaguchi et al. (2008). Samples with a higher porosity fragment at a lower initial pore pressure. Altered samples of this study confirm the criterion plotting slightly below the dashed lines.

Table 3.3:Averaged rock porosities and mechanical properties.

Sample series	Connected porosity (mean) (%)	Vp dry (mean) (km/s)	Vp saturated (mean) (km/s)	UCS dry (mean) (MPa)	UCS saturated (mean) (MPa)	ITS dry (mean) (MPa)	ITS saturated (mean) (MPa)
S1	26.6	2.5	4.0	34.8	33.5	4.4	3.7
S2	38.4	2.0	3.4	20.3	16.8	2.0	2.0
S3	61.3	0.6	0.8	5.5	4.5	0.7	0.5
P1	35.0	1.9	2.5	17.0	10.2	2.1	1.6
P2	40.0	1.4	2.1	11.3	9.7	1.4	1.0
P3	48.5	0.9	1.6	6.3	4.0	0.6	0.6

Fragmentation and ejection speed of particles front in the presence of dry argon gas and stream expansion at 260 °C and at an initial pressure of 4 MPa are summarized in Table 3.4 and displayed in Figure 3.14. Both values were obtained in a single experiment that was again repeated three times to account for sample heterogeneities. The fragmentation velocities (Figure 3.14A) obtained in the phreatic experiments generally rise with increasing porosity and range between 15.2–45.0 m/s (S) as well as between 26.2 – 34.9 m/s (P). Fragmentation speeds resulting from pure argon gas expansion (control experiments) follow a similar trend but exhibit lower speeds ranging between 10.6–34.9 m/s (S) and 16.4–27.2 m/s (P). The ejection speed of the particle front obtained by high-speed video analysis reveals a similar dependence (Figure 3.14B). Particle ejection velocities in the presence of steam expansion (phreatic experiments) ranging from 74.5–174.3 m/s (S) and 111.0–139.1 m/s (P) are higher than those attained in the control experiments, extending from 52.9–158.9 m/s (S) and 91.4–121.8 m/s (P).
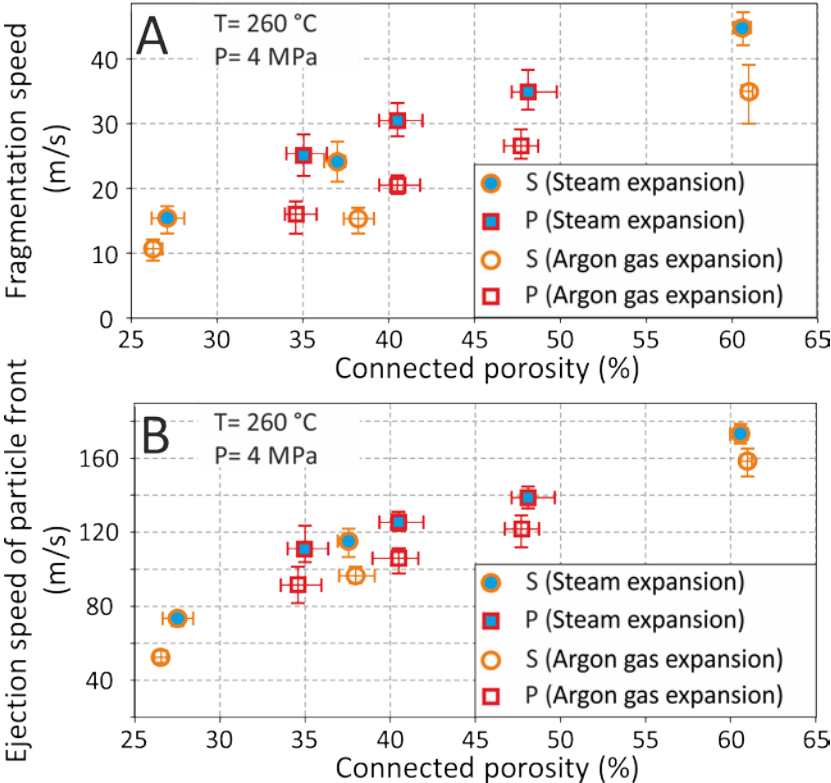
Figure 3.14: Fragmentation and ejection speed of particle front obtained by rapid decompression experiments at 260 °C and 4 MPa initial pressure. (A) Fragmentation speeds within sample series (S, P), increase with porosity and in the presence of steam expansion. (B) Ejection speed of the particle front in the presence of argon gas and steam expansion. The ejection speed values correspond to the average of the velocities of several particles (≥5) traveling at the front of the gas-particle mixture. The velocity of ejected particles increases with porosity and in the presence of steam expansion. (Note: Plotted values represent the average of three experiments; error bars indicate the range of porosity and of obtained speeds).

Table 3.4: Averaged values from results obtained in fragmentation experiments.

Sample series	Connected porosity (mean)	Frag. threshold (mean)	Frag. speed Steam exp. (mean)	Frag. speed Argon gas exp.	Eject. speed Steam exp. (mean)	Eject. speed Argon gas exp.
	(%)	(MPa)	(m/s)	(m/s)	(m/s)	(m/s)
S1	26.6	4.2	15.2	10.6	74.5	52.9
S2	38.4	3.7	24.1	15.3	115.8	96.3
S3	61.3	2.0	45.0	34.9	174.3	158.9
P1	35.0	3.7	26.2	16.4	111.0	91.4
P2	40.0	2.7	30.6	24.4	123.2	104.2
P3	48.5	2.2	34.9	27.2	139.1	121.8

3.5.5 Size and compositional analysis of fragments

Particles generated during fragmentation have been recollected and the PSD of the coarse (≥63 μm) and fine (<63 μm) fraction was determined. Figure 3.15 shows the cumulative curve of the weight fractions for phreatic (Figure 3.15A, B) and control experiments (Figure 3.15C, D), in which every individual line represents the entirety of particles collected from three experiments. The geometric mean particle size (Folk and Ward, 1957) of S fragments decreases in the phreatic experiments from S1 (2412 μm) to S2 (2217 μm) and S3 (1696 μm) and is smaller than the mean particle size generated in the control experiments, which decrease from S1 (3948 μm) to S2 (2985 μm) and S3 (2301 μm).
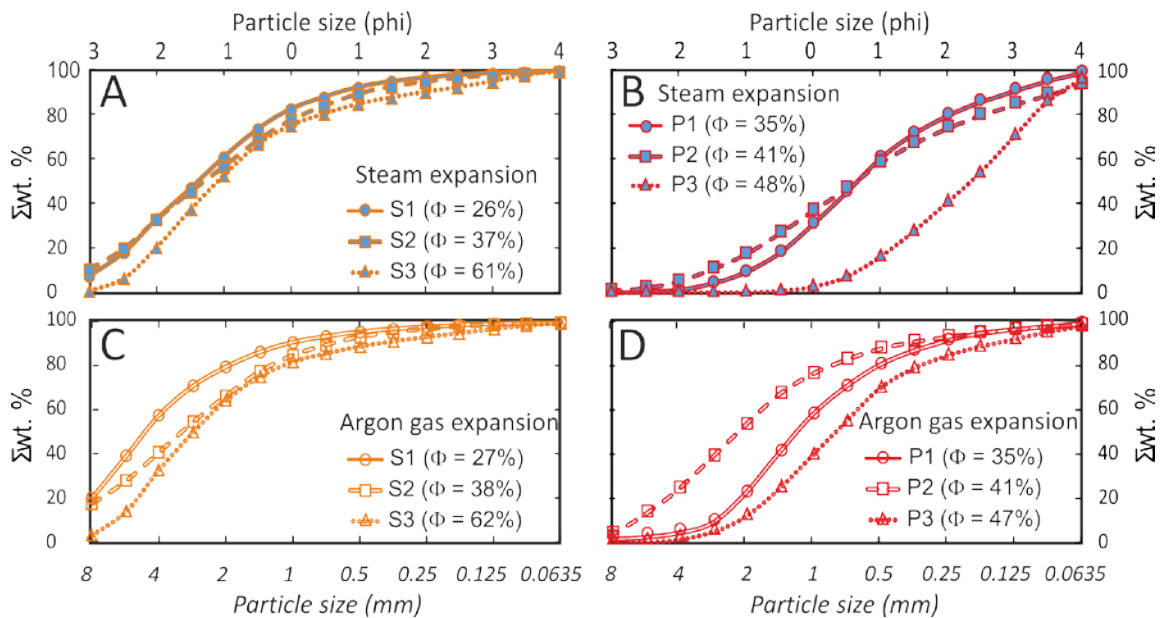
Figure 3.15: Cumulative particle size distribution (PSD) plots showing the weight fractions of particles after rapid decompression experiments. (A, B) Fragmentation of Solfatara and Pisciarelli samples due to steam expansion (phreatic experiments) and in the presence of argon gas expansion (C, D). The particle size is decreasing to the right in all plots, showing a particle-size reduction with increasing porosity for the phreatic experiments and for the control experiment with Solfatara samples. PSD obtained in control experiments with Pisciarelli sample revealed a different trend with intermediate porous sample S2 showing the coarsest PSD.

PSD of P samples after the phreatic experiments shows P1 containing a higher amount of fines and smaller amount of coarse particles when compared to P2. The mean particle diameter of P1 (564 µm) is slightly higher than P2 (550 µm). P3 differs significantly with a mean particle diameter of 208 µm and a PSD shifted towards a high amount of fines. The size analysis of P samples after the control experiments shows bigger mean particle sizes than in the phreatic experiments, but a PSD and mean particle size decreasing from P2 (1891 µm) to P1 (1027 µm) and P3 (703 µm). Figure 3.16A displays the proportion (in wt. %) of fine particles (<63 µm) in the control experiments in comparison to those generated in the phreatic experiments. Results show only minor amounts (0.3–0.5 %) of fines for S samples in control experiments and slightly increased amounts (0.5–0.9 %) in the phreatic experiments. In contrast P samples fragmented during argon gas expansion produced 1.1–2.3 % of fines, whereas steam expansion led to an increased amount 2.1–7.4 %. The amount of fine material generated in fragmentation experiments on P samples was sufficient for quantitative chemical analysis. Figure 3.16B shows a decreasing proportion of amorphous silica from the bulk sample to that containing in the fine fraction of control and phreatic experiments for all P sample series. XRF analysis revealed a minimum amorphous silica content in the bulk sample of 41 % and a maximum reduction of 8 % for P2.
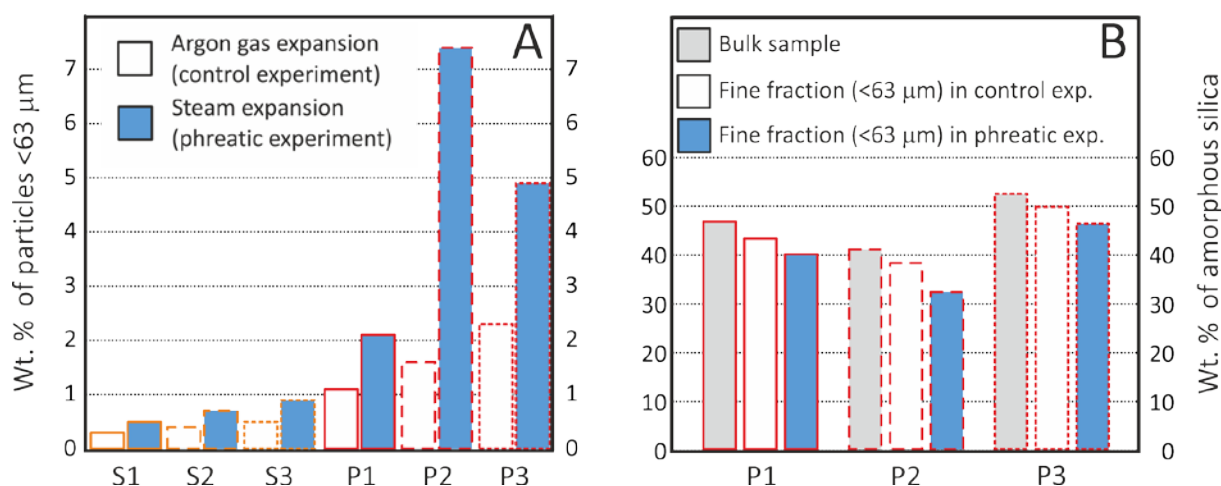
Figure 3.16: (A) Proportion of fine particles (<63 µm) generated in control and phreatic experiments in wt. %. Generation of fines increases with increasing porosity and degree of alteration in control experiments for both P and S samples. In phreatic experiments the proportion of fines also generally increases with porosity and is higher than in control experiments. Results revealed a significant increase of fines in phreatic experiments with P samples. (B) Amount of amorphous silica in bulk sample and fine fraction generated in control and phreatic experiments with P samples. A clear decrease in the amount of amorphous silica is shown related to an enrichment of alunite in the fine fraction. P2 contains the smallest amount of amorphous silica and as a consequence highest amount of alunite within the fraction of particles <63 µm.

Additional insight in the size and compositional characteristics of the fine fraction is gained by SEM-EDS and PSD analysis via laser refraction technique (Figure 3.17). The amount of alunite (partially precipitated on amorphous silica clasts) increases from S1 to S2 and P1 to P2, respectively. Alunite crystal sizes in the fine fraction range between few microns

whereas amorphous silica clasts show diameters up to 100 microns. The particles generated during the fragmentation experiments are mainly agglomerates of both phases and more or less individual alunite crystals. Alunite, identified by euhedral crystal shape and SEM-EDS analysis clearly dominates the fraction of very fines (<10 μm). The cumulative PSD plots (Figure 3.17A) show the weight proportion of fines on the total amount of particles. S1 and S2 contain a higher amount of very fines compared to S3 whereas P samples show a gradual trend towards more very fines from P1 to P3 and P2. SEM images of P1, P2 and S2 samples are characterized by amorphous silica particles with different amount of alunite crystal growth on the surface (Figure 3.17B). In contrast S3 shows only minor amounts of alunite, but instead typical ˈvuggy silicaˈ features of the particles.
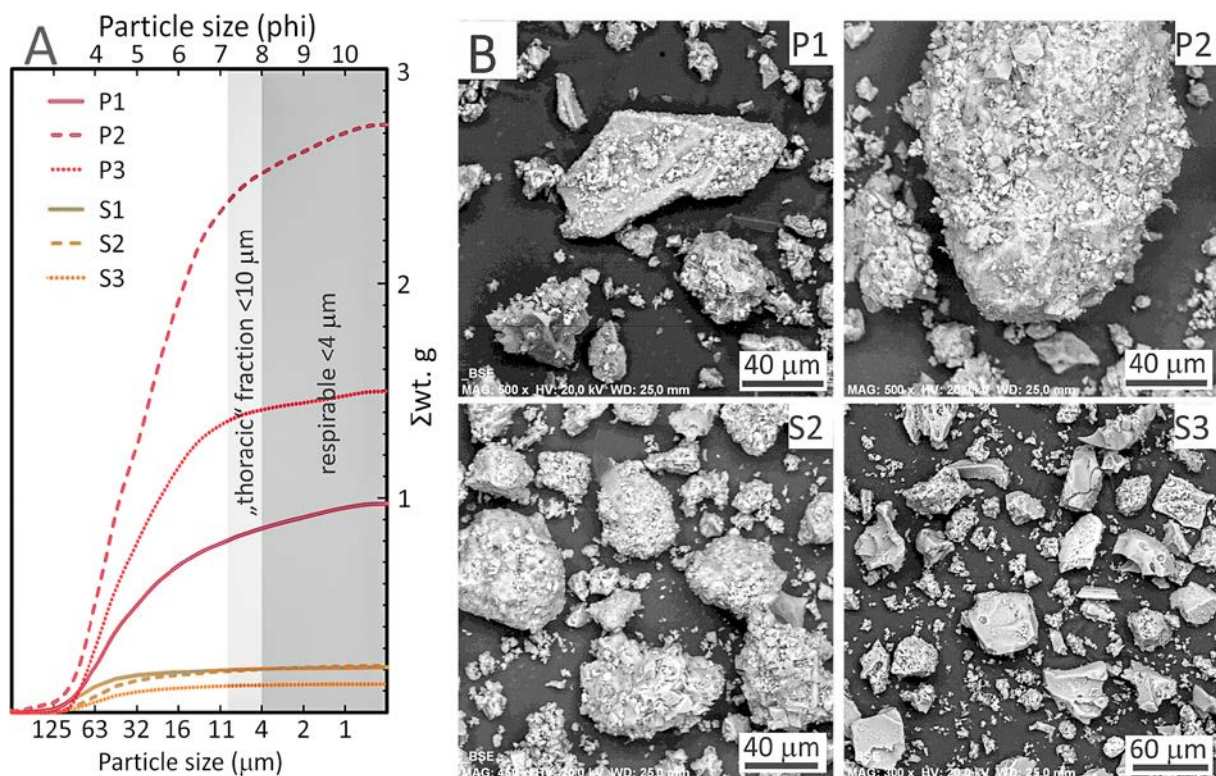
Figure 3.17: (A) Cumulative PSD plots showing the amount of fine particles (<63 μm; separated by dry sieving) generated during phreatic experiments on samples with an initial volume of 29.4 cm³. P samples produce a significant higher amount of very fines, attributing to the ˈthoracicˈ (<10 μm) and respirable (<4 μm) fraction, than S samples. S3 containing the lowest proportion of alunite, produced the lowest amount of very fines. (B) SEM images of selected S and P particles showing small euhedral alunite crystals on large grains and fragments replaced by amorphous silica. Chemical composition of individual particles was measured by SEM-EDX analysis. SEM images reveal different amount of alunite on amorphous silica surface. S3 particles show porous ˈvuggy silicaˈ alteration features on particles surface and only a minor amount of euhedral alunite crystals.

3.6 Discussion

According to the above, surficial solfataric alteration has significant effects on the mineralogy of rocks and led to a degradation of their physical properties - a trend confirmed by an increasing CIA. The increase in porosity due to acidic leaching in combination with the replacement of pristine mineralogy by alunite has a first order control on the mechanical properties, on the fragmentation behavior of investigated rock samples and on the production of fines during fragmentation initiated in rapid decompression experiments.

3.6.1 Geochemical, rock physical and mechanical properties

The mineralogy determined in this study derives from a complex interaction of alunite and amorphous silica formation. It is most likely generated by the repetition of alteration processes with spatial and temporal variability depending on temperature, pH and fluid composition (Zimbelman et al., 2005). A dominant process can hardly be identified as alunite is enclosed in amorphous silica and vice versa. Acidic leaching of the rocks caused the decrease and almost entire removal of mobile elements (Ca, Na, Mg) and led to relatively high amounts of residual silica. However, the formation of alunite has prevented the removal of aluminum and potassium (Table 3.1). The CIA values obtained for the investigated rocks confirm the alteration trend found by geochemical analysis including optical microscopy and also correlate well with those determined by Pola et al. (2012) for altered pyroclastic rocks. The mineralogy of surficial encrustations and efflorescences on rocks from Solfatara and Pisciarelli determined by Piochi et al. (2015) differ from the results of this study. Within the internal rock structure, leaching and thus formation of amorphous silica is one of the main processes. This appears not to be evident at the rock surface. The formation of native sulfur and other sulfates (e.g. alunogen, pickingerite, potassium alum; Piochi et al., 2015) seems to occur solely on the rock surfaces. Fulignati et al. (1998) suggested supergene origin of sulfates (e.g. gypsum) due to the circulation of surface rainwater fluids in their study investigating hydrothermal alteration at Vulcano (Aeolian Islands, Italy). Although these two studies did not focus on effects of alteration on rock physical properties, their results nevertheless highlight the high variability in alteration minerals on a small scale. The alteration processes observed in this study causes a general decrease in sample density, an increase in connected porosity and as a consequence a higher gas permeability of the investigated rocks. Hence these effects lead to lower elastic wave velocities as well as lower uniaxial compressive and indirect tensile strengths (Figure 3.12). The obtained results are in agreement with the mechanical properties of altered pyroclastic rocks investigated by Pola et al. (2013). The samples mainly consist of silicified components within a matrix replaced by abundant alunite crystals with sizes of few microns in sizes (Figure 3.9-3.10). This hydrolytic alteration causing the dissolution of silicate minerals leads to a decrease in bulk rock density by removal of cations and silica in solution, destroying the primary rock fabric (Vikre and Henry, 2011).

Density reduction and alteration in combination with the development of the resulting fine-grained microstructure imparts weak bonding forces to the rock, exhibited by low values of P wave velocity, tensile and compressive strength. Water saturation of samples increases the ultrasonic wave velocities (as P wave velocity is higher in water than in air) (Heap et al., 2014) and additionally decreases the strength values due the weakening effect of water (Baud et al., 2000). Our results therefore confirm the findings of previous studies on different hydrothermally altered volcanic rocks (Arıkan et al., 2007; Del Potro and Hürlimann, 2009; Pola et al., 2012).

3.6.2 Fragmentation behavior

The fragmentation threshold of investigated samples decreases with increasing degree of alteration as a consequence of the increased porosity. Alteration and the fine-grained microstructure cause a weaker cementation of samples when compared to unaltered tuffs (e.g. NYT, Montanaro et al., in prep). This leads to fragmentation below the threshold defined by Koyaguchi et al. (2008). These results are in agreement with the fragmentation threshold of hydrothermally-altered ash tuffs (Mayer et al., 2015), which also plot slightly below the fragmentation criterion (Figure 3.13). Rock physical and mechanical properties as well as the initial overpressure and the type of fluid within the pores have a first order control on the fragmentation and ejection speed of the sample (Mayer et al., 2015, and references therein). The analysis of fragmentation experiments reveals that fragmentation and ejection speed generally increase with increasing porosity. The amount of pressurized fluid stored within the sample and causing the fragmentation and ejection of particles during rapid decompression is controlled by the connected porosity (Scheu et al., 2006; Mayer et al., 2015). Further, steam expansion leads to slightly higher fragmentation and ejection speed than expansion of argon gas. This highlights the influence of the fluid type and especially the expansion coefficient on the processes. Water vapor at 4 MPa and 260 °C has a 1.2-fold larger volume increase during the isothermal expansion to ambient pressure compared with pure argon gas expansion. As a result, the fragmentation and ejection speeds are somewhat higher in the phreatic experiments as the processes involved are more energetic (Wohletz, 1983). Our results are in agreement with previous studies determining the fragmentation speed of pristine samples at an initial argon gas overpressure of 4 MPa (Spieler et al., 2004; Richard et al., 2013). In those studies, samples with a connected porosity of 48.0 % and 59.8 % fragmented at 14 and 22 m/s, respectively, lower than the fragmentation speeds of heavily altered samples of this study with similar porosities (P3, S3). This indicates a weaker strength of altered samples resulting in a faster fragmentation when compared to unaltered samples.

Under constant initial conditions, the ejection velocity of the gas-particle mixture increases with increasing porosity but also with increasing fragmentation velocity. In addition, the ejection speed is higher than the fragmentation velocity. These results confirm the findings of previous studies (Alatorre-Ibargüengoitia et al., 2011; Mayer et al., 2015). As

the alteration lowers the strength of the rock, a lower amount of energy is consumed by fragmentation and, as a consequence, more energy is available for acceleration and ejection of the fragments – resulting in a higher ejection speed.

Further, the degree of alteration showed an influence on the particle size distribution of experimentally generated pyroclasts – this effect is mainly due to the increase in porosity. Samples with higher porosities contain a higher gas volume resulting in higher fragmentation energy (Kueppers et al., 2006). Therefore, our results indicate that the fragmentation of altered samples generally leads to a decreased mean fragment diameter and produces an increased amount of fine particles. Such high proportions of fine (<10 μm) and very fine (<4 μm) particles, which lie in the 'thoracic' and respirable fraction, constitute a severe hazard due to the potential for causing acute and chronic respiratory diseases (Horwell and Baxter, 2006; Horwell, 2007). PSD analysis further revealed however that the production of fines is not only controlled by porosity. The samples investigated exhibit different productions of fines depending on the type of fluid (steam vs. argon gas) causing the fragmentation. The complex microstructure (distribution of alunite within the sample, size of amorphous silica particles) of these heavily altered, fine-grained surge deposits seems to have a control on the fragmentation process. The phreatic experiments with P samples in particular generated abundant fines (Figure 3.16A). WD-XRF analysis revealed that the fraction <63 μm experienced a decrease in silica (Figure 3.16B) resulting in an increased amount of alunite. These findings are in good agreement with the PSD (<63 μm) obtained by laser refraction analysis and with SEM-EDS analysis. Smallest particles generally characterized by a rhombohedral morphology are predominantly alunites. They appear as small clusters precipitated on the surface of amorphous silica clasts (Figure 3.17B). Very few amorphous silica particles of P samples contain surfaces that are 'alunite-free' consistent with the proposal that fragmentation within the samples initiates at the contact between alunites. A higher fraction of alunite and a more homogeneous distribution amongst the amorphous silica particles would thereby favor a higher fraction of finer fragments. In particular, the interaction of steam and a homogenous alunite distribution appears to enhance very efficient fragmentation.

3.7 Summary and conclusions

The effects of surficial solfataric alteration on mineralogy, rock physical and mechanical properties and as a consequence on the fragmentation and ejection behavior of samples from the hydrothermally active sites of Solfatara and Pisciarelli have been investigated. The PSD and composition of selected fine-grained pyroclastic fractions was also analyzed. Rapid decompression experiments were designed to compare phreatic conditions (steam expansion) with dry argon gas expansion at initial conditions of 260 °C and 4 MPa in order to evaluate the influence of different fluids. For quantification of sample's degree of

alteration a chemical index (CIA) was applied and compared to the experimentally obtained properties. The main observations and conclusions are:

(1) Alteration by sulfuric acid causes leaching of the rocks and thereby the formation of amorphous silica (mainly opal-A) as well as the formation of alunite as a replacement of crystals and groundmass;

(2) The investigated rocks do not contain any clay minerals due to the high acidity of the fluids involved;

(3) The alteration weakens the rocks, increases porosity and permeability and leads to a lower fragmentation threshold;

(4) Fragmentation and ejection speed of samples increase with increasing porosity and with a higher degree of alteration respectively. Both velocities are slightly enhanced in the presence of steam expansion;

(5) The microstructure of the samples has an influence on the rock mechanical properties, on the fragmentation behavior and on the production of fine particles;

(6) Fragmentation of fine-grained ash fall deposits (P samples) affected by solfataric alteration produces a significant amount of fines containing a considerable proportion of very fines (<10 μm);

(7) Due to their potential to instigate chronic diseases, dispersion of such material would represent a serious health hazard on a local scale.

In summary our results have shown that solfataric alteration in the upper regions of hydrothermal systems is increasing the permeability of surficial rocks. A conceptual model for the formation of near surface high-sulfidation alteration is illustrated in Figure 3.18. Depending on pH, fluid temperature and composition, a sequence of different zones develops with increasing distance to the main fumarolic conduits. The most acidic core is characterized by a halo of amorphous silica, the residual phase after the mobilization of all other elements. The depletion in Al_2O_3 within this silicic alteration zone is significant for conditions with pH <2 (Stoffregen, 1987). Laterally the progressive neutralization of fluids by reaction with the rocks, generates a domain with pH >2. This in turn results in much less depletion due to the immobility of aluminum and thereby the formation of alunite (Fulignati et al., 1998). A further neutralization of the fluids favors the formation of kaolinite at lower acidity (4 < pH < 6) in an intermediate argillic alteration regime (Boyce et al., 2007). Rock permeability as well as the degree of alteration increases towards the center of the hydrothermal activity, in agreement with the study by Piochi et al. (2015). As a consequence, this should reduce the risk of pressurization within the shallow subsurface. Alteration at greater depth (Mormone et al., 2014) and its effect on the permeability by argillic alteration

and by vein and pore filling precipitation might be a process of higher importance concerning volcanic unrest. But still the risk of surficial phreatic events can't be excluded. Pressurization can also be caused by an increased fluid supply deriving from the hydrothermal system, which could in turn exceed the outgassing capacities and result in a phreatic eruption.

Our study investigated the processes of such an event and highlights the effects on the rocks present at the main hydrothermal sites of Campi Flegrei. Further, rocks dominated by secondary precipitated alunite and amorphous silica produce an increased fraction of very fine particles during fragmentation. Ash particles in this size range and especially those possessing silica- and alumina-rich compositions constitute a high potential for respiratory diseases and their dispersion would represent a serious health hazard on a local scale. The mineralogy of host rocks should therefore be considered for modelling of eruptions in hydrothermally active sites and taken into account for hazard assessment.
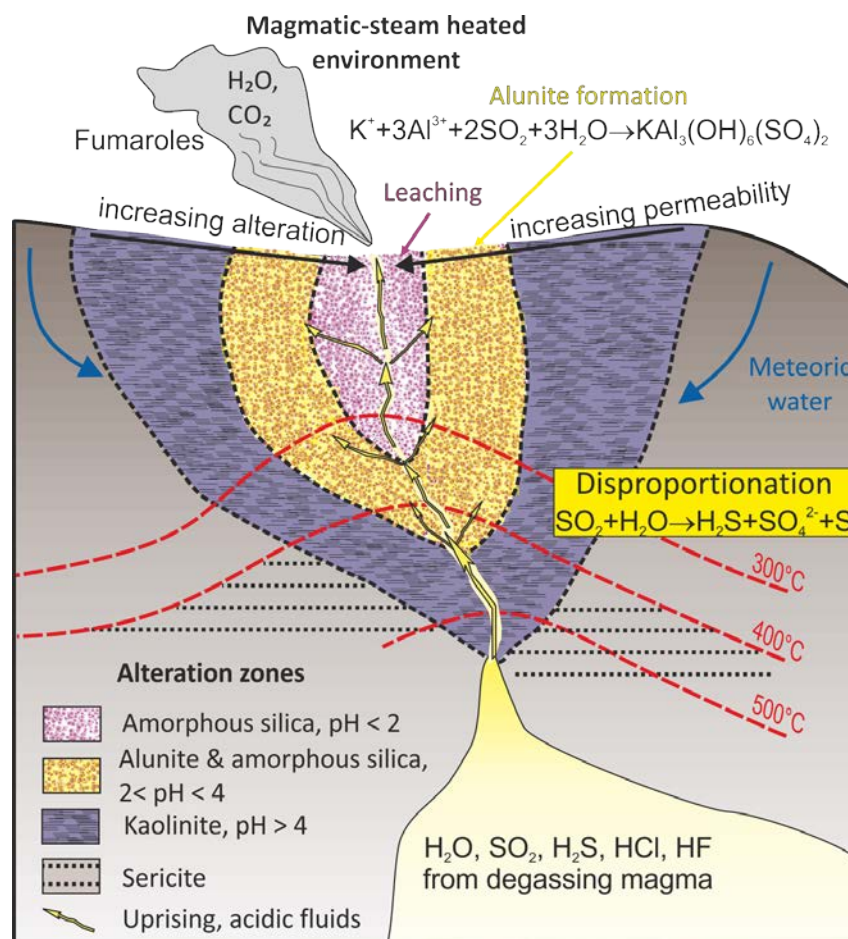
Figure 3.18: Conceptual model for the formation of near surface high-sulfidation alteration (modified after Robb et al., 2005). pH, fluid temperature and composition control the development of alteration zones with increasing distance to the main fumarolic conduit. A highly permeable, acidic core characterized by amorphous silica is laterally replaced by a zone of alunite and amorphous silica. Successive neutralization of the fluids promotes the formation of kaolinite. Rock permeability as well as the degree of alteration increase towards the center of the hydrothermal activity.

4 Phreatic activity and hydrothermal alteration in the Valley of Desolation, Dominica

Figure 4.1: Steaming vents in the Valley of Desolation, Dominica (Lesser Antilles).

This page was intentionally left blank.

4.1 Introduction

Dominica has one of the worldwide highest concentrations of potentially active volcanoes, which are related to nine distinct volcanic centers on the island (Lindsay et al., 2003). In addition to this activity, abundant geothermal phenomena are observed at the surface, especially in the southern part of the Island. The Valley of Desolation/Boiling Lake area is one of the most vigorous ones, hosting hot springs, mud pools, fumaroles, steam vents and the second largest boiling lake in the world (Di Napoli et al., 2014). These very touristic sites, formed as a result of phreatic and/or phreatomagmatic eruptions, are textbook examples for past and present phreatic activities on various scales. Based on the Volcanic Hazard Atlas of the Lesser Antilles (Lindsay et al., 2005), a phreatic eruption from one of these sites is considered as the most likely scenario for future volcanic activity on Dominica. The hazards associated with such non-juvenile eruptions are the explosion and ejection of fluids with significant quantities of mud and rocks (Montanaro et al., 2016).

Only little information is available on the Valley of Desolation, in particular its hydrothermal activity, (Herlihy, et al., 2005; Smith et al., 2013) historic phreatic events (Nicholls, 1880; Watt, 1880; Nicholls and Watt, 1880; Sapper, 1903; James, 1997; Komorowski and Hammouya, 1998; Lindsay et al., 2005) or surficial alteration processes. Past studies focused indeed on the geology of the island and described some details in the framework of volcanic hazard assessment (Lindsay et al., 2005). Joseph et al. (2011) investigated the geochemistry of the main geothermal areas, including the Valley of Desolation. Further studies have been conducted on the Boiling Lake (Fournier et al., 2009; Di Napoli et al., 2013), one of Dominica's most popular tourist attractions, which was showing episodic drainage events in the past.

Despite the abundance of surficial hydrothermal phenomena within the Valley of Desolation (Joseph et al., 2011), no detailed descriptions or maps do exist. Phreatic eruptions have occurred in historic times (1863, 1880, 1997), but little estimates on the processes leading to them, have been suggested. Hydrothermal alteration of the host rock or of the ejecta generated by the abovementioned historic eruptions, is scarcely described (Lindsay et al., 2005, and references therein; James, 1997). Soil properties affected by weathering processes across the island have been investigated (Rouse et al., 1986; Rao, 1996). Yet, a detailed description of both supergene and hydrothermal alteration within the Valley of Desolation, and their influence on outgassing is still lacking.

Here, results from two field campaigns including mapping, in situ measurements and sampling of weathered and hydrothermally altered rocks from the Valley of Desolation are presented. Furthermore laboratory investigations on rock samples were carried out. In particular, the effects of hydrothermal alteration on rock composition as well as on rock physical and mechanical properties (including in situ permeability), have been studied.

Additionally, rapid decompression experiments allowed to investigate the ejection behavior of hydrothermally altered, unconsolidated material collected from the vicinity of the last phreatic eruption (1997).

4.2 Geological setting

The Valley of Desolation is situated within the Morne Trois Piton National Park in the south-central part of Dominica (Lesser Antilles) (Figure 4.2A). The island of Dominica, with an area of 750 km^2 and a rugged topography, consists almost entirely of volcanic rocks and their weathering products, which are mostly covered by dense vegetation (Lindsay et al., 2005). The oldest rocks of the relatively young island have been dated to Miocene times (7 Ma; Demange et al., 1985). About 1.6 Ma ago, volcanic activity migrated from the northern to the southern half of the island. Based on seismic activity, Morne Diablotin and Morne aux Diables (located in the North) show still a potential activity (Joseph et al., 2011).
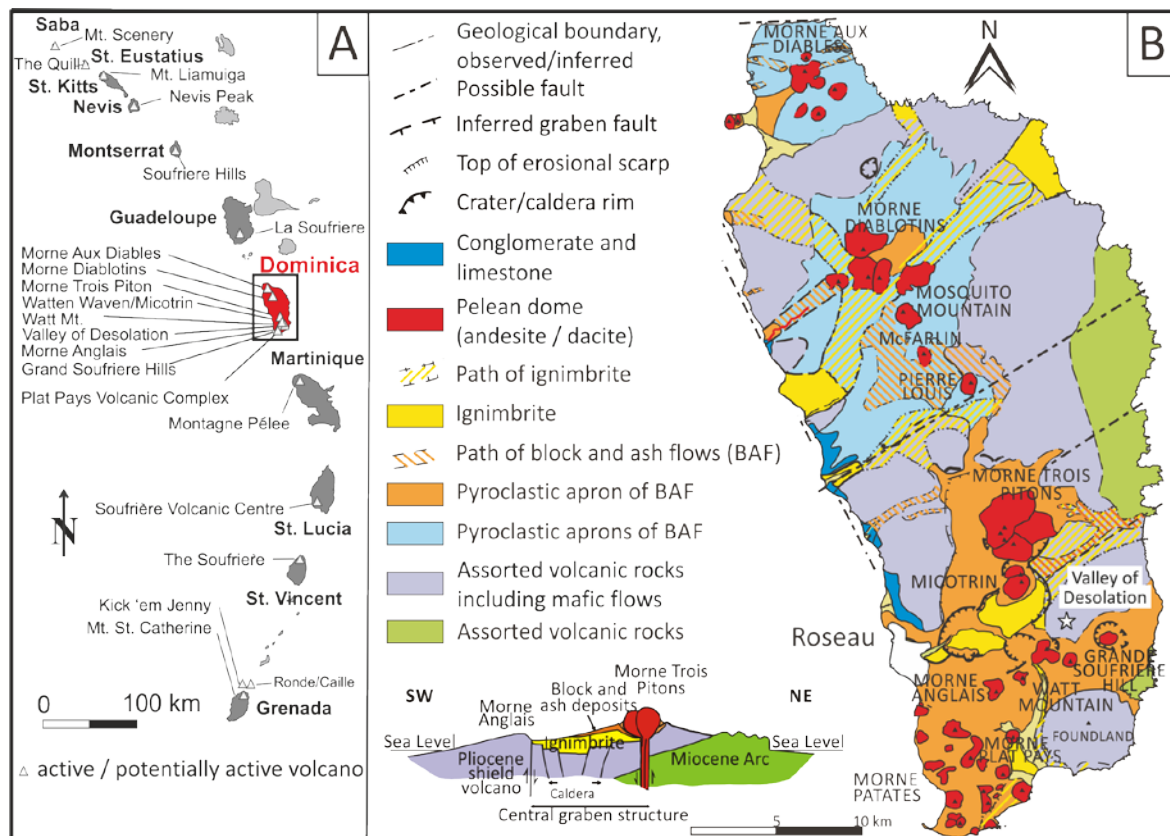
Figure 4.2: (A) Simplified geographical map of the Lesser Antilles showing the location of Dominica (modified after Joseph et al., 2011). (B) Simplified geological map of Dominica (modified from Roobol and Smith, 2005).

Since the late Pleistocene seven major andesitic-dacitic volcanic centers, most of them associated with a geothermal systems, have been active in the South of Dominica (Lindsay et al., 2003). Most of them erupted within the last 10 ka (Lindsay et al., 2005; Joseph et al., 2011). Regarding the erupted volume of magma within the last 100 ka, Dominica was

with ~40 km^3 the most productive of all volcanic islands in the Lesser Antilles (Wadge, 1984; Di Napoli et al., 2013). The mainly andesitic-dacitic lithology of Dominica comprises Pelean domes and ignimbrites as well as block and ash flows and assorted volcanic rocks (Lindsay et al., 2005; Robool and Smith, 2005) (Figure 4.2B). Due to the tropical climate with a high mean rainfall (3000 mm) and the distinct topography (slopes frequently exceeding 40°), the island is subject to extreme weathering and physical denudation, mainly controlled by landslides (Rouse et al., 1986; Rad et al., 2013). Weathering favors the formation of montmorillonite-rich smectoid soils, which demonstrate an early stage within the soil formation, generally characterized by extremely high porosity and permeability (Rouse et al., 1986). The Valley of Desolation itself is located within massive lavas associated with the Pelean dome of Watt mountain (Traineau et al., 2015). Block and ash flow deposits as well as landslide debris deriving from the surrounding slopes partially filled the valley, which was formed by phreatic or phreatomagmatic eruptions (Lindsay et al., 2005).

Nowadays the Valley of Desolation/Boiling Lake area is, one of the main geothermally active areas throughout the island (Joseph et al., 2011). Its geothermal origin is still unclear. According to Traineau et al. (2015), the circular shaped depression containing the Valley of Desolation/Boiling Lake area might be related to a local fault system trending NE–SW and NNW–SSE. (Figure 4.3) Nevertheless the Valley of Desolation/Boiling Lake area comprises several small, crater-shaped depressions associated with vigorous hydrothermal activity. The dilution of acidic gases in near surface oxygenated groundwater, leads to the discharge of predominantly acid-sulfate fluids with various sulfate concentration (100–4,200 ppm) and moderate to high acidity (pH≤4; Joseph et al., 2011).
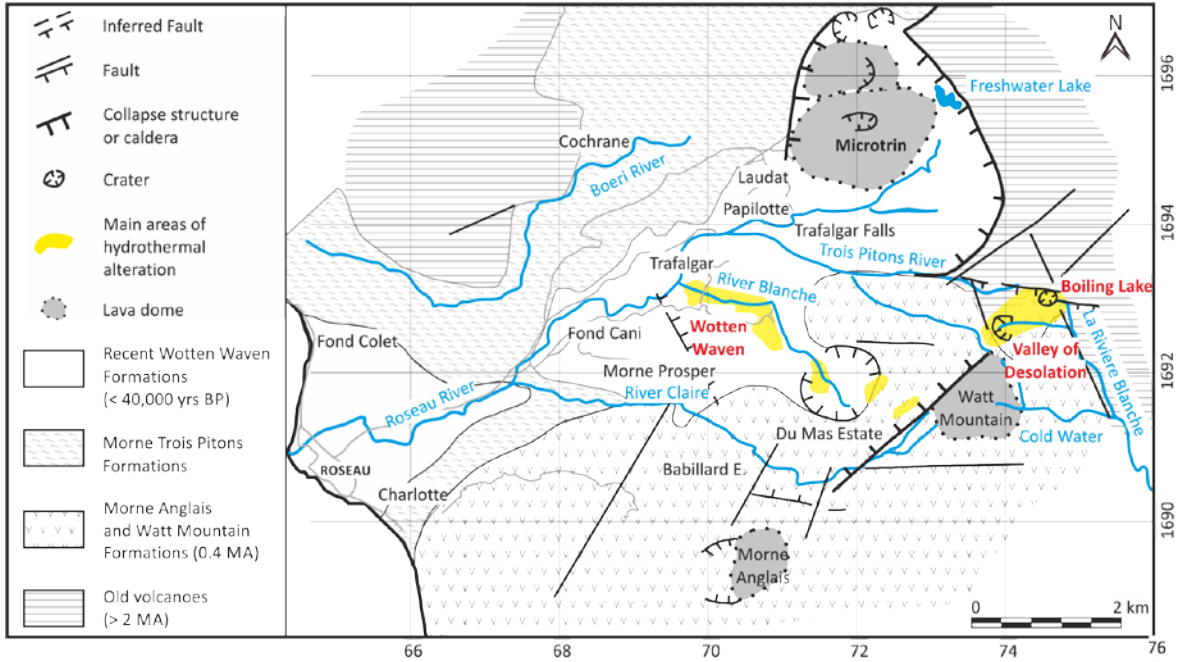
Figure 4.3: Simplified geological map of the Roseau Valley showing faults, inferred faults collapse structures or calderas, craters, lava domes and the main areas of hydrothermal activity (modified from Traineau et al., 2015).

4.3   Eruption history

There is evidence for phreatic eruptions to have occurred from the Valley of Desolation/Boiling Lake area at least since 4 ka (Lindsay, 2005). Based on dated lahar deposits, the oldest eruption within this area happened ~4050 years ago, but no details about the precise vent location are available. In contrast, two other prehistoric eruptions (~3750 and ~2900 years ago) dated by lithic ash deposits are believed to have generated small explosion craters within the Valley of Desolation (Demange et al., 1985; Lindsay et al., 2005). The formation of the Boiling Lake – not being dated and confirmed so far - could possibly have resulted from one of these events (Fournier et al., 2009)
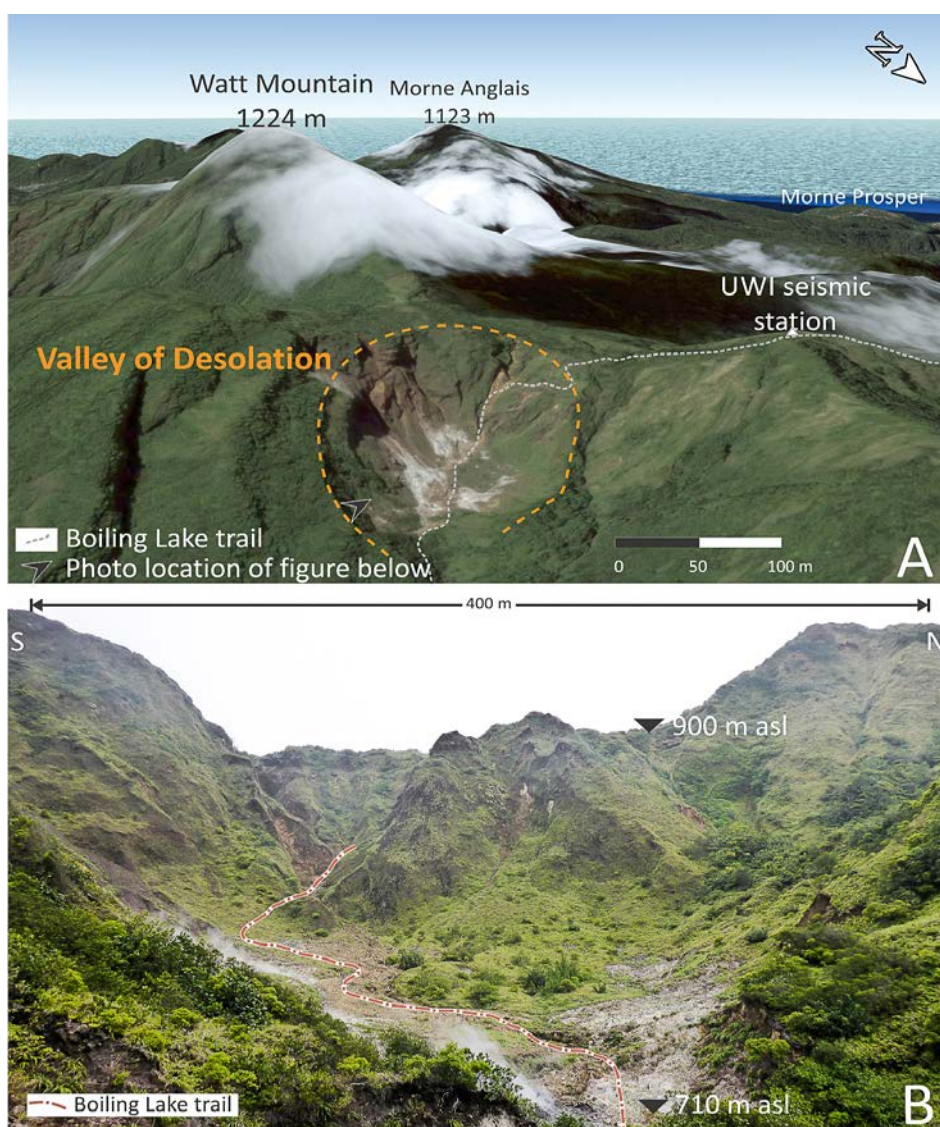
Figure 4.4: (A) Google Earth^{TM} image (2015) showing the outline of the Valley of Desolation (dashed line), the suggested location of the phreatic eruption of January 4th, 1880. (B) Photograph of the Valley of Desolation (2015) surrounded by steep slopes. The Boiling Lake trail (dash-dotted line) enters the valley in the West, passes by the hydrothermal phenomena and exits in the lowest point in the East.

According to several authors (Nicholls, 1880; Watt, 1880; Sapper, 1903; Komorowski and Hammouya, 1998; Lindsay et al., 2005) the first historic phreatic event from the Valley of Desolation/Boiling Lake area occurred on January 4th 1880. But there is evidence for the area named as the Eastern Hot Springs (Robson and Willmore, 1955) to be the source of an earlier eruption in 1863 (Sapper, 1903; Demange et al., 1984; Demange et al., 1985; Traineau et al., 2015). The 1880 event, which generated from the Valley of Desolation on January 4th, is much better documented, and speculated to be associated with a decrease in barometric pressure during heavy rainfall in the area (Nicholls, 1880). Some other authors (Nicholls and Watt, 1880; Nicholls, 1880) suggest a reactivation of a previously active crater, characterized by solfataric activity prior to the event. The eruption lasted for several minutes and caused ash fall in an area of at least 50 km^2 and up to a distance of 19 km to the West including the city of Roseau, which was covered by few millimeters (Nicholls, 1880). The very violent non-magmatic steam eruption ejected rocks and boulders, consisting of mineral fragments and altered material, and did not contain any juveniles (Daubrée 1880a, b; Wadsworth, 1880). Within and beyond the crater edge, trees were destroyed by ballistics and the ground was covered by debris up to one meter in size (Nicholls, 1880). Endlich (1880) estimated a total volume of 27 million tons for this eruption, which generated a WSW–ENE elongated ovoid crater with a depth of ~180 m and breached to the NE. These dimensions correspond well with the topography of the valley today, even though considering post-eruptive wall collapse and intense denudation due to weathering (Figure 4.4). The eruption caused furthermore a lahar-like flooding in the Roseau River and also the river Rivier Blanch, which finally drains into the sea via the Point Mulatre River (Endlich 1880; Nicholls, 1880).

Sapper (1903) visited the Valley of Desolation/Boiling Lake in 1903 and investigated the area in detail. He mapped and described hydrothermal features including temperature measurements within three distinct craters. Figure 4.5 shows the Boiling Lake located within the easternmost crater (Crater III), a second crater (Crater II), which was characterized by strong activity but also clear signs of regrown vegetation along the crater walls and a third crater (Crater I), the Valley of Desolation – formerly known as Sulphur Springs (Sapper, 1903). The features observed within the Valley of Desolation itself in 1903 were distributed within a flat-floored, crater. This depression was slightly inclined towards the northeast and free of vegetation (Sapper, 1903). Nevertheless ascribing the strongest hydrothermal activity of the investigated area to the Valley of Desolation, Sapper (1903) surprisingly had doubts and did not consider it being the location of the 1880 eruption. This consideration is contradicting to observations made just days after the eruption, which clearly confirm the Valley of Desolation being the source location, specifying elevation, distance and direction to the Boiling Lake as well as crater shape and morphology (Eldridge, 1880; Endlich, 1880; Nicholls, 1880).
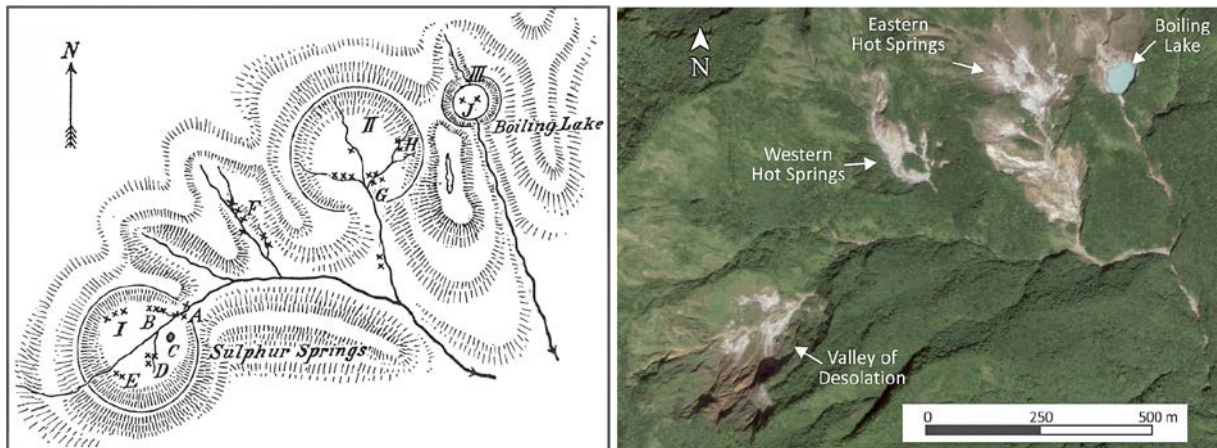
Figure 4.5: Map of the Valley of Desolation/Boiling Lake area (left) indicating morphological craters and hydrothermal features (modified after Sapper, 1903). The features indicated within the map are: [*A*] steaming, bubbling hot spring (92 °C) and highly spraying mineral spring, [*B*] strongly steaming fumaroles (96 °C) surrounded by sulphur precipitations and several small fumaroles along the northern crater margin, [*C*] bubbling and spraying mud pools (max. 7 m diameter; 84 °C), [*D*] spraying fumaroles (2 m high; 94.5 °C), [*E*] several small fumaroles and hot springs (92 °C), [*F*] strong fumaroles and several hot springs (max. 95 °C), [*G*] vigorously bubbling hot spring (80 °C) and several other springs and [*H*] two springs (40.5 °C / 42 °C). Recent Google Earth™ image showing the same area in 2015 (right). Note the striking similarities between the hand drawn map and the satellite image.

A recent phreatic event occurred on the 8th/9th of July 1997 during a strong tropical wave with heavy rain. This eruption, also not directly witnessed, was significantly smaller in size than the eruption in 1880 (James, 1997). The event was suggested to have been triggered by a landslide from the foothill of Morne Watt into the Valley of Desolation (James, 1997). This might have happened on the same day, or some days before the eruption (James, 1997). Due to the covering of fumaroles and steaming vents in the southwestern part of the crater shaped valley, an effective outgassing was hindered in that area, which in turn led to the pressurization of the subsurface and finally resulted in a small-volume phreatic eruption (James, 1997). According to observations made on July 13th, a small eruption crater, which contained a bubbling mud pool was superseded by a ˈMini valleyˈ (Figure 4.6). This gully-like feature was created by the erosion of surface waters into the loose material within the proximity of the eruption crater (James, 1997). Furthermore the 2.5–7.5 m deep and 19-m-long valley contained at least eight fumaroles and a hot spring (85°C) (James, 1997). Mud, pebbles and sulphur-bearing chunks of rocks have been found ejected primarily to the western area of the ˈMini valleyˈ up to a distance of 53 m (James, 1997) (Figure 4.6).
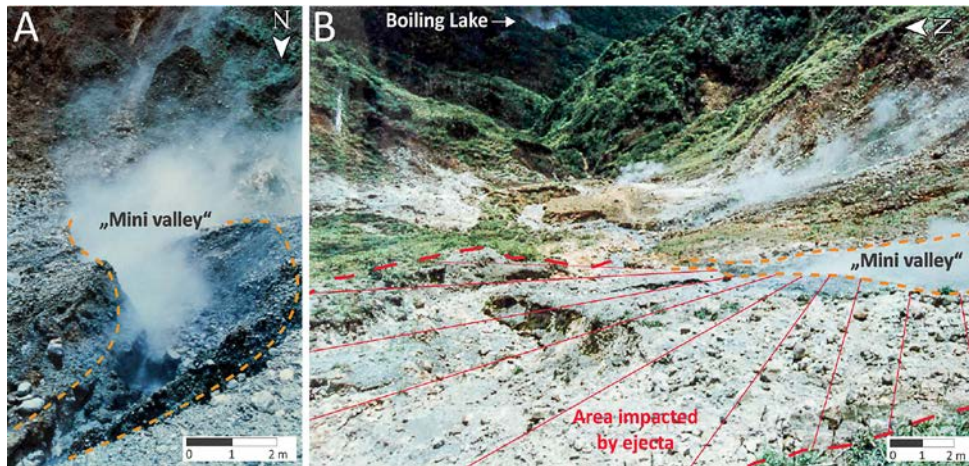
Figure 4.6: Photographs taken by A. James ~5 days after the 1997 phreatic eruption in the Valley of Desolation. (A) Following the eruption, the crater was affected by erosion of surficial runoff, which changed its shape and created a gully-like ˈMini valleyˈ surrounded by loose phreatic debris. (B) Distribution of ejecta mainly in a sector from the North to the South-South-West of the vent location (modified after James, 1997).

Since this event, the Valley of Desolation shows vigorous hydrothermal activity and its morphology undergoes steady change. The activity of fumaroles and the discharge of springs experience slight fluctuations possibly due to rain and landslide events, but without showing significant variations in chemistry (Jeffrey, pers. comm.; Joseph et al., 2011). The volcanic rocks of the area are exposed to ongoing weathering and hydrothermal alteration (Lindsay et al., 2005). Following the 1997 eruption, seismic activity is monitored by a seismometer located near the highest point of the Boiling Lake trail west of the Valley of Desolation (James, 1997). Since 2000, bubbling pools are sampled on a regular basis for analysis of fluid chemistry (Joseph et al., 2011).

4.4 Investigated area and lithologies

In order to study hydrothermal activity, its alteration effects and especially the processes controlling the outgassing within the Valley of Desolation, we conducted two field campaigns in April 2013 and May 2015. Field investigations included mapping of hydrothermal features, surficial lithological units, as well as sampling of rocks and unconsolidated material, affected by supergene and hydrothermal alteration.

4.4.1 Mapping of hydrothermal phenomena

The locations of hydrothermal features, such as hot springs, pools of bubbling water and mud, as well as steaming fumaroles within the Valley of Desolation are shown in Figure 4.7. A second map (Figure 4.8) additionally illustrates areas where the soil is affected by hydrothermal alteration, locally characterized by surficial sulphur-rich encrustations. Furthermore areas covered by landslide debris and run off deposits as well as rocks exposed and covered by vegetation were mapped.
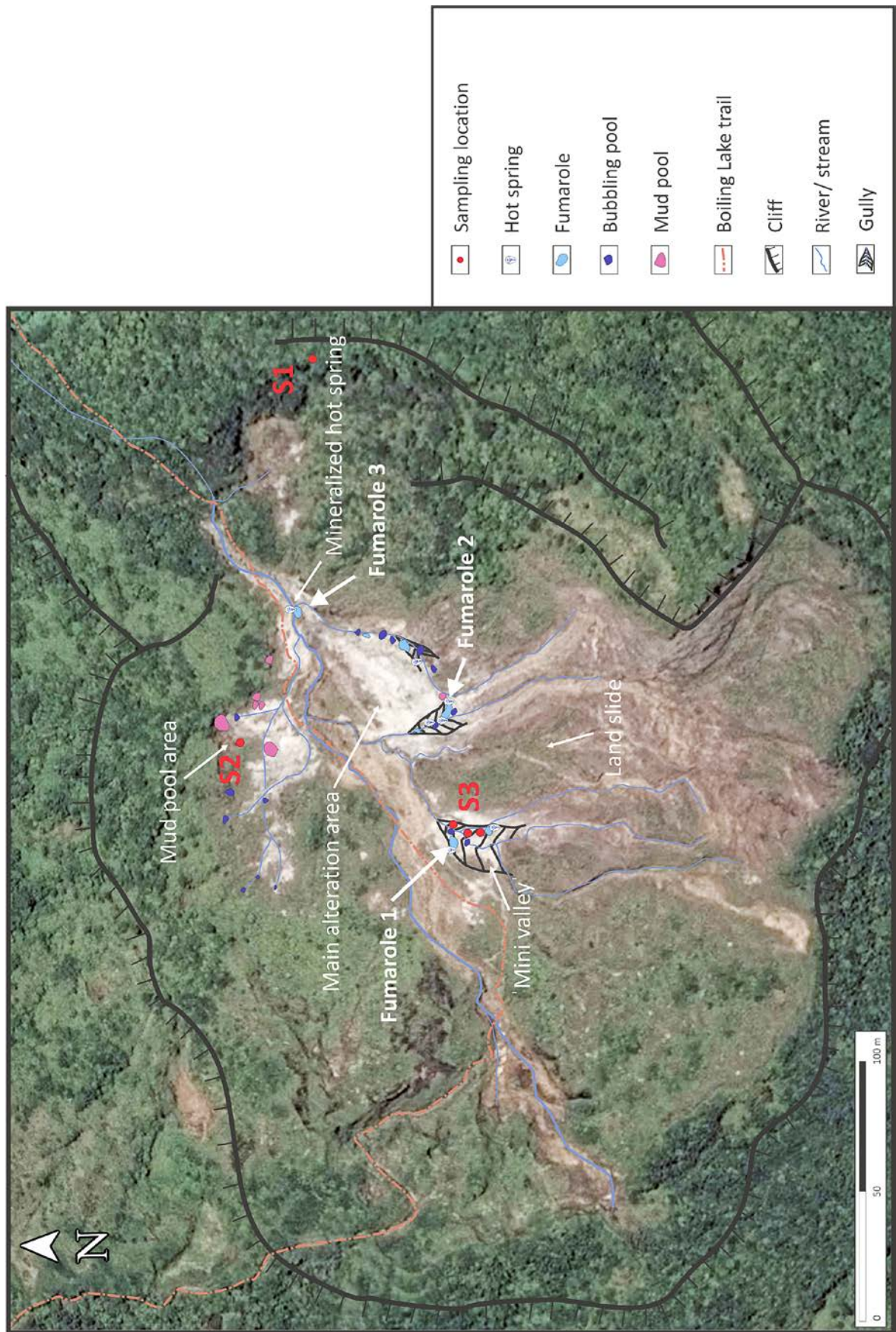
Figure 4.7: Map of the Valley of Desolation (Google Earth™ image; 2015) showing the distribution of surficial hydrothermal features and main outgassing sites during fieldwork in May 2015.
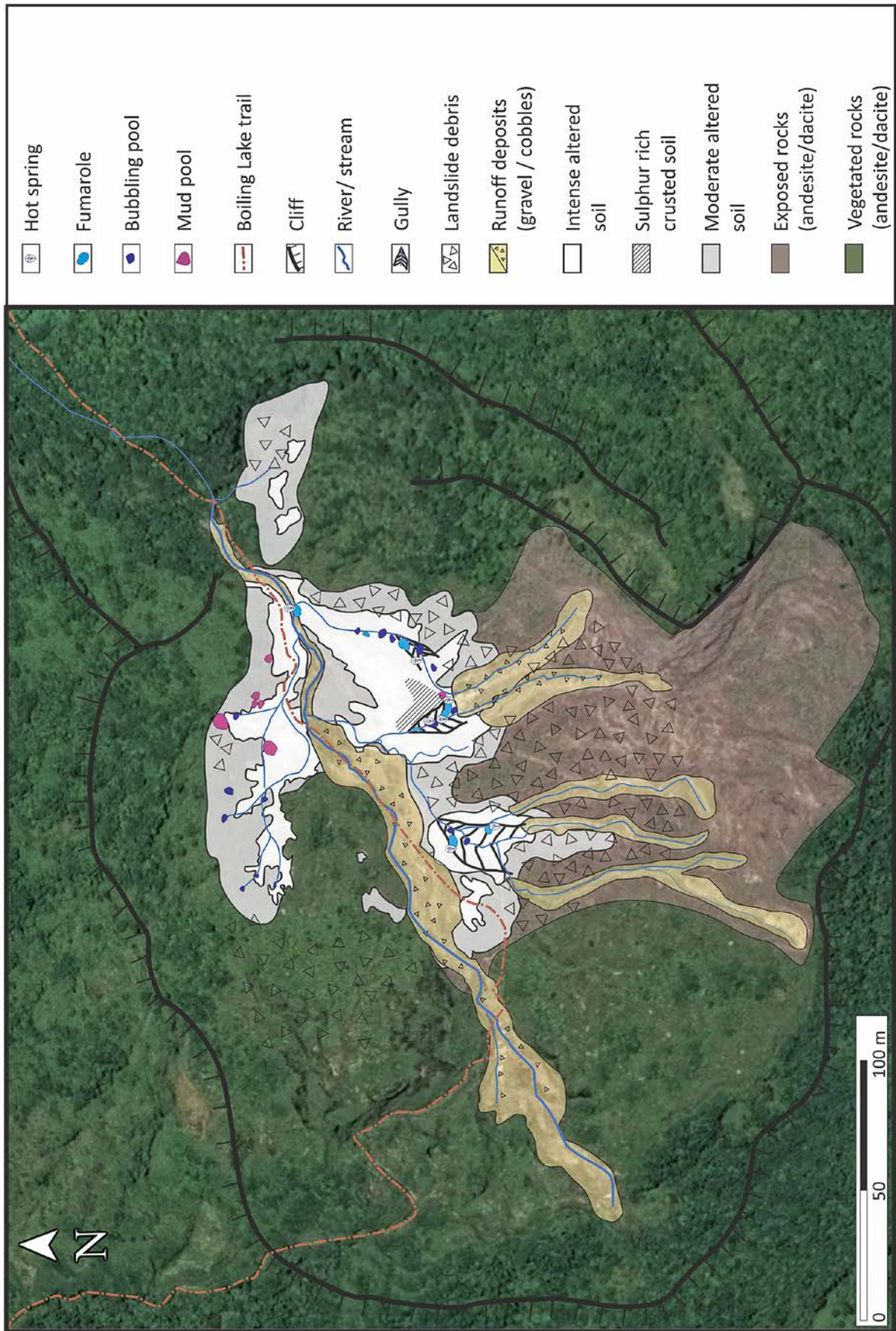
Figure 4.8: Map of the Valley of Desolation (Google Earth™ image; 2015) showing the distribution of surficial hydrothermal phenomena and lithological units during fieldwork in May 2015.
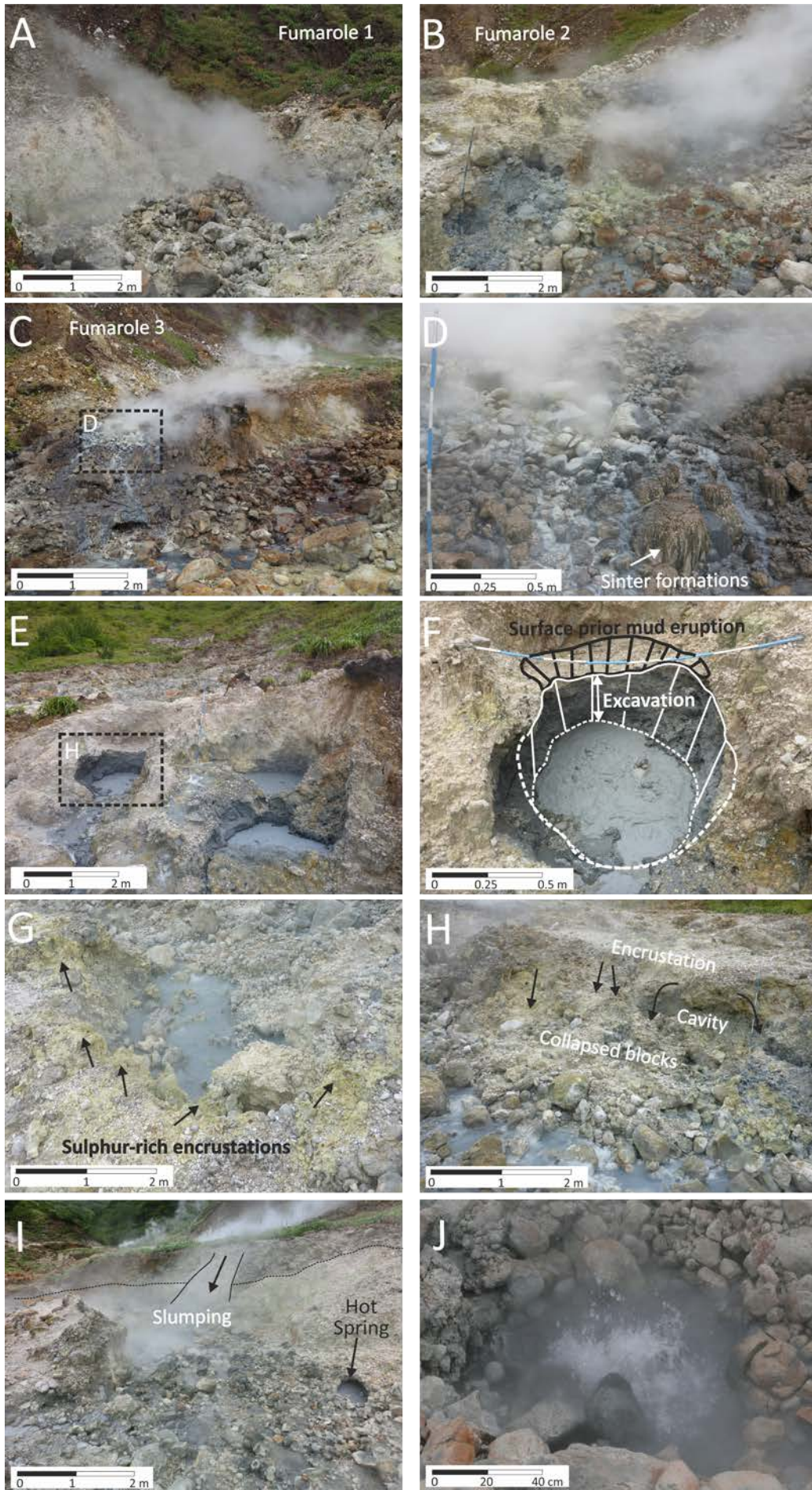
Figure 4.9: Photographs of hydrothermal features from the Valley of Desolation. (A, B) Fumaroles within gullies emitting gas and steam. (C, D) Fumarole and mineralized hot spring showing steam emission and sinter formation. (E, F) Bubbling mud pools showing signs of activity including a recent burst excavating 0.5m of weakly consolidated material. (G) Hot spring emerging from an area characterized by sulphur-encrusted soil. (H) Collapsed blocks of encrusted soil exposing cavities partially filled by bubbling pools. (I) Hot springs, bubbling pools and slumping features along instable walls of the ˈMini valleyˈ. (J) Small bubbling hot spring within stream bed.

Most of the fluids appear at the surface along the Southern and Eastern margin between the lowest areas of the landslide deposits and the somewhat flat-floored central part of the valley. A massive landslide deposit of several meters thickness, originating from the steep slopes of the mountain Watt in the South, separates the hydrothermal active areas containing Fumarole 1 and 2 (Figure 4.9A, B). Both are located within gullies of up to 3 meters depth, several meters width and more than 40 meters length. Fumarole 3 (Figure 4.9C, D), situated in the lowest part of the valley at the northeastern exit, emits primarily steam next to the mineralized hot spring (Traineau et al., 2015). The fumaroles are clearly visible from distance due to their rising steam clouds. The river entering the valley in the Southwest joins with the stream deriving from the ˈMini valleyˈ. It further bypasses the main area of alteration, before it drains the valley between the mineralized hot spring and the easternmost part of the mud pool area. Several mud pools, ranging in size and showing various activity, are located in the lower part of the valley, north of the trail. One of the mud pools showed clear signs of a recent mud eruption (Figure 4.9E, F), which was reported to have occurred few days ago (Jeffrey, pers. comm.). Mud was ejected to a distance of several meters around the pool, including parts of the Boiling Lake trail. Sulfur-rich encrustations appear predominantly along gullies where the main outgassing occurs (Figure 4.9 G, H). Below these encrusted areas, alteration and erosional processes lead occasionally to the formation of cavities, which may cause collapse and slumping of the overburden (Figure 3.9H, I). In addition to these phenomena abundant hot springs, encrustations and alteration features of minor size occur mainly along the river and stream beds (Figure 4.9J).

4.4.2 Investigated lithologies

The soil and deposits in the vicinity of the hydrothermal phenomena show the most distinct effects of alteration. Their properties gradually change with increasing distance to the hydrothermal features resulting in an area characterized by minor effects (Figure 4.8). In some areas north of Fumarole 2, the soil is intensely encrusted by sulphur-rich precipitates (Figure 4.9G). The riverbeds and the tributary streams from the South show continuous processes of erosion and deposition. The beds contain mainly run off deposits in gravel and cobble size (Figure 4.9H, I) The steep southern walls of the Valley of Desolation cause abundant landslides, which reach the main outgassing vents as well as the river and the trail in the axis of the valley. Due to the frequent landslides and the high erosion rates at these walls, parent rocks are exposed and not covered by vegetation (Figure 4.7-4.8). In contrast,

the northern and western part of the valley are densely vegetated, but occasionally small landslides expose the subsurface and in rare locations minor evidences of alteration appear.

In order to investigate the effects of both supergene and hydrothermal alteration on the parent rocks, several locations within the valley have been inspected and sampled (Figure 4.7). Sampling location S1 is located at a cliff in the East of the valley, outside the area affected by hydrothermal alteration. Here a recent landslide created a fresh outcrop, which allowed sampling of the host rock (Figure 4.10A). A second landslide at the northern wall, close to the area of mud pools furthermore allowed the investigation of the parent rock and its supergene alteration products (Figure 4.10B, sampling location S2). Both locations showed changes in macroscopic texture and rock/soil color due to the alteration effects. From the inner grey, slightly altered, andesitic parent rock, a transition to a pitch-black, more intense altered horizon and finally to a brown-orange clay-rich surficial horizon, was observed (Figure 4.10D, E). A similar sequence is present at various locations along the margins of the valley where vegetation permits. This transition from solid andesitic-dacitic rocks to its unconsolidated weathering products represents the typical sequence affected by supergene alteration.
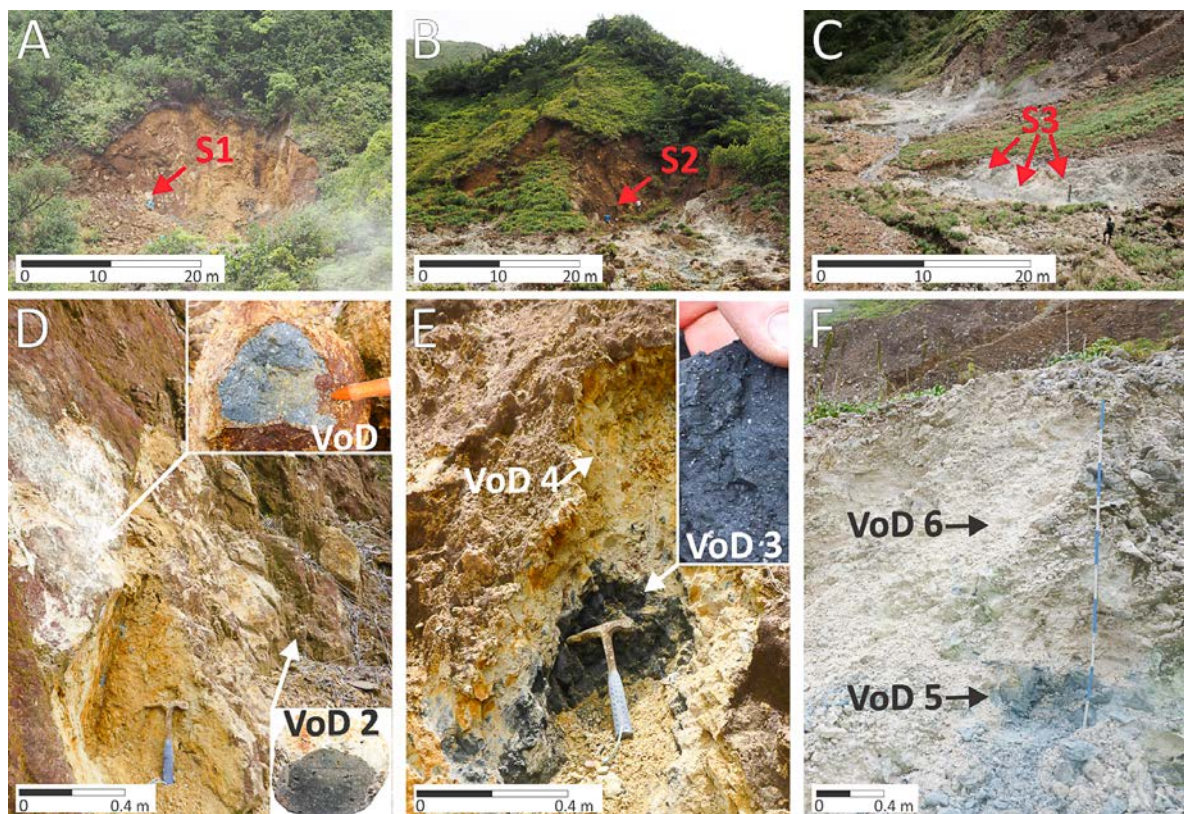
Figure 4.10: Overview and close-up photographs showing the sampling locations within the Valley of Desolation. Sampling locations S1 (A) and S2 (B) were accessible due to recent landslides and contained consolidated and unconsolidated rocks affected by supergene alteration. Sampling location S3 (C) represented by the escarpment within the ˈMini valleyˈ comprised two units of unconsolidated material affected by hydrothermal alteration in the close proximity of outgassing vents. Corresponding close-up photographs show the alteration sequence from VoD 1 to VoD 2 (D), from VoD 3 to VoD 4 (E) and from VoD 5 to VoD 6 (F).

Denudation and erosion processes are removing and transporting most of the altered material into the valley. Then, in the vicinity of hydrothermal vents these reworked rocks and soil experience further alteration clearly affected by hydrothermal activity. Two different types of alteration products were investigated and sampled within the ˈMini valleyˈ (sampling location S3) close to Fumarole 1. Here a 2-meter-deep escarpment comprises a lower section of a clay-rich, homogeneous, blue-grey layer (VoD 5), overlain by a white, heterogeneous and partly loose breccia-like material (VoD 6). To account for heterogeneities both horizons have been sampled and investigated at three locations along the escarpment (Figure 4.10C).

4.5   Methods

Petrophysical and soil mechanical properties have been determined in the field and in the laboratory and correlated with the geochemical composition of the rocks.

4.5.1   Field-based characterization of petrophysical properties

A PL-300 soil permeameter (Umwelt-Geräte-Technik) was used to measure the permeability and the water content of unconsolidated material (Figure 4.11, 4.12A). Samples were taken by using stainless steel cylinders (l = 61 mm; d = 72 mm) and air permeability could be obtained within a measuring range of $5.6E^{-16}\,m^2$ to $6.5E^{-13}\,m^2$. The device determines the gas volume flow through a samples connected pore network based on Darcy's equation. An internal vacuum pump produces the inflow of ambient air through the sample, which is defined over a calibrated throat in the apparatus. The pressure difference over the sample is recorded by a sensor, which provides the pressure gradient of that flow. Comparison of the pressure gradient, in respect to a second gradient over the calibrated permeability of the internal throat, enables the determination of the air volume flow through the sample and consequently the calculation of its permeability. At least three individual samples were taken with the sampling cylinder and connected to the soil permeameter for measurement, in order to account for sample heterogeneities.
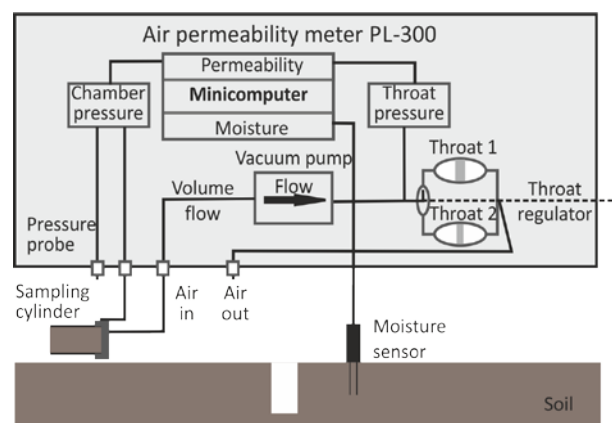
Figure 4.11: Schematic drawing of the PL-300 soil permeameter (modified after Umwelt-Geräte-Technik, 2012).

The obtained air permeability characterizes the water-free pore space of the sample and is therefore a function of the water content. (Makó et al., 2009; Umwelt-Geräte-Technik, 2012). The device is furthermore equipped with a sensor consisting of two stainless steel rods (l=10 cm) to indirectly quantify the volumetric water content by measuring the dielectric constant. The water content is calculated by comparing the obtained dielectric value with calibrated standards of pure water (ε=80) and dry soil (ε=2). The volume affected by the measurement is ~1000 cm^3. Cylinders containing the samples were weighted in order to determine the bulk density. Selected samples were immediately sealed and wrapped for transport. This technique allowed non-destructive sampling and preservation of sample texture and water content required for further analysis in the laboratory. The field characterization of the investigated unconsolidated material was continued using two handheld devices usually applied in soil science. A pocket penetrometer (Figure 4.12B) allowed measurements of the unconfined compressive strength (Zimbone et al., 1996) whereas the undrained shear strength was measured by a torvain (Farquhar, 2001) (Figure 4.12C).
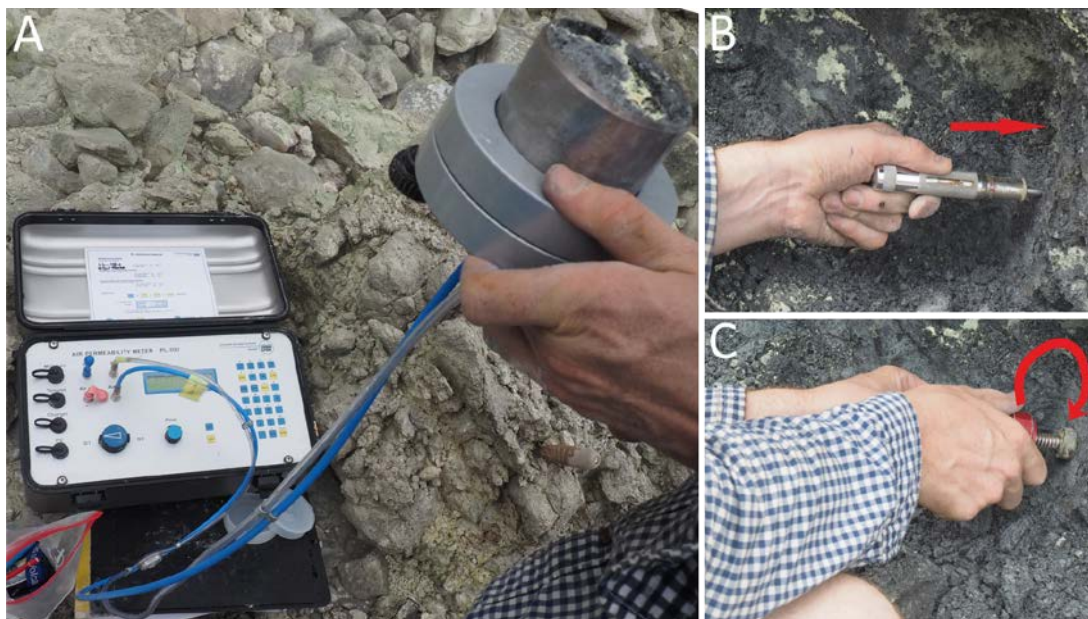
Figure 4.12: (A) Soil permeameter PL-300, (B) pocket penetrometer and (C) torvain during air permeability and strength measurements in the field.

4.5.2 Laboratory-based characterization of petrophysical properties

Collected samples were further characterized in the laboratory, in order to determine rock physical properties. Consolidated rock samples were therefore cored (l = 60mm; d = 25 mm) with their end faces ground flat and dried in an oven at 65 °C for at least 24 h until fully dry. Same drying conditions were applied for unconsolidated samples and sample powders. The latter (produced from every sample) were used for powder density measurements and geochemical analyses.

Samples were weighted prior and after drying in order to determine their water content. Powder density and volume of all cored samples were measured using a helium pycnometer (Ultrapyc 1200e®, Quantachrome). This allowed to define the porosity of the samples, which is a key parameter controlling the mechanical behaviour (Pola et al., 2012). For unconsolidated samples, the dry density and water content was used to calculate the initial porosity within the sampling cylinder of known volume.

Gas permeability of the dried cored samples was obtained by using a benchtop (nitrogen) permeameter under a confining pressure of 1 MPa in order to preclude fluid (nitrogen) flow around the sides of the sample. The device measures confining pressure and gas volume flux by a pressure sensor and a precision gas flow meter under several pressure gradients. This allowed to determine the permeability using Darcy's law.

4.5.3 Geochemical characterization

The bulk geochemical as well as the mineralogical composition of each sample was determined by wavelength dispersive X-ray fluorescence (WD-XRF) and X-ray powder diffraction (XRD) analysis. Sample preparation and analysis was performed in analogy to a previous study, described in Chapter 3.4.1. Geochemical analysis furthermore allowed the determination of the type and degree of alteration, which could be related to the differences in petrophysical properties. The relationship between chemical changes and alteration is evaluated by using five indices, which have been proposed for characterizing the alteration degree of different rocks (Pola et al., 2012, and references therein). These indices, which are based on the weight percentage ratio of major elements, assume that distributions of chemical elements are controlled by the degree of alteration (Duzgoren-Aydin et al., 2002).

4.5.4 Rapid decompression experiments

Unconsolidated samples VoD 5 and VoD 6, collected at the escarpment of the ˈMini valleyˈ, were used for rapid decompression experiments in order to investigate the ejection behavior of heavily altered clay rich material. For details of the experimental setup (Figure 4.13A) and of the general procedure, please refer to subchapter 2.4.2. Samples were carefully pressed in sample holders to ensure preservation of sample texture and water content and subsequently mounted into the autoclave. Experimental conditions were chosen to best mimic steam-flashing during rapid decompression, close to the overpressure and temperature, which we estimated to have caused the phreatic eruption in 1997. Based on the descriptions of James (1997) and the temperature measurements of hydrothermal features (Sapper, 1903; Joseph et al., 2011) a first series of experiments at 115 °C and an initial overpressure of 0.3 MPa was performed. A second series was conducted under slightly higher temperature and pressure conditions of 125 °C and 0.5 MPa (Figure 4.13B). Those conditions, which imply the sudden expansion of heated, liquid water flashing to steam, to be required, (James, 1997) were assumed in order to generate the initiation of a phreatic

eruption as reported. Accumulation of steam and gas below a low permeability cover can be considered to lift the overlying material, which may cause fractures for outgassing. But taking both the distribution of ejecta and the size of the area affected by the eruption into account, this scenario seems to be unrealistic. The expansion of steam and gas in respect to the relative low pressures and temperatures would not release the energy required To account for sample heterogeneities, at least three repeats for each investigated condition and sample were performed.
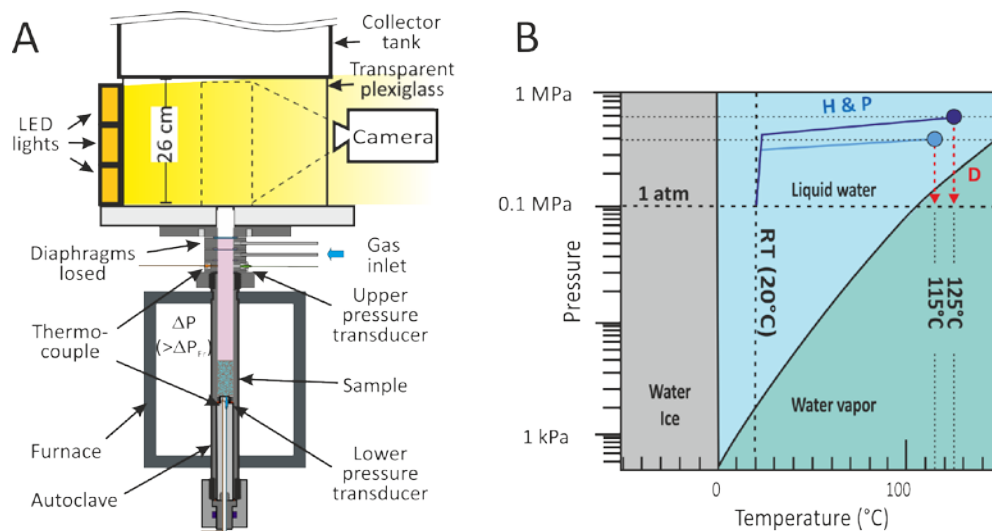
Figure 4.13: (A) Schematic drawing of the experimental setup showing the sample mounted within the autoclave, separated by a set of diaphragms from the collector tank. Particle ejection illuminated by LED lights can be recorded through a transparent plexiglass. (B) Experimental conditions for phreatic fragmentation experiments. Samples are heated and pressurized (H & P) to the dwell conditions until ejection is finally triggered by decompression (D).

Analysis of high-speed video recordings allowed a determination of the particles ejection velocity. The experimental setup was equipped with LED lights, facing towards the high-speed camera (Figure 4.13A), in order to facilitate the tracking of very fine particles ejected within the gas-steam-particle mixture. Tracked particles were grouped by size in ash (<2 mm) and lapilli (>2 mm) and investigated individually.

4.5.5 Ballistic trajectory estimations

In order to estimate the ejection dynamics during a phreatic event similar to the eruption occurring in the Valley of Desolation in 1997, ballistic trajectory distances were calculated. For this approach phreatic deposits, have been considered to be ballistic projectiles (Barberi et al., 1992; Mastin, 1995). Ejection velocity and particle size, which were obtained by high-speed video analysis, as well as particle density determined during the rock physical characterization, were used as input parameter. The ballistic trajectories were calculated using the software Eject! (Mastin, 2001). By assuming a spherical particle shape

and an ejection angle of 45°, maximum trajectory distances could be estimated. Additional information concerning the software Eject! are provided in the documentation (Mastin, 2001). Calculations allowed to analyze the influence of particle size and sample type of both ash and lapilli from VoD 5 and VoD 6 on their trajectory distances.

4.6 Results

4.6.1 Mineralogical and geochemical composition

A conceptual model shows the investigated samples and summarizes their origin as well as their relation in respect to supergene and hydrothermal alteration (Figure 4.14). Results of the geochemical analysis based on XRD and XRF are displayed in Table 4.1 and Table 4.2, respectively.
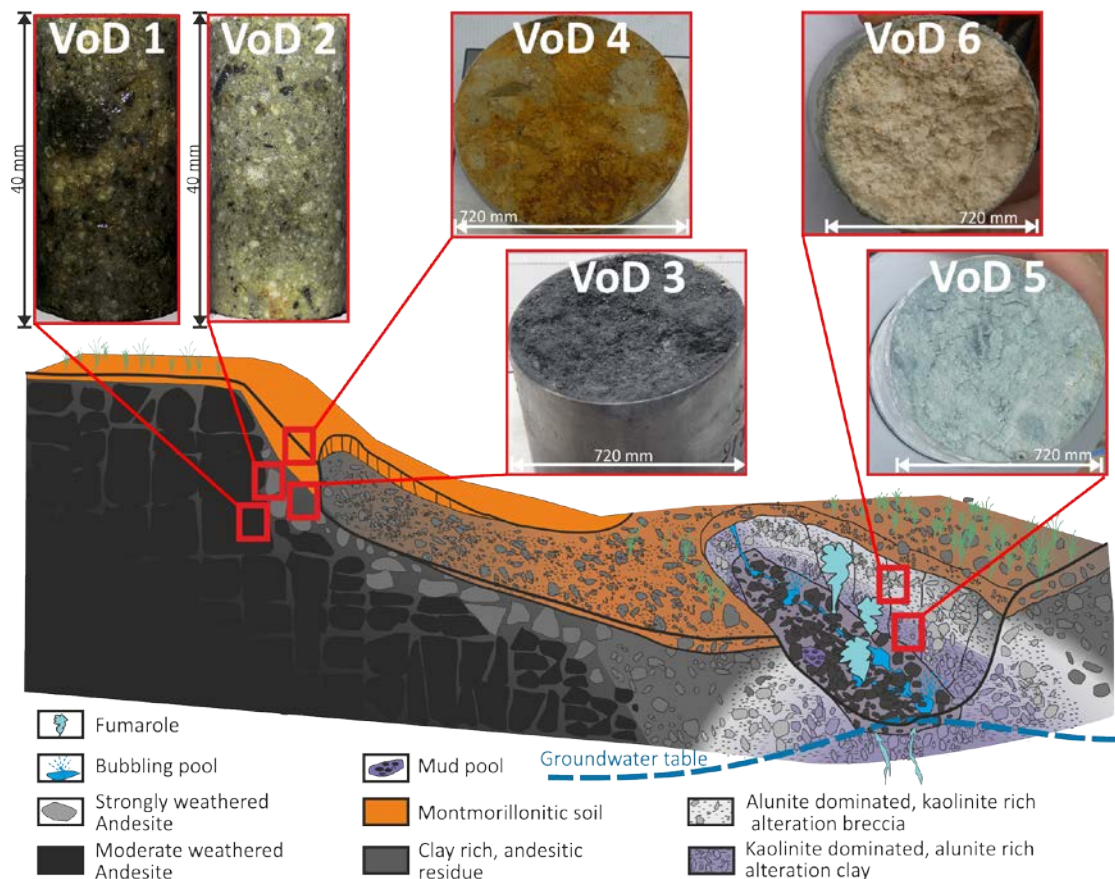
Figure 4.14: Conceptual model of the origin and deposition of the investigated rocks as well as photographs of samples. VoD 1 to VoD 4 represent a sequence from solid to unconsolidated rocks affected by supergene argillic alteration. The progressive decomposition of feldspars results in an increased amount of montmorillonite towards the surface. In the vicinity of hydrothermal vents emitting acid sulphate fluids, rocks are affected by advanced argillic alteration. VoD 5 is dominated by kaolinite whereas VoD 6 shows a lesser degree of alteration characterized by the formation of predominantly alunite at and above the groundwater table.

The following lithologies have been sampled and investigated in detail:

VoD 1 is a dense, volcanic rock with a porphyritic texture. It mainly consists of euhedral plagioclase and sanidine as well as fine-grained cristobalite (<10 μm). Furthermore it contains minor amounts of quartz fragments, euhedral pyrite and hornblende. The latter represent large crystals with an average diameter of up to 850 μm (Figure 4.15A). A significant amount of clay minerals as detected by XRD analysis confirms the weathering of feldspars (Glasmann, 1982).

VoD 2 is very similar in composition but due to a higher degree of alteration, this sample shows a higher amount of clay minerals associated to a decreased proportion of sanidine and plagioclase. Features such as 10-30-μm-wide alteration rims, locally surrounding feldspars, can be observed (Figure 4.15B).

VoD 3 represents the product of progressive supergene weathering. The oxidation of sulfide minerals (e.g. pyrite) to sulfuric acid, creates an acidic environment favoring argillic alteration at low temperatures. Further disaggregation of the rocks towards the surface and the replacement of plagioclase and amphibole by montmorillonite, can be observed, for this hard packed horizon of more than 40 cm thickness (Figure 4.10E). Unlike VoD 1 and VoD 2, which represent solid samples, VoD 3 could be sampled in steel cylinders as other, even further disaggregated and unconsolidated lithologies.

VoD 4 a surficial, yellow-brown horizon (<20 cm) is completely disaggregated and altered, which results in an increased amount of montmorillonite. In agreement with the chemical alteration indices (Table 4.3), which represent the degradation of alkali elements, the degree of argillic alteration increases towards the surface. The clay content accordingly generally increases from 23% (VoD 1) to 73% (VoD 4). Following re-deposition and exposure to sulphur-bearing, acidic fluids (Joseph et al., 2011) these rocks (VoD 1-VoD 4) are eventually affected by advanced argillic alteration.

VoD 5 a blue-grey, clay-rich layer with a visible outcropping thickness of 1.5 m contains locally remnants of the parent rock, which are less altered (Figure 4.16A). Acid sulphate fluids cause leaching and the complete alteration of feldspars to dominantly kaolinite and alunite (Figure 4.15C).

VoD 6 representing the upper part of the escarpment is mainly made up by a white, breccia-like horizon consisting of altered fragments and partially sub rounded clasts (in the size range of pebble), which are embedded in a finer matrix (Figure 4.16B). Some of these clasts comprise a similar andesitic composition as VoD 1 and VoD 2, which is confirming their origin (Figure 4.15B, D). VoD 6 consists mainly of alunite and a lesser amount of kaolinite resulting in a reduced amount of clay (36%), whereas VoD 5 is dominated by kaolinite (58%).

Cristobalite was detected by XRD analysis in all samples. It most possibly formed by devitrification from amorphous volcanic glass or by precipitation from a vapor phase in dome

rocks (Horwell et al., 2013). Due to the fine-grained size of cristobalite it is absent in macroscopic and microscopic observations (Henderson et al., 1971; Horwell et al., 2013).
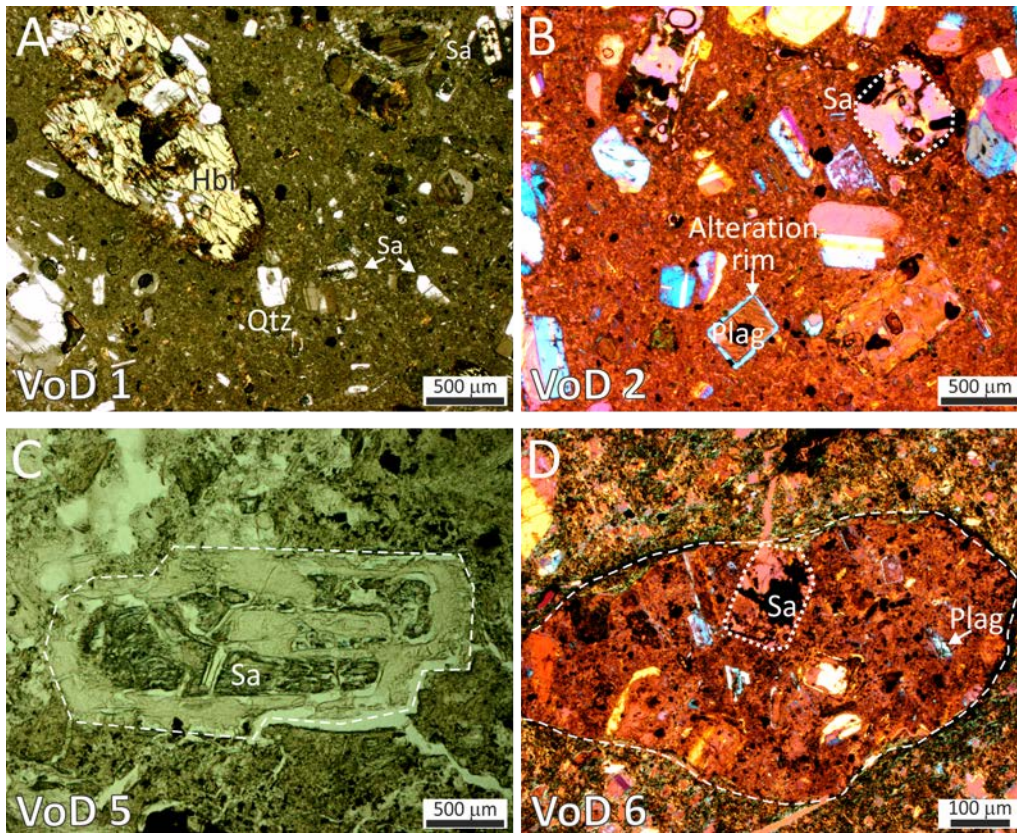
Figure 4.15: Photomicrographs of investigated samples. (A) Hornblendes, sanidines, plagioclase and quartz surrounded by fine-grained matrix, which consists of montmorillonite and cristobalite (Xpol). (B) Plagioclase and sanidines surrounded by a fine-grained matrix of montmorillonite and cristobalite. Furthermore an alteration rim can be observed (surrounding an euhedral plagioclase) (Xpol+γ). (C) Remnant of an euhedral mineral face (most possibly feldspar) intensely altered to kaolinite and alunite within a kaolinized fine matrix (IIpol). (D) Fragment consisting of sanidine, plagioclase, montmorillonite and cristobalite, surrounded by a fine-grained matrix of kaolinite and alunite (Xpol+γ).
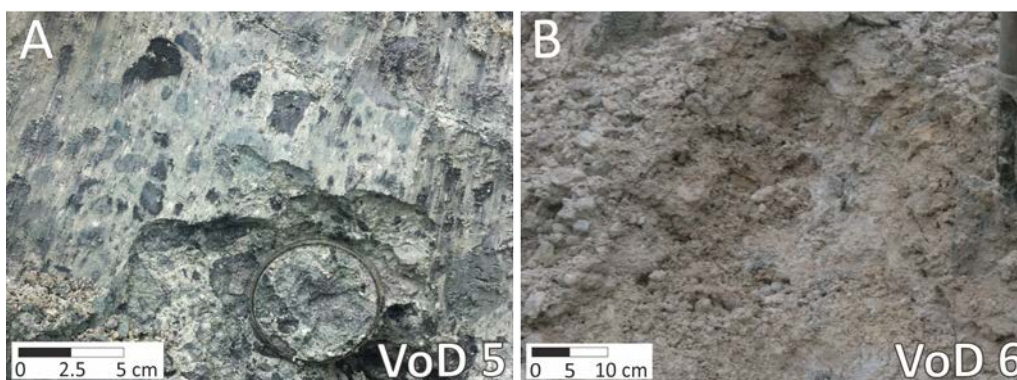
Figure 4.16: Photographs from the sampling location (S3) within the escarpment of the ˈMini valleyˈ. (A) Remnants of darker clasts are embedded in a clay-rich, green-grey matrix (VoD 5). (B) The white, breccia-like horizon is lesser altered and contains loose fragments ranging in size up to several cm (VoD 6).

Table 4.1: Mineral composition of investigated samples based on X-ray diffraction analyses.

| Sample | Supergene alteration | | | | Hydroth. alteration | |
	VoD 1	VoD 2	VoD 3	VoD 4	VoD 5	VoD 6
Plagioclase	37 ± 3	32 ± 3	16 ± 3	18 ± 3		
Sanidine	15 ± 2	12 ± 2	8 ± 2			
Hornblende	2 ± 1					
Clinopyroxene				2 ± 1		
Cristobalite	20 ± 2	23 ± 2	8 ± 2	6 ± 2	15 ± 2	13 ± 2
Quartz	2 ± 1	2 ± 1	5 ± 1	1 ± 1	2 ± 1	4 ± 1
Pyrit	1 ± 1	1 ± 1	3 ± 1			
Alunite[a]					25 ± 3	47 ± 3
Montmorillonite	23 ± 2	30 ± 3	60 ± 3	73 ± 3		
Kaolinite					58 ± 3	36 ± 3
Sum	100	100	100	100	100	100

[a] Includes Na- and K- dominated alunites

Table 4.2: Representative major and trace element analyses of rocks affected by supergene and hydrothermal alteration, examined in this study.

| Sample | Supergene alteration | | | | Hydroth. alteration | |
	VoD 1	VoD 2	VoD 3	VoD 4	VoD 5	VoD 6
Major elements (%)						
SiO_2	61.5	65.1	59.2	54.8	54.5	49.8
TiO_2	0.5	0.6	0.6	1.0	0.6	0.5
Al_2O_3	17.0	17.5	17.5	20.2	19.2	13.5
Fe_2O_3	5.8	3.7	6.3	7.9	3.9	2.9
MnO	0.1	0.1	0.1	0.1	0.1	0.1
MgO	1.6	0.9	1.7	3.6	0.7	0.9
CaO	5.2	3.7	3.5	3.4	0.7	2.7
Na_2O	3.0	2.8	1.5	1.4	1.0	2.1
K_2O	1.6	1.7	1.1	0.2	1.4	1.2
P_2O_5	0.1	0.1	0.1	0.1	0.1	0.2
SO_3	0.7	0.3	0.6	0.4	10.7	10.7
LOI	3.4	2.9	9.3	6.8	17.6	26.4
Sum	99.8	98.9	99.4	99.8	99.7	100.0
Trace elements (ppm)						
Ba	267	266	220	115	0	544
Cr	<20	<20	<20	128	<20	<20
Cu	48	82	71	<30	117	92
Ni	7	1	<20	<20	70	50
Rb	53	55	31	<30	48	40
Sr	192	161	102	90	192	133
Y	40	30	21	17	0	0
Zn	90	46	99	96	52	59
Zr	103	103	113	77	87	74

Table 4.3: Chemical alteration indices for volcanic rocks from the Valley of Desolation affected by supergene and hydrothermal alteration.

Sample	Supergene alteration				Hydroth. alteration	
	VoD 1	VoD 2	VoD 3	VoD 4	VoD 5	VoD 6
CIA	63.6	68.1	74.2	80.2	86.1	69.5
ACN	0.68	0.73	0.78	0.81	0.92	0.74
SA	3.61	3.73	3.38	2.71	2.84	3.69
PIA	65.5	70.8	76.6	80.6	91.3	72.2
CIW	67.6	72.9	77.8	80.8	91.9	74.0

The indices used to estimate the degree of alteration assume the immobility of aluminum and should therefore be carefully applied to heterogeneous samples, especially in environments of hydrothermal alteration (Arıkan et al., 2007; Pola et al., 2012). Nevertheless the values of the indices correlate well with the degree of alteration observed for the investigated rocks. CIA, ACN, PIA and CIW values generally rise due to the loss of mobile cations within the sequences of supergene and hydrothermal alteration. By contrast the SA value decreases with alteration as it is reflecting the loss of silica. For further information concerning formula and references of individual indices shown in Table 4.3, please refer to Chapter 1.2. Loss on ignition correlates with the amount of clay minerals (Arıkan et al., 2007) and shows a large increase due to the presence of alunite formed by hydrothermal alteration.

4.6.2   Petrophysical properties of collected samples

Rock physical and mechanical properties determined in the field and the laboratory are displayed in Table 4.4. Humidity, water content and strength were only measured for the unconsolidated samples. Moreover the unconfined compressive strength (UCS) of VoD 3 was exceeding the range of the device (5.0 kN/m^2). In situ humidity of unconsolidated samples ranged between 34.9 and 87.8 % and was slightly higher than the water content determined in the laboratory by drying (26.3–67.3 %). The differences originate most possibly from the sample heterogeneities and the loss of water during sample shipping and unpacking. Samples have been exposed to significant temperature and pressure changes during the transport, which might have induced changes in the water distribution within the sample cylinders.

Bulk and matrix density ranges between 1.52–1.74 g/cm^3 and 2.56–2.76 g/cm^3 for unconsolidated, as well as between 2.18–2.22 g/cm^3 and 2.49–2.61 g/cm^3 for solid rocks, respectively. Gas permeability could be obtained for all samples besides for VoD 5, which was too low permeable and therefore exceeded the range of the soil permeameter ($<5.6 \times 10^{-16}$ m^2). Results given in Table 4.4 are averaged on three individual measurements (deviating for each sample within the same order of magnitude as the obtained average

value) and range between 2.5 x 10^{-15} and 2.1 x 10^{-14} m^2. Finally UCS and shear strength of investigated samples varies between 0.9–2.4 kN/m^2 and 0.8–3.1 kN/m^2, respectively. These results confirm that strength of unconsolidated samples decreases with 1) an increasing clay content, and 2) an increasing degree of alteration for samples affected by supergene (VoD 3 and VoD 4) and hydrothermal alteration (VoD 5 and VoD 6).

Table 4.4: Averaged petrophysical properties obtained during field and laboratory analysis.

Sample	Humidity PL-300	Water content	Clay content	Bulk density	Matrix density	Connected porosity	Gas permeability	UCS	Shear strength
	(%)	(%)	(%)	(g/cm^3)	(g/cm^3)	(%)	(m^2)	(kN/m^2)	(kN/m^2)
VoD 1	n.m.	n.m.	23	2.22	2.61	14.8	2.5 x 10^{-15} [a]	n.m.	n.m.
VoD 2	n.m.	n.m.	30	2.18	2.49	17.3	8.5 x 10^{-15} [a]	n.m.	n.m.
VoD 3	34.9	26.3	52	1.74	2.58	50.2	3.6 x 10^{-15} [b]	> 5.0	3.1
VoD 4	41.5	32.1	73	1.58	2.76	65.5	2.1 x 10^{-14} [b]	0.9	1.6
VoD 5	87.8	67.3	58	1.56	2.56	73.1	<5.6 x 10^{-16} [b]	1.4	0.8
VoD 6	54.9	49.9	36	1.52	2.56	65.5	9.4 x 10^{-15} [b]	2.4	2.7

[a] Gas permeability determined by benchtop permeameter under a confining pressure of 1 MPa

[b] Air permeability determined by PL-300 soil permeameter (Umwelt-Geräte-Technik)

4.6.3   Ejection behavior

The ejection velocity of the gas-particle mixture in the presence of steam-flashing was determined by high-speed video analysis of each experiment. The energy released during decompression and thereby driving the unloading and ejection of samples is controlled by the amount of water in the system. Thereby porosity and sample saturation are the main parameter affecting the ejection dynamics of particles during rapid decompression experiments (Rager et al., 2014; Mayer et al., 2015). We observed a non-linear decay of the ejection velocity as a function of time irrespective of the particle size (Figure 4.17). Grouping particles of each sample type (VoD 5 and VoD 6) and each condition (3 bar/115 °C and 5 bar/125 °C) by size into lapilli (>2 mm) and ash (<2 mm) revealed following results:

(1) Independent of the condition, initially ejected particles are smaller than 500 μm and exhibit the highest ejection speeds (55–70 m/s) (Figure 4.18A, D);

(2) Lapilli sized particles (>2 mm) arrive at a later stage of the ejection (12.5 ms) and show slower ejection velocities (25–50 m/s) (Figure 4.18B, E);

(3) Higher initial pressures and temperatures result in higher ejection speeds for ash and lapilli-sized particles of both sample series (65–80 m/s and 40–50 m/s for ash and lapilli from VoD 5 compared to 55–70 m/s and 25–40 m/s for ash and lapilli from VoD 6) (Figure 4.17);

(4) As a result of the samples' water content VoD 5 (67.3%) showed higher ejection speeds under both conditions and for both size groups compared to VoD 6 (49.9%);

(5) During video analysis and collection of particles from the tank after the experiment, a higher amount of coarse particles from VoD 6 samples was noticed (Figure 4.18).
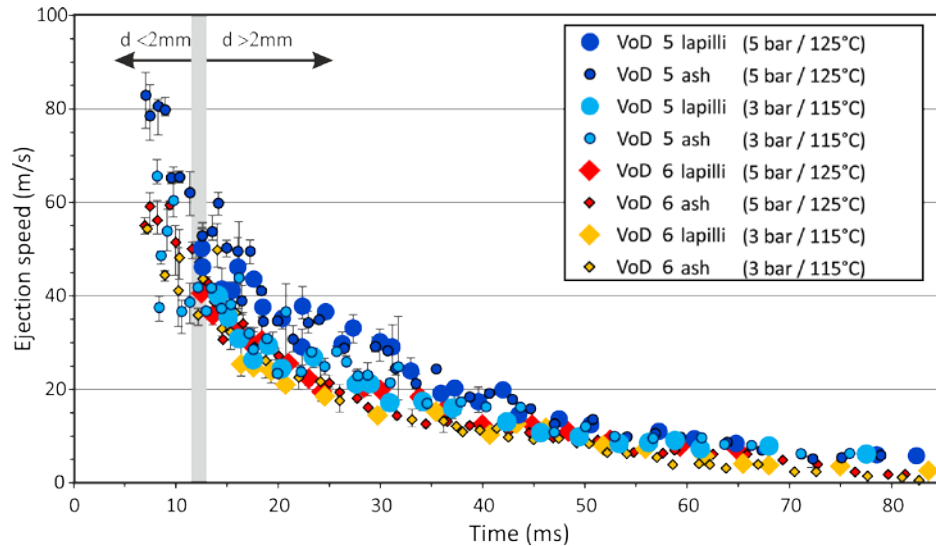
Figure 4.17: Ejection speed of particles determined by analysis of high-speed camera footage. The velocity of the particles decays with time. Coarser particles (d >2 mm, with d = particle diameter) exhibit lower ejection speeds and appear in the field of view at a later stage of the ejection.
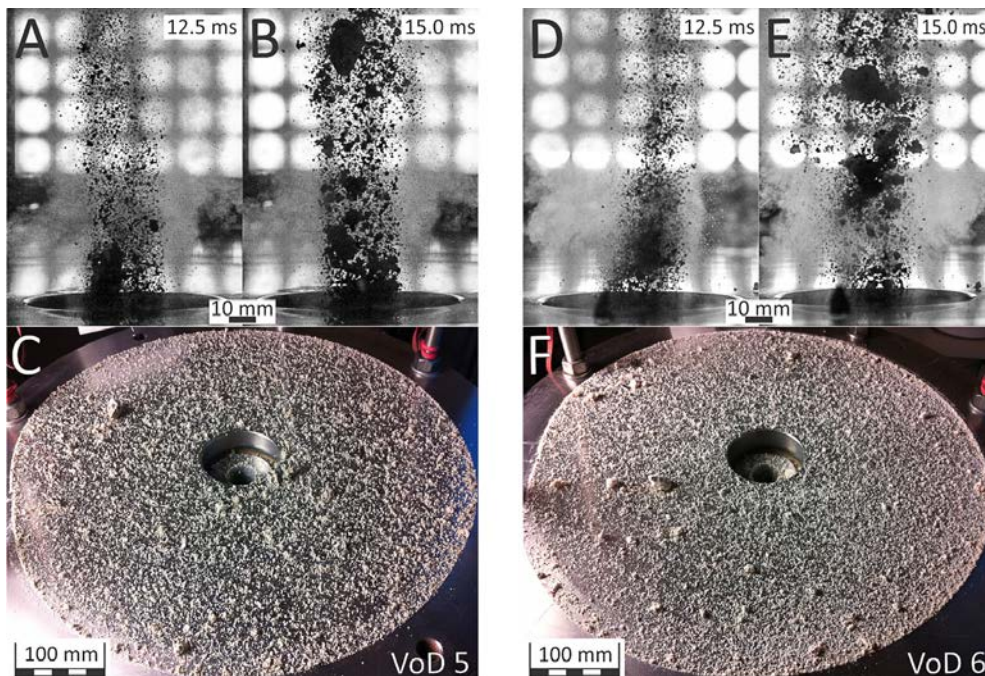
Figure 4.18: Sequences of still-frames from high-speed camera recordings showing the ejection of particles at different times after the initiation of the decompression. Ash and lapilli-sized particles from the sample VoD 5 during ejection (A, B) and prior collection at the bottom plate (C) and from VoD 6 respectively (D, E, F). The onset of the ejection is characterized by the expulsion of fine particles followed by a mixture of fine and coarse particles. Note the differences in the amount of coarse particles at the bottom plate.

4.6.4 Ballistic trajectory

Using the program Eject! (Mastin, 2001) allowed to estimate the minimum and maximum ballistic trajectory distances. A size range for ash (1–2 mm) and lapilli (2–10 mm) was assumed to calculate the minimum and maximum trajectory distance for both investigated samples under each condition (Table 4.5). Minimum and maximum trajectory distances obtained for VoD 5 are slightly higher than for VoD 6. For both samples they increase with particle size, ranging between 21–24 m for ash and 35–65 m for lapilli. The quite narrow range of applied initial overpressure and temperature of this study does not have a significant influence on the estimated distances.

Table 4.5: Estimated trajectory distances based on ejection speeds obtained during decompression experiments by high-speed video analysis. For the calculation the in situ bulk density was used and an ejection angle of 45° was assumed.

Sample	Size	P	T	V_{eject}	$Traj_{min}$	$Traj_{max}$
		(MPa)	(°C)	(m/s)	(m)	(m)
VoD 5	lapilli	0.5	125	50	20	65
VoD 5	ash	0.5	125	80	12	24
VoD 5	lapilli	0.3	115	40	18	56
VoD 5	ash	0.3	115	65	11	22
VoD 6	lapilli	0.5	125	40	17	40
VoD 6	ash	0.5	125	70	11	21
VoD 6	lapilli	0.3	115	25	13	35
VoD 6	ash	0.3	115	55	10	21

4.7 Discussion

Field work and laboratory investigations in combination with a detailed literature research allowed to gain further insight in the past and present hydrothermal activity, including phreatic eruptions in the Valley of Desolation. Detailed maps of the Valley of Desolation showing the distribution of hydrothermal phenomena and lithological units, as observed between 2013 and 2015, were presented. Moreover the results highlight the effects of supergene and hydrothermal alteration on the rock physical and mechanical properties. Decompression experiments and analytical modelling further allowed to reconstruct the dynamics of a recent phreatic event in 1997.

4.7.1 Hydrothermal activity

In the Valley of Desolation the spatial distribution of hydrothermal phenomena is most likely controlled by the structural setting (Traineau et al., 2015). Nevertheless their intensity and style seem to be subject to some variations influenced by alteration processes

at the surface and at shallow depth. Documented reports of the activity in the area since the eruption in 1880 seem to be rare. Apparently the only information available was recorded following the phreatic eruption in 1997 (James, 1997) and even more recent studies (e.g. Lindsay, 2005; Joseph et al., 2011; Di Napoli et al., 2013). Therefore, clear statements of a changing activity especially due to alteration processes are hardly possible. Comparing the mapping results with the descriptions, made soon after the phreatic eruption of 1880 (Sapper, 1903) and the report from James (1997), yielded the following findings:

(1) Despite denudation and abundant landslides, which changed the topography of the valley, the main hydrothermal features remained their general activity and persisted at their location (Figure 4.5 and 4.7).

(2) The area in the north of the Valley of Desolation, which is characterized by several mud pools, obviously experienced a change in style, as it was previously described as an area of intense fumarolic activity (Sapper, 1903). Advanced argillic alteration causing the formation of low permeability clay-rich layers may lead to increased condensation of fluids at shallow depth. This could in turn have induced a gradual change from emission of gaseous fluids as fumaroles to the development of bubbling mud pools within a liquid dominated shallow zone (Figure 4.9E, F). Such a change in activity might furthermore be favored if located within a depression with little drainage. These mud pools show occasionally an increased activity associated with burst events and minor mud eruptions, which eject hot mud up to several meter distance. Advanced argillic alteration affecting mainly the proximity of hydrothermal vents results in clay-rich material, which exhibits a lower strength and is generally easier eroded than consolidated rocks (Figueiredo et al., 1999). As a result gullies and rills mostly develop in areas where fumaroles, hot springs and bubbling pools are located.

(3) A significantly larger amount of material was ejected during the eruption in 1880 (Watts, 1880) as this event was much more energetic as the recent phreatic eruption in 1997 (Lindsay et al., 2005). According to reports, the generated crater was filled (to a certain extent) by its ejecta, as well as subsequent slumping processes and retrograde erosion of its crater walls (Watts, 1880; Nicholls, 1880; Sapper 1903). Hydrothermal features located mainly along the margin of the oval crater-shaped valley, could therefore be related to the discontinuity between the host rock and the loose reworked material. Such a zone might facilitate the rise of fluids at shallow depth. Similar processes of fluid circulation along a discontinuity have been observed during flank collapse studies in the Lesser Antilles (Boudon et al., 2007) and elsewhere around the world (Waythomas, 2012). Hydrothermal outflow at greater depth is most commonly associated to structural settings (Curewitz and Karson, 1997), which are thought to be the source for the persistent activity in the Valley of Desolation.

4.7.2 Effects of hydrothermal alteration

Geochemical analysis of investigated samples revealed, that two types of alteration are prominent in the Valley of Desolation. Supergene argillic alteration of the host rocks leads to the formation of montmorillonite-rich, unconsolidated material and in turn to the development of a soil-like horizon at the surface (Table 4.1). Advanced argillic alteration by acid-sulphate fluids affects the close proximity of vent locations. It causes leaching and complete decomposition of feldspars and thus formation of kaolinite and alunite (Rye et al., 2003; Zimbelman et al., 2005; Pirajno, 2009). The Valley of Desolation represents a good example for the influence of the water table on the mineral zoning within an advanced argillic alteration sequence. The highly water saturated horizon (VoD 5) in the lower part of the escarpment is dominated by kaolinite whereas the overlying, alunite-dominated layer (VoD 6) showed a lesser amount of water saturation (Figure 4.14). The dominance of alunite over kaolinite in the upper part of the investigated escarpment may indicate, that alunite formation is favored above the water table where atmospheric oxidation of H_2S to H_2SO_4 occurs (Mutlu et al., 2005).

Sequential alteration, as confirmed by the alteration indices, induces the degradation of rock mechanical properties and is furthermore influencing their petrophysical properties (Table 4.4; Pola et al., 2012). The obtained porosities, densities and water contents are typical for clay-rich materials and agree well with the values of residual and volcanic soil investigated in other locations on Dominica and similar volcanic environments (Rouse et al., 1986; Rao, 1996; Hürlimann et al., 2001; Del Potro and Hürlimann, 2009). Moreover the increasing degree of alteration is reflected by decreasing strength - a relation observed for samples affected by supergene and hydrothermal alteration in this study and elsewhere (Del Potro and Hürlimann, 2009). The results confirm previous investigations, which showed that clay formation is associated with intense weakening and destabilization of rocks causing landslides and collapse (Boudon et al., 2007; Del Potro and Hürlimann, 2009, and references therein). Such processes, usually observed at volcano edifices made up of solid rocks (de Vries et al., 2000; Donnadieu et al., 2001; John et al., 2008), can also occur at slopes consisting of unconsolidated material and colluvial deposits (Del Potro and Hürlimann, 2008; 2009). Petrophysical properties of investigated unconsolidated samples support previous studies showing that volcanic soils represent very weak units and that their behavior is furthermore controlled by particle size distribution and water content (Del Potro and Hürlimann, 2008, and references therein). In addition, clay alteration is decreasing the permeability and thereby affecting the outgassing of hydrothermal active areas (Alvarado et al., 2010; Vignaroli et al., 2015).

Surficial sulfur-rich encrustations, which were observed in the close vicinity of the degassing vents (Figure 4.9G, H), could further contribute to a decrease in permeability and create sealing levels within surficial lithological units (Harris and Maciejewski, 2000). Low-permeability lithologies may favor pressurization episodes at shallow depth of

hydrothermally active areas, which eventually lead to phreatic eruptions (Mayer et al., 2015; Montanaro et al., 2016). Such pressurization could be caused by 1) an increased fluid flux to the surface resulting from changes within the hydrothermal system (e.g. rising of the isotherms, changes in the groundwater table); or 2) by constant gas flow but continuously decreasing permeability (due to clay formation and precipitation of secondary minerals). As the lithologies in the vicinity of outgassing vents comprised relative low strength, rupture and decompression might occur at little overpressure and not leading to large eruptions.

4.7.3   Ejection behavior of altered unconsolidated material

The results obtained by rapid decompression experiments with heavily altered, clay-rich material at initial pressures of 0.3 and 0.5 MPa confirmed the influence of particle size on the ejection speed. As most of the kinetic energy is released during the initial stage of the decompression, and smaller particles are more efficiently coupled with the expanding gas and steam, ash-sized particles arriving during an early stage in the field of view, exhibit the highest ejection velocities (Alatorre-Ibargüengoitia et al., 2010). These results are well in agreement with a study performed by Montanaro et al. (2016).

The estimated trajectory distances (up to 65 m) correspond well with the measured maximum distances of debris (52 m) ejected during the phreatic eruption in 1997 (James, 1997), which supports the conditions chosen for the fragmentation experiments. The asymmetrical distribution of ejecta as reported by James (1997) was most likely caused by a lateral jet. Figure 4.19 displays a conceptual model showing a possible evolution of the 1997 phreatic eruption in the Valley of Desolation. The landslide deriving from the steep slopes of the mountain Watt might have caused a uneven coverage of the vent locations, which resulted in a lower overburden towards the valley side. Hence the expansion of fluids was favored in this direction and caused a directed jet of steam and debris to the NW of the source location.
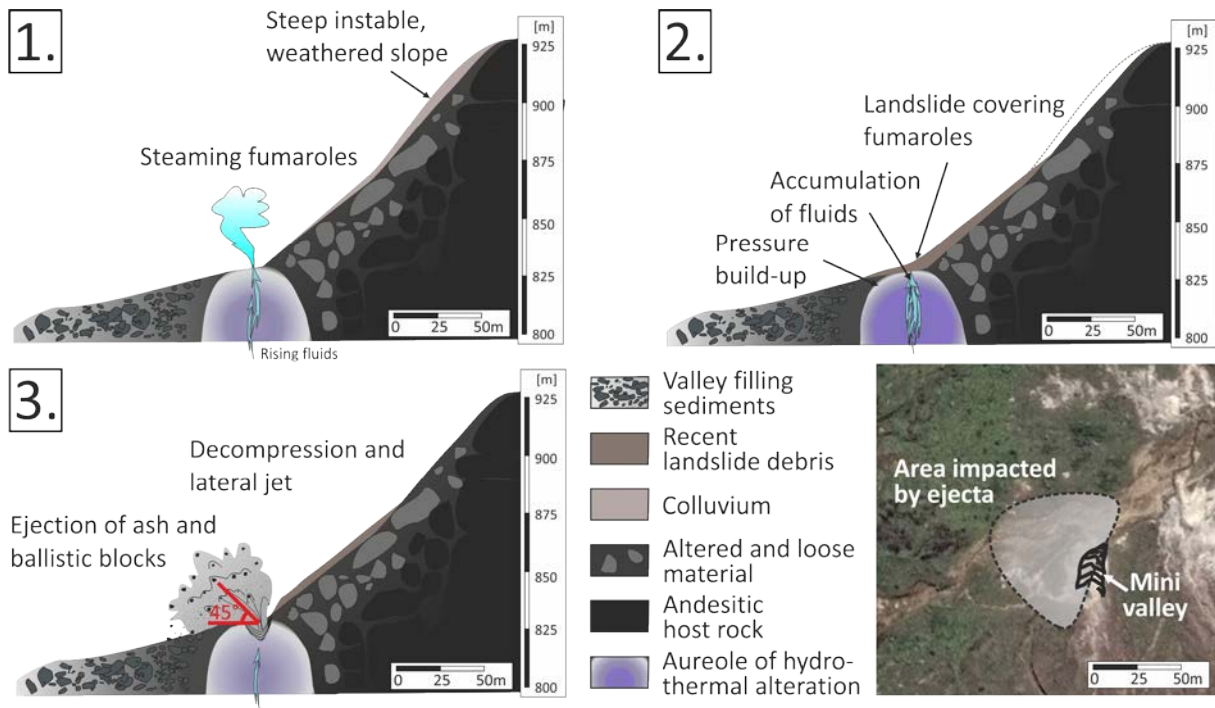
Figure 4.19: Conceptual model showing a possible scenario for the evolution of the phreatic eruption in the Valley of Desolation in 1997. The landslide deposit might have caused an uneven coverage of the vent locations, which most likely resulted in a lateral jet of steam and tephra. The distribution of the ejecta was thereby dominantly in an area in the NW of the source location, as reported by a field investigation (James, 1997).

4.8   Summary and conclusion

Two field campaigns and laboratory analysis was conducted, in order to investigate phreatic activity and alteration processes in the Valley of Desolation,. Detailed mapping of the area included hydrothermal features and surficial lithological units affected by supergene and hydrothermal alteration. The maps, produced by this study, may serve as a basis for further investigation of hydrothermal activity in the area, as they represent a snapshot of activity in an environment subjected to various surface processes, which affect the outgassing style and intensity.

Further field and laboratory-based characterization including in situ permeability measurements of altered unconsolidated rocks revealed several effects of supergene and hydrothermal alteration in the Valley of Desolation:

(1) Rocks within the Valley of Desolation are generally affected by supergene argillic alteration, causing disaggregation and the formation of montmorillonite;

(2) The close proximity of outgassing vents is characterized by advanced argillic alteration and the formation of kaolinite and alunite;

(3) Both types of alteration decreased the strength and permeability of rocks accompanied by increasing abundance of clay minerals;

(4) Advanced argillic alteration in the vicinity of outgassing vents (leading to clay formation and reducing the permeability) may have enhanced the condensation of fluids at shallow depth, therefore inducing the progressive change from steaming fumaroles to boiling mud pools;

(5) Strength reduction of altered rock/soil could have caused destabilization along slope areas, which may have increased the occurrence of landslides, which have the potential to cause the covering of outgassing vents by landslide debris (a similar process most possibly triggered the 1997 phreatic eruption in the Valley of Desolation).

Results demonstrate that the degradation of petrophysical properties, caused by supergene and hydrothermal alteration, is well represented by chemical alteration indices.

Rapid decompression experiments simulated the ejection dynamics involved in small phreatic eruptions and allowed to estimate the conditions leading to such events. Based on the report of the 1997 eruption and the obtained results, a conceptual model for the progression of events, which occur during a landslide-triggered phreatic eruption in the Valley of Desolation is provided.

New techniques for mapping and monitoring of alteration processes, which induce mechanical instability of degassing vents, must be developed for all active volcanoes of the Lesser Antilles (Boudon et al., 2007). The results, presented in this study, may therefore be considered as a contribution to such efforts at the Valley of Desolation and at similar hydrothermally active environments.

This page was intentionally left blank.

5   Synthesis and conclusions

Figure 5.1: View from the eastern rim of Solfatara crater.

This page was intentionally left blank.

5.1 Key findings and general conclusion

Investigations obtained within this thesis focus on the effects of hydrothermal alteration on petrophysical properties, which in turn influence phreatic eruption processes. A combination of rapid decompression experiments and extensive characterization of the rock samples involved was applied to three individual case studies.

A first study on Whakaari investigated the influence of argon gas expansion versus steam flashing on the fragmentation behavior as well as on the size and shape of particles generated during rapid decompression (6.5 MPa; 270 °C). Furthermore the effect of sample type (loose or consolidated) and the amount of secondary hydrothermal alteration, among others alunite precipitation, is demonstrated. The Campi Flegrei case study includes a more detailed investigation of the alteration processes. Samples have been geochemically analyzed prior to rock mechanical characterization and rapid decompression experiments. The fragmentation behavior of consolidated samples with various degree of alteration was investigated in the presence of steam expansion and compared to gas expansion under identical initial pressure and temperature conditions (4 MPa; 240 °C). Additional geochemical and laser scan analysis was conducted to determine the chemical composition and size distribution of the very fine fraction generated during fragmentation. The third case study focused on the distribution and characterization of hydrothermal phenomena within the Valley of Desolation in Dominica. Geochemical and petrophysical characterization of consolidated and unconsolidated clay-rich samples, allowed an investigation of rocks affected by supergene and hydrothermal alteration. Rapid decompression experiments and analytical modelling have been conducted in order to explore the physical conditions (0.3−0.5 MPa; 115−125 °C) inferred for a recent phreatic event driven by steam flashing.

Each of the key aims of this thesis, set out in Chapter 1, are summarized here in light of the findings presented in the preceding chapters.

➢ *Alteration type and its effects on the mineralogical composition of the host rock.*

Although the three case studies are characterized by acid-sulphate alteration, significant differences have been observed mainly as a result of the fluid composition. Besides other parameters, acidity and the concentration of sulfate dictate whether dissolution of the host rock, secondary mineral precipitation of sulfates, or clay alteration is dominant.

Andesitic-dacitic Whakaari samples, which were affected by very acidic fluids (pH: 0.7−2.4) with a very high sulfate concentration (75,000 ppm) are characterized by acid-sulfate alteration. This led to precipitation of amorphous silica and alunite, causing the cementation of the ash tuffs. A similar alteration mineral assemblage was observed for samples from Solfatara and Pisciarelli. The slightly less acidic fluids (pH 1.3−2.5) with a lower sulfate concentration (4,600 ppm) caused leaching of the surficial trachytic rocks associated with replacement of pristine mineralogy by amorphous silica and alunite. Whakaari samples revealed the precipitation of secondary minerals within the pores, which decreased the rock

porosity and permeability. In contrast, the investigated samples from Campi Flegrei are mainly affected by leaching processes, which increased porosity and permeability. Secondary minerals have not been detected to precipitate within open voids of Campi Flegrei samples.

Compared to these two areas, moderate acidic alteration conditions (pH: ≤4) with lower sulfate concentrations (100–4,200 ppm) occur in the Valley of Desolation. This is confirmed by the dominance of kaolinite over alunite within the samples affected by hydrothermal alteration. Moreover the effect of the groundwater table and/or the high soil saturation associated to the tropical climate (i.e. high rainfall) seems to favor the formation of kaolinite by diluting the fluids and decreasing their acidity. Hence, in the Valley of Desolation a transition from kaolinite-dominated and alunite-containing advanced argillic alteration to supergene argillic alteration (outside of the hydrothermal active areas) can be observed.

According to the findings the alteration conditions for Whakaari seem to permit the formation of a mineralogical seal above the hydrothermal system, which seems not to be the case for Campi Flegrei or the Valley of Desolation. However, in the latter area some sectors may experience the development of a low permeability layer due to the formation of clay minerals. Slight variations in fluid composition or local variation in the nature of the rocks might lead to contrary results.

➢ *Influence of alteration on petrophysical properties.*

The rocks investigated in this study cover a wide range of different lithologies from ash tuffs, surge deposits, ash/lapilli to dome lavas, and clay-rich products of advanced argillic alteration. The alteration affecting these rocks generally decreases density and strength while it increases porosity and permeability, unless secondary mineral precipitation or the formation of clay dominates. The latter two processes have been observed for samples from Whakaari and the Valley of Desolation. In both cases alteration reduced the permeability of the rocks, which can affect the outgassing behavior thus leading to a pressurization of the system. For the Whakaari ash tuffs alteration appeared to increase the strength of rocks by progressive precipitation of secondary minerals cementing the samples. Geochemical indices, expressed as weight percentage ratios of major elements, were applied to the altered rocks analyzed in this study. The degradation of petrophysical properties yielded a good correlation with the indices, despite these are mostly used to characterize the weathering degree of rocks.

➢ *Effects of fluid type (i.e. gas or liquid), pressure and temperature on phreatic eruption processes.*

Eruptions driven by steam flashing are significantly more violent than those driven by steam expansion or by pure argon gas expansion. The phase change of water from liquid to vapor results in a tremendous volume increase compared to steam and gas expansion. Hence, the energy surplus enhances the fragmentation process and the ejection of particles. Increased

fragmentation results in higher proportion of fine particles. The energy released during decompression increases with increasing initial pressure (for all experiments) and significantly with increasing temperature (for steam flashing experiments).

> ➤ *Effect of the alteration on the fragmented particle shape and their size distribution.*

Fragmentation of hydrothermally-altered rocks dominated by alunite and amorphous silica produce an increased fraction of very fine particles compared to unaltered rocks. Fine ash particles (<10 µm) possessing silica- and alumina-rich compositions may be causative agents of respiratory diseases, and their dispersion could represent a serious health hazard on a local scale.

A synthesis from the presented studies provides following general conclusions:

(1) Mapping, characterization and monitoring of hydrothermal active sites is vital to understand the behavior of hydrothermal systems over time and allows the detection of changes;

(2) Geochemical investigation as a tool to characterize surficial lithologies provides important insight for the understanding of alteration processes within volcanic system dynamics;

(3) Rapid decompression experiments represent a valuable approach for the investigation of phreatic eruption processes.

5.2   Ongoing work and future perspectives

In the process of this work, a number of new studies started which are currently under investigation at the time of writing.

The results obtained within the first case study together with the successful use of the field soil permeameter during the Dominica case study provided the basis for further field campaigns to Whakaari and Campi Flegrei. In order to better understand the permeability of an active volcanic hydrothermal system, the existing porosity-permeability data of solid rock samples from Whakaari was complemented by porosity and field permeability measurements of fresh, unconsolidated deposits. This study is conducted in collaboration with co-workers from the University of Canterbury and the University of Strasbourg. A combination of macroscopic, microscopic and chemical analysis will be utilized to investigate a possible relationship between physical properties of rocks from the crater floor and alteration. Preliminary results indicate a large variability in alteration and microstructure of investigated samples. Nevertheless, this study will offer the most complete porosity-permeability dataset for a volcanic hydrothermal system to date.

A similar approach has been used to investigate the outgassing processes at Solfatara crater with respect to alteration affecting the crater floor lithologies. This highly active site is

one of the best-studied volcanoes worldwide and represents a significant hazard to the population in the surrounding region. Nowadays no detailed mapping or characterization of the surficial lithologies of the crater floor exists. Fieldwork was conducted in order to address this limitation, by measuring rock and soil permeability, temperature and humidity, and by collecting samples for further lab analysis. In collaboration with several coworkers from the INGV Naples and the University Savoie Mont Blanc who performed detail geophysical investigations of the shallow zone (<50 m) below Solfatara, the study aims to investigate fluid circulation, alteration and outgassing dynamics. The interactions of these processes needs to be better understood (Bruno et al., 2007) as the distribution and type of fluids is essential for quantitative modelling (Byrdina et al., 2014).

Another interesting topic under investigation is the hydrothermal activity of the Eastern Hot Springs and the Boiling Lake. Both locations were examined and sampled during the fieldwork in the Valley of Desolation. Together with the Valley of Desolation, they are expected to be the most likely locations for future eruptions (Lindsay et al., 2005). A similar approach as conducted for the Valley of Desolation is ongoing at the moment. Geochemical and petrophysical characterization, rapid decompression experiments and analytical modeling is applied to estimate the dynamics of phreatic eruption processes in these areas.

Besides these ongoing studies several new questions and possibilities have arisen from this work:

➢ Multidisciplinary studies appear to be promising, in order to further investigate hydrothermal alteration. The analysis of drill cores, geophysical studies as well as field and laboratory-based characterization, might be additionally supported by hydrological and hydrogeological data.

➢ How do fluctuations in the groundwater table influence the dynamics of hydrothermal systems, and can they affect the potential for – or even trigger phreatic events? Groundwater monitoring is already used in volcanic settings for analysis of ground deformation. The distribution of groundwater could also affect alteration processes, as observed for the Valley of Desolation. Therefore the composition and the distribution of groundwater should be investigated and taken into account for future studies.

➢ Geological and structural mapping has been carried out for many hydrothermal areas. But the relationship of these investigations with hydrothermal alteration could be improved. The lateral extent of surficial alteration features and capping layers, has an important control on outgassing locations.

➢ What are the time scales over which hydrothermal alteration occurs? Geochemical modelling and experiments need to be performed in order to better understand the time scales of alteration processes. How fast can the permeability of rocks change and what are the implications of such a change on the heat and fluid flow.

References

Agip, 1987. Geologia e geofisica del sistema geotermico dei Campi Flegrei. Unpublished Internal Report, 17 pp.

Alatorre-Ibargüengoitia, M.A., Scheu, B., Dingwell, D.B., Delgado-Granados, H., Taddeucci, J., 2010. Energy consumption by magmatic fragmentation and pyroclast ejection during Vulcanian eruptions. Earth and Planetary Science Letters, 291(1), 60-69.

Alatorre-Ibargüengoitia, M.A., Scheu, B., Dingwell, D.B., 2011. Influence of the fragmentation process on the dynamics of Vulcanian eruptions: An experimental approach. Earth and Planetary Science Letters, 302(1), 51-59.

Alidibirov, M., Dingwell, D.B., 1996a. An experimental facility for the investigation of magma fragmentation by rapid decompression. Bulletin of Volcanology, 58(5), 411-416.

Alidibirov, M., Dingwell, D.B., 1996b. Magma fragmentation by rapid decompression. Nature, 380(6570), 146-148.

Alidibirov, M., Dingwell, D.B., 2000. Three fragmentation mechanisms for highly viscous magma under rapid decompression. Journal of Volcanology and Geothermal Research, 100(1), 413-421.

Alvarado, G.E., Carboni, S., Cordero, M., Avilés, E., Valverde, M. 2010. Stability of the cone and foundation of Arenal volcano, Costa Rica. In Volcanic Rock Mechanics (pp. 159-166). Balkema Leiden, The Netherlands

Arienzo, I., Moretti, R., Civetta, L., Orsi, G., Papale, P., 2010. The feeding system of Agnano–Monte Spina eruption (Campi Flegrei, Italy): dragging the past into present activity and future scenarios. Chemical Geology, 270(1), 135-147.

Arıkan, F., Ulusay, R., Aydın, N., 2007. Characterization of weathered acidic volcanic rocks and a weathering classification based on a rating system. Bulletin of Engineering Geology and the Environment, 66(4), 415-430.

Barberi, F., Bertagnini, A., Landi, P., Principe, C. 1992. A review on phreatic eruptions and their precursors. Journal of volcanology and geothermal research, 52(4), 231-246.

Baud, P., Zhu, W., Wong, T.F., 2000. Failure mode and weakening effect of water on sandstone. Journal of Geophysical Research: Solid Earth (1978–2012), 105(B7), 16371-16389.

Bergmann, J., Friedel, P., Kleeberg, R., 1998. BGMN—A new fundamental parameters based Rietveld program for laboratory X-ray sources, its use in quantitative analysis and structure investigations. CPD Newsletter, 20, 5-8.

Bishop, J.L., Schiffman, P., Murad, E., Dyar, M.D., Drief, A., Lane, M.D., 2007. Characterization of alteration products in tephra from Haleakala, Maui: A visible-infrared spectroscopy, Mössbauer spectroscopy, XRD, EMPA and TEM study. Clays and Clay Minerals, 55(1), 1-17.

Bixley, P.F., Browne, P.R.L. 1988. Hydrothermal eruption potential in geothermal development. In Proceedings, 10th New Zealand Geothermal Workshop, Geothermal Institute, Univ. Auckland (pp. 195-198).

Black, P. M., 1970. Observations on White Island volcano, New Zealand. Bulletin of Volcanology, 34(1), 158-167.

Bloomberg, S., Werner, C., Rissmann, C., Mazot, A., Horton, T., Gravley, D., Kennedy, B., Oze, C., 2014. Soil CO2 emissions as a proxy for heat and mass flow assessment, Taupō Volcanic Zone, New Zealand. Geochemistry, Geophysics, Geosystems.

Boudon, G., Le Friant, A., Komorowski, J. C., Deplus, C., Semet, M.P. 2007. Volcano flank instability in the Lesser Antilles Arc: diversity of scale, processes, and temporal recurrence. Journal of Geophysical Research: Solid Earth, 112(B8).

Boyce, A.J., Fulignati, P., Sbrana, A., Fallick, A.E., 2007. Fluids in early stage hydrothermal alteration of high-sulfidation epithermal systems: A view from the Vulcano active hydrothermal system (Aeolian Island, Italy). Journal of Volcanology and Geothermal Research, 166(2), 76-90.

Breard, E.C.P., Lube, G., Cronin, S.J., Fitzgerald, R., Kennedy, B., Scheu, B., Montanaro, C., White, J.D.L., Tost, M., Procter, J.N., Moebis, A., 2014. Using the spatial distribution and lithology of ballistic blocks to interpret eruption sequence and dynamics: August 6 2012 Upper Te Maari eruption, New Zealand. Journal of Volcanology and Geothermal Research, 286, 373-386.

Bromley, C.J., Mongillo, M.A. 1994. Hydrothermal eruptions–a hazard assessment. In Proceedings of the 16th New Zealand Geothermal Workshop (pp. 45-50).

Browne, P.R.L., 1978. Hydrothermal alteration in active geothermal fields. Annual Review of Earth and Planetary Sciences, 6, 229-250.

Browne, P.R.L., Lawless, J., 2001. Characteristics of hydrothermal eruptions, with examples from New Zealand and elsewhere. Earth-Science Reviews, 52, 229-331.

Bruno, P.P.G., Ricciardi, G.P., Petrillo, Z., Di Fiore, V., Troiano, A., Chiodini, G., 2007. Geophysical and hydrogeological experiments from a shallow hydrothermal system at Solfatara Volcano, Campi Flegrei, Italy: Response to caldera unrest. Journal of Geophysical Research: Solid Earth (1978–2012), 112(B6).

Buttinelli, M., De Rita, D., Cremisini, C., Cimarelli, C., 2011. Deep explosive focal depths during maar forming magmatic-hydrothermal eruption: Baccano Crater, Central Italy. Bulletin of Volcanology, 73(7), 899-915.

Caliro, S., Chiodini, G., Moretti, R., Avino, R., Granieri, D., Russo, M., and Fiebig, J., 2007. The origin of the fumaroles of La Solfatara (Campi Flegrei, south Italy). Geochimica et Cosmochimica Acta, 71(12), 3040-3055.

Caliro, S., Chiodini, G., Paonita, A. 2014. Geochemical evidences of magma dynamics at Campi Flegrei (Italy). Geochimica et Cosmochimica Acta, 132, 1-15.

Cardellini, C., Chiodini, G., Frondini, F., Granieri, D., Lewicki, J., Peruzzi, L., 2003. Accumulation chamber measurements of methane fluxes: application to volcanic-geothermal areas and landfills. Applied Geochemistry, 18(1), 45-54.

Carlino, S., Piochi, M., Tramelli, A., Troise, C., Mormone, A., Montanaro, C., Scheu, B., Mayer, K., Somma, R., De Natale, G. Small-to-large scale permeability and continuous gradient temperature monitoring of subsurface rocks in volcanic areas: new insights from borehole and laboratory analysis at the Campi Flegrei caldera (Southern Italy). International Journal of Rock Mechanics and Mining Sciences (in review).

Cennamo, P., Ciniglia, C., Valentino, G. M., Stanzione, D., 2002. Interaction between acidic geothermal waters and algae living in Pisciarelli (Naples, Italy). In: Geochimica et Cosmochimica Acta (Vol. 66, No. 15 A, pp. A126-A126). Pergamon-Elsevier Science Ltd.

Chardot, L., Jolly, A. D., Kennedy, B., Fournier, N. Sherburn, S., 2015. Using volcanic tremor for eruption forecasting at White Island volcano (Whakaari), New Zealand. Journal of Volcanology and Geothermal Research.

Chiodini, G., Frondini, F., Cardellini, C., Granieri, D., Marini, L., Ventura, G., 2001. CO2 degassing and energy release at Solfatara volcano, Campi Flegrei, Italy. Journal of Geophysical Research: Solid Earth (1978–2012), 106(B8), 16213-16221.

Chiodini, G., Todesco, M., Caliro, S., Del Gaudio, C., Macedonio, G., Russo, M., 2003. Magma degassing as a trigger of bradyseismic events: The case of Phlegrean Fields (Italy): Geophysical Research Letters, v. 30, 1434.

Chiodini, G., Caliro, S., De Martino, P., Avino, R., Gherardi, F., 2012. Early signals of new volcanic unrest at Campi Flegrei caldera? Insights from geochemical data and physical simulations. Geology, 40(10), 943-946.

Chiodini, G., Vandemeulebrouck, J., Caliro, S., D'Auria, L., De Martino, P., Mangiacapra, A., Petrillo, Z., 2015. Evidence of thermal-driven processes triggering the 2005–2014 unrest at Campi Flegrei caldera. Earth and Planetary Science Letters, 414, 58-67.

Christenson, B.W., Werner, C.A., Reyes, A.G., Sherburn, S., Scott, B.J., Miller, C., Rosenburg, M.J., Hurst, A.W., Britten, K.A., 2007. Hazards from hydrothermally sealed volcanic conduits. Eos, Transactions American Geophysical Union, 88(5), 53-55.

Christenson, B.W., Reyes, A.G., Young, R., Moebis, A., Sherburn, S., Cole-Baker, J., Britten, K., 2010. Cyclic processes and factors leading to phreatic eruption events: Insights from the 25 September 2007 eruption through Ruapehu Crater Lake, New Zealand. Journal of Volcanology and Geothermal Research, 191(1), 15-32.

Christiansen, R.L. Peterson, D.W., 1981. Chronology of the 1980 eruptive activity. The 1980 Eruptions of Mount St. Helens, Washington 1250, 17-30.

Christoffel, D.A., 1989. Variations in magnetic field intensity at White Island Volcano related to the 1976–82 eruption sequence. In: Houghton, B.F., Nairn, I.A. (1991). The 1976–1982 Strombolian and phreatomagmatic eruptions of White Island, New Zealand: eruptive and depositional mechanisms at a ˈwetˈ volcano. Bulletin of Volcanology, 54(1), 25-49.

Clark, R.H., Otway, P.M., 1982. Deformation monitoring associated with the 1976–82 White Island eruption sequence. In: Houghton, B.F., and Nairn, I.A. (1989). The 1976–82 Eruption Sequence at White Island Volcano (Whakaari), Bay of Plenty, New Zealand, New Zealand Geological Survey Bulletin. 103. New Zealand Geological Survey, Lower Hutt. 69–84.

Clark, R.H., Cole, J.W., 1989. Volcanic monitoring and surveillance at White Island before the 1976–82 eruption sequence. In: Houghton, B.F., Nairn, I.A. (1989). The 1976–82 Eruption Sequence at White Island Volcano (Whakaari), Bay of Plenty, New Zealand. New Zealand Geological Survey Bulletin, 103. New Zealand Geological Survey, Lower Hutt, 13–23.

Cole, J.W., Nairn, I.A., 1975. Catalogue of the active volcanoes and solfatara fields of New Zealand, Part XXII. In: Decker, R.W. (Ed.), Catalogue of the Active Volcanoes of the World Including Solfatara Fields, International Association of Volcanology and Chemistry of the Earth's Interior, Rome, 38–49.

Cole, J.W., Thordarson, T., Burt, R.M., 2000. Magma Origin and Evolution of White Island (Whakaari) Volcano, Bay of Plenty, New Zealand. Journal of Petrology, 41(6), 867-895.

Collar, R.J., Browne, P.R.L. 1985. Hydrothermal eruptions at the Rotokawa geothermal field, Taupo volcanic zone, New Zealand. In Proceedings of the seventh New Zealand geothermal workshop, University of Auckland. Geothermal Institute, Auckland, New Zealand (pp. 6-8).

Costa, A., Dell'Erba, F., t, M.A., Isaia, R., Macedonio, G., Orsi, G., Pfeiffer, T., 2009. Tephra fallout hazard assessment at the Campi Flegrei caldera (Italy): Bulletin of Volcanology, v. 71, p. 259–273.

Cronin, S.J., Neall, V.E., Lecointre, J.A., Hedley, M.J., Loganathan, P., 2003. Environmental hazards of fluoride in volcanic ash: a case study from Ruapehu volcano, New Zealand. Journal of Volcanology and Geothermal Research, 121(3), 271-291.

Curewitz, D., Karson, J.A. 1997. Structural settings of hydrothermal outflow: fracture permeability maintained by fault propagation and interaction. Journal of Volcanology and Geothermal Research, 79(3), 149-168.

Daubrée M 1880a. Examen des poussières volcaniques tombées le 4 janvier 1880 à la Dominique et de l'eau qui les accompagnait. CR Acad Sci Paris 90:624-626.

Daubrée M 1880b. Produits solides et liquides qui continuaient à sortir, en avril 1880, d'un cratère de la Dominique (Antilles anglaises). CR Acad Sci Paris 91:949-950.

De Gennaro, M., Cappelletti, P., Langella, A., Perrotta, A., Scarpati, C., 2000. Genesis of zeolites in the Neapolitan Yellow Tuff: geological, volcanological and mineralogical evidence. Contributions to Mineralogy and Petrology, 139(1), 17-35.

Del Potro, R., Hürlimann, M. 2008. Geotechnical classification and characterization of materials for stability analyses of large volcanic slopes. Engineering Geology, 98(1), 1-17.

Del Potro, R., Hürlimann, M., 2009. The decrease in the shear strength of volcanic materials with argillic hydrothermal alteration, insights from the summit region of Teide stratovolcano, Tenerife. Engineering Geology, 104(1), 135-143.

Del Potro, R., Hürlimann, M. 2010. The origin and geotechnical properties of volcanic soils and their role in developing flank and sector collapses. In Volcanic Rock Mechanics (pp. 159-166). Balkema Leiden, The Netherlands.

Demange, J., Puvilland, P., Iundt, F. 1984. Geothermal feasibility study on Dominica island (Wotten Waven and Soufriere areas) Bureau de Recherches Géologiques et Minères, Institut Mixte de Recherches Geothermiques, Rapport 84 SGN 101 GTH, pp 1-35.

Demange, J., Iundt, F., Puvilland, P. 1985. Geothermal field model of Wotten Waven Island of Dominica Lesser Antilles. Geothermal Resources Council Transactions, 9, 409-415.

De Natale, G., Troise, C., 2011. The 'Campi Flegrei Deep Drilling Project': from risk mitigation to renewable energy production. European Review, 19(03), 337-353.

De Vita, S., Orsi, G., Civetta, L., Carandente, A., D'Antonio, M., Di Cesare, T., Di Vito, M., Fisher, R.V., Isaia, R., Marotta, E., Ort, M., Pappalardo, L., Piochi, M., Southon, J., 1999. The Agnano–Monte Spina eruption (4.1 ka) in the resurgent, nested Campi Flegrei caldera (Italy): Journal of Volcanology and Geothermal Research, v. 91, p. 269–301.

De Vries, B.V.W., Kerle, N., Petley, D. 2000. Sector collapse forming at Casita volcano, Nicaragua. Geology, 28(2), 167-170.

Di Napoli, R., Aiuppa, A., Allard, P. 2014. First multi-gas based characterization of the Boiling Lake volcanic gas (Dominica, Lesser Antilles). Annals of Geophysics, 56(5), S0559.

Di Vito, M.A., Isaia, R., Orsi, G., Southon, J., De Vita, S., d'Antonio, M., Pappalardo, L., Piochi, M., 1999. Volcanism and deformation since 12,000 years at the Campi Flegrei caldera (Italy). Journal of Volcanology and Geothermal Research, 91(2), 221-246.

Di Vito, M.A., Arienzo, I., Braia, G., Civetta, L., D'Antonio, M., Di Renzo, V., Orsi, G., 2011. The Averno 2 fissure eruption: a recent small-size explosive event at the Campi Flegrei Caldera (Italy). Bulletin of volcanology, 73(3), 295-320.

Donnadieu, F., Merle, O., Besson, J. C. 2001. Volcanic edifice stability during cryptodome intrusion. Bulletin of Volcanology, 63(1), 61-72.

Duncan, A.R., 1970. The petrology and petrochemistry of andesite and dacite volcanoes in eastern Bay of Plenty, New Zealand. Ph.D. Thesis, Victoria University of Wellington, New Zealand.

Duzgoren-Aydin, N.S., Aydin, A., Malpas, J. 2002. Re-assessment of chemical weathering indices: case study on pyroclastic rocks of Hong Kong. Engineering Geology, 63(1), 99-119.

D'Auria, L., Giudicepietro, F., Aquino, I., Borriello, G., Del Gaudio, C., Lo Bascio, D., D., Martini, M., Ricciardi, G.P., Ricciolino, P., Ricco, C., 2011. Repeated fluid-transfer episodes as a mechanism for the recent dynamics of Campi Flegrei caldera (1989–2010). Journal of Geophysical Research: Solid Earth (1978–2012), 116(B4).

Edmonds, M., Oppenheimer, C., Pyle, D.M., Herd, R.A., Thompson, G., 2003. SO_2 emissions from Soufriere Hills Volcano and their relationship to conduit permeability, hydrothermal interaction and degassing regime. Journal of Volcanology and Geothermal Research, 124(1), 23-43.

Eldridge 1880. Recent volcanic eruption at the Grand Souffriere, in the island of Dominica. Proceedings of the Royal Geographical Society 2:363-366.

Ellis, A.J., Mahon, W.A.J., 1964. Natural hydrothermal systems and experimental hot-water/rock interactions. Geochimica et Cosmochimica Acta, 28(8), 1323-1357.

Endlich, F.M., 1880. The Island of Dominica. The American Naturalist 14(11):761-772

Farquhar, G., 2001. Guideline for Hand Held Shear Vane Test. New Zealand Geotechnical Society.

Farquharson, J., Heap, M.J., Varley, N.R., Baud, P., Reuschlé, T., 2015. Permeability and porosity relationships of edifice-forming andesites: A combined field and laboratory study. Journal of Volcanology and Geothermal Research, 297, 52-68.

Fedo, C.M., Nesbitt H.W., Young G.M., 1995. Unraveling the effects of potassium metasomatism in sedimentary rocks and paleo sols, with implications for paleo weathering conditions and provenance. Geology. 23, p 921-924

Figueiredo, M.D.A., Augustin, C.H.R.R., Fabris, J. D. 1999. Mineralogy, size, morphology and porosity of aggregates and their relationship with soil susceptibility to water erosion. Hyperfine Interactions, 122(1-2), 177-184.

Fitzgerald, R.H., Tsunematsu, K., Kennedy, B.M., Breard, E.C.P., Lube, G., Wilson, T.M., Jolly, A.D., Pawson, J., Rosenberg, M.D., Cronin, S.J., 2014. The application of a calibrated 3D ballistic trajectory model to ballistic hazard assessments at Upper Te Maari, Tongariro. Journal of Volcanology and Geothermal Research. 286, 248-262.

Folk, R.L. Ward, W.C., 1957. Brazos River bar: a study in the significance of grain size parameters. Journal of Sedimentary Petrology, 27, 3-26.

Foote, L.C., 2012. Experimental modelling of fragmentation processes within phreatic and hydrothermal eruptions.

Foote, L.C., Scheu, B., Kennedy, B., Gravley, D., Dingwell, D.B., 2011. Experimental calibration of phreatic and hydrothermal explosions: a case study on lake Okaro, New Zealand. New Zealand Geothermal workshop 2011 Proceedings.

Fournier, N., Witham, F., Moreau-Fournier, M., Bardou, L., 2009. Boiling Lake of Dominica, West Indies: High-temperature volcanic crater lake dynamics. Journal of Geophysical Research: Solid Earth, 114(B2).

Fournier, N., Chardot, L., 2012. Understanding volcano hydrothermal unrest from geodetic observations: Insights from numerical modeling and application to White Island volcano, New Zealand. Journal of Geophysical Research: Solid Earth (1978–2012), 117(B11).

Fowler, A.C., Scheu, B., Lee, W.T., McGuinness, M.J., 2010. A theoretical model of the explosive fragmentation of vesicular magma. In: Proceedings of the Royal Society A: Mathematical, Physical and Engineering Science, (Vol. 466, No. 2115, pp. 731-752). The Royal Society.

Fullard, L., 2011. Modelling the initiation of a hydrothermal eruption--the shock tube model: a thesis presented in partial fulfilment of the requirements for the degree of Doctor of Philosophy in Mathematics at Massey University, Manawatu Campus, New Zealand (Doctoral dissertation).

Fullard, L.A., Lynch, T.A., 2012. On the initiation of a hydrothermal eruption using the shock-tube model. Transport in porous media, 94(1), 19-46.

Fulignati, P., Gioncada, A., Sbrana, A., 1998. Geologic model of the magmatic hydrothermal system of vulcano (Aeolian Islands, Italy). Mineralogy and Petrology, 62(3-4), 195-222.

Fyfe, W.S., 2012. Fluids In The Earth's Crust: Their Significance In Metamorphic, Tectonic and Chemical Transport Process (Vol. 1). Elsevier.

Giggenbach, W.F., Glasby, G.P., 1977. The influence of thermal activity on the trace metal distribution in marine sediments around White Island, New Zealand. New Zealand Department of Scientific and Industrial Research Bulletin, 218, 121-126.

Giggenbach, W.F., 1987. Redox processes governing the chemistry of fumarolic gas discharges from White Island, New Zealand. Applied Geochemistry, 2(2), 143-161.

Giggenbach, W.F., Shinohara, H., Kusakabe, M., Ohba, T., 2003. Formation of acid volcanic brines through interaction of magmatic gases, seawater and rock within the White Island volcanic-hydrothermal system, New Zealand. Society of Economic Geologists, Special Publication 10, 19-40.

Glasmann, J.R., 1982. Alteration of andesite in wet, unstable soils of Oregon's western Cascades. Clays and Clay Minerals, 30(4), 253-263.

Global Volcanism Program, 2014. Report on White Island (New Zealand). In: Wunderman, R., (ed.), Bulletin of the Global Volcanism Network, 39:2. Smithsonian Institution.

Goff, F. Janik, C.J., 2000. Geothermal systems. Encyclopedia of volcanoes, 817-834.

Graham, I.J., Cole, J.W., 1991. Petrogenesis of andesites and dacites of White Island volcano, Bay of Plenty, New Zealand, in the light of new geochemical and isotopic data. New Zealand Journal of Geology and Geophysics, 34(3), 303-315.

Guidoboni, E., Ciuccarelli, C., 2011. The Campi Flegrei caldera: historical revision and new data on seismic crises, bradyseisms, the Monte Nuovo eruption and ensuing earthquakes (twelfth century 1582 AD). Bulletin of volcanology, 73(6), 655-677.

Handal, S. Barrios, L., 2004. Hydrothermal eruptions in El Salvador. In Rose, W., Bommer, J., Lopez, D., Carr, M., Major, J. (Eds), Natural Hazards in El Salvador, Geological Society of America. Pp 245-256.

Hamilton, W.M., Baumgart, I.L., 1959. White Island, Department of Scientific and Industrial Research Bulletin. 127, 9–24.

Hardy, L., 2005. Lake Okaro: Explosions and Erosion. BSc (Hons) Thesis, The University of Otago.

Harnois, I., 1988. The CIW index. Sedimentary Geology 55, 319–322.

Harnois, L., Moore, J.M., 1988. Geochemistry and origin of the Ore Chimney Formation, a transported paleo regolith in the Grenville Province of southeastern Ontario, Canada. Chemical Geology, 69(3), 267-289.

Harris, A.J.L., Maciejewski, A.J.H., 2000. Thermal surveys of the Vulcano Fossa fumarole field 1994–1999: evidence for fumarole migration and sealing. Journal of Volcanology and Geothermal Research, 102(1), 119-147.

Heap, M.J., Lavallée, Y., Laumann, A., Hess, K.U., Meredith, P.G., Dingwell, D.B., 2012. How tough is tuff in the event of fire?, Geology, 40(4), 311-314.

Heap, M.J., Lavallée, Y., Petrakova, L., Baud, P., Reuschlé, T., Varley, N.R., Dingwell, D.B., 2014. Microstructural controls on the physical and mechanical properties of edifice-forming andesites at Volcán de Colima, Mexico, Journal of Geophysical Research: Solid Earth, 119.

Heap, M.J., Kennedy, B.M., Pernin, N., Jacquemard, L., Baud, P., Farquharson, J.I., Scheu, B., Lavallée, Y., Gilg, H.A., Letham-Brake, M., Mayer, K., Jolly, A.D., Reuschlé, T., Dingwell, D.B., 2015. Mechanical behaviour and failure modes in the Whakaari (White Island volcano) hydrothermal system, New Zealand. Journal of Volcanology and Geothermal Research, 295, 26-42.

Hedenquist, J.W., Henley, R.W., 1985. Hydrothermal eruptions in the Waiotapu geothermal system, New Zealand; their origin, associated breccias, and relation to precious metal mineralization. Economic Geology, 80(6), 1640-1668.

Hedenquist, J.W., Lowenstern, J.B., 1994. The role of magmas in the formation of hydrothermal ore deposits. Nature, 370 (6490), 519-527.

Hedenquist, J.W., Arribas, A., Gonzalez-Urien, E., 2000. Exploration for epithermal gold deposits. Reviews in Economic Geology, 13, 245-277.

Henderson, J.H., Jackson, M.L., Syers, J.K., Clayton, R.N., Rex, R.W., 1971. Cristobalite authigenic origin in relation to montmorillonite and quartz origin in bentonites. Clays and Clay Minerals, 19(4), 229-238.

Herlihy, R.D., Smith, A.L., Rheubottom, A.N., Kirkley, J., Melchiorre, E., Fryxell, J.E., Roobol, M.J., 2005. Geology and geochemistry of volcanic hot springs on the island of Dominica, West Indies. In AGU Fall Meeting Abstracts.

Horwell, C.J., 2007. Grain-size analysis of volcanic ash for the rapid assessment of respiratory health hazard. Journal of Environmental Monitoring, 9(10), 1107-1115.

Horwell, C.J., Baxter, P.J., 2006. The respiratory health hazards of volcanic ash: a review for volcanic risk mitigation. Bulletin of Volcanology, 69, 1-24.

Horwell, C.J., Williamson, B.J., Llewellin, E.W., Damby, D.E., Le Blond, J.S., 2013. The nature and formation of cristobalite at the Soufrière Hills volcano, Montserrat: implications for the petrology and stability of silicic lava domes. Bulletin of Volcanology, 75(3), 1-19.

Houghton, B.F., Nairn, I.A., 1989a. A model for the 1976–82 phreatomagmatic and Strombolian eruption sequence at White Island volcano. New Zealand Geological Survey Bulletin 103, 127–136.

Houghton, B.F., Nairn, I.A., 1989b. The phreatomagmatic and strombolian eruption events at White Island volcano 1976–82: eruption narrative. In: Houghton, B.F., and Nairn, I.A., 1989. The 1976–82 Eruption Sequence at White Island Volcano (Whakaari), Bay of Plenty, New Zealand. New Zealand Geological Survey Bulletin, 103. New Zealand Geological Survey, Lower Hutt, 13–23.

Houghton, B.F., and Nairn, I.A., 1991. The 1976–1982 Strombolian and phreatomagmatic eruptions of White Island, New Zealand: eruptive and depositional mechanisms at a 'wet' volcano. Bulletin of Volcanology. 54, 25–49.

Höller, H., 1967. Experimentelle Bildung von Alunit-Jarosit durch die Einwirkung von Schwefelsäure auf Mineralien und Gesteine. Contributions to Mineralogy and Petrology, 15(4), 309-329.

Hurst, A.W., Rickerby, P.C., Scott, B.J., Hashimoto, T., 2004. Magnetic field changes on White Island, New Zealand, and the value of magnetic changes for eruption forecasting. Journal of Volcanology and Geothermal Research, 136(1), 53-70.

Hurst, T., Jolly, A.D., Sherburn, S., 2014. Precursory characteristics of the seismicity before the 6 August 2012 eruption of Tongariro volcano, North Island, New Zealand. Journal of Volcanology and Geothermal Research 286, 294–302.

Hürlimann, M., Ledesma, A., Martı, J. 2001. Characterization of a volcanic residual soil and its implications for large landslide phenomena: application to Tenerife, Canary Islands. Engineering Geology, 59(1), 115-132.

Isaia, R., Marianelli, P., Sbrana, A., 2009. Caldera unrest prior to intense volcanism in Campi Flegrei (Italy) at 4.0 ka BP: implications for caldera dynamics and future eruptive scenarios. Geophysical Research Letters, 36(21).

Isaia, R., Vitale, S., Di Giuseppe, M.G., Iannuzzi, E., Tramparulo, F.D.A., Troiano, A., 2015. Stratigraphy, structure, and volcano-tectonic evolution of Solfatara maar-diatreme (Campi Flegrei, Italy). Geological Society of America Bulletin, B31183-1.

Italiano, F., Nuccio, P.M., Valenza, M., 1984. Geothermal energy release at the Solfatara of Pozzuoli (Phlegraean Fields): phreatic and phreatomagmatic explosion risk implications. Bulletin volcanologique, 47(2), 275-285.

James, A., 1997. Observations made in the Valley of Desolation following a volcanic eruption, July 1997. Unpublished report, Forestry and Wildlife Division, Dominica.

John, D.A., Sisson, T.W., Breit, G.N., Rye, R.O., Vallance, J.W., 2008. Characteristics, extent and origin of hydrothermal alteration at Mount Rainier Volcano, Cascades Arc, USA: Implications for debris-flow hazards and mineral deposits. Journal of Volcanology and Geothermal Research, 175(3), 289-314.

Joseph, E.P., Fournier, N., Lindsay, J.M., Fischer, T.P., 2011. Gas and water geochemistry of geothermal systems in Dominica, Lesser Antilles island arc. Journal of Volcanology and Geothermal Research, 206(1), 1-14.

Jolly, A.D., Chardot, L., Neuberg, J., Fournier, N., Scott, B.J., Sherburn, S., 2012. High impact mass drops from helicopter: A new active seismic source method applied in an active volcanic setting. Geophysical Research Letters, 39(12), 1-5.

Kato, A., Terakawa, T., Yamanaka, Y., Maeda, Y., Horikawa, S., Matsuhiro, K., Okuda, T., 2015. Preparatory and precursory processes leading up to the 2014 phreatic eruption of Mount Ontake, Japan. Earth Planets Space67, 111.

Kennedy, B., Spieler, O., Scheu, B., Kueppers, U., Taddeucci, J., Dingwell, D.B., 2005. Conduit implosion during Vulcanian eruptions. Geology, 33(7), 581-584.

Kieffer, S.W., Sturtevant, B., 1984. Laboratory studies of volcanic jets. Journal of Geophysical Research: Solid Earth, 89(B10), 8253-8268.

Kilgour, G., Manville, V., Della Pasqua, F., Graettinger, A., Hodgson, K.A., Jolly, G.E., 2010. The 25 September 2007 eruption of Mount Ruapehu, New Zealand: directed ballistics, surtseyan jets, and ice-slurry lahars. Journal of Volcanology and Geothermal Research, 191(1), 1-14.

Komorowski, J.C., Hammouya, G., 1998. Analytical results and report on the current activity of the Soufrière area as of December 8-9 1998. Unpublished report presented to the Government of Dominica.

Koyaguchi, T., Scheu, B., Mitani, N. K., Melnik, O., 2008. A fragmentation criterion for highly viscous bubbly magmas estimated from shock tube experiments. Journal of Volcanology and Geothermal Research, 178(1), 58-71.

Kueppers, U., Scheu, B., Spieler, O., Dingwell, D.B., 2006. Fragmentation efficiency of explosive volcanic eruptions: a study of experimentally generated pyroclasts. Journal of Volcanology and Geothermal Research, 153(1), 125-135.

Ladygin, V.M., Frolova, Y.V., Rychagov, S.N., 2014. The alteration of effusive rocks due to acidic leaching by shallow thermal waters: The Baranskii geothermal system, Iturup Island. Journal of Volcanology and Seismology, 8(1), 17-33.

Letham-Brake, M., 2013. Geological constraints on fluid flow at Whakaari volcano (White Island). M.Sc. Thesis, Department of Geological Sciences, University of Canterbury, Christchurch, New Zealand.

Lindsay, J.M., Stasiuk, M.V., Shepherd, J.B., 2003. Geological history and potential hazards of the late-Pleistocene to Recent Plat Pays volcanic complex, Dominica, Lesser Antilles. Bulletin of Volcanology, 65(2-3), 201-220.

Lindsay, J.M., Smith, A.L., Roobol, M.J., Stasiuk, M.V., 2005. Dominica. In: Lindsay, J.M., Robertson, R.E.A., Shepherd, J.B., Ali, S. (Eds.), Volcanic Hazard Atlas of the Lesser Antilles-Seismic Research Unit. The University of the West Indies, Trinidad and Tobago, W.I, pp. 1-48.

Lynne, B.Y., Campbell, K.A., Moore, J.N., Browne, P.R.L., 2005. Diagenesis of 1900-year-old siliceous sinter (opal-A to quartz) at Opal Mound, Roosevelt Hot Springs, Utah, USA. Sedimentary Geology, 179(3), 249-278.

Makó, A., Elek, B., Dunai, A., Hernadi, H., 2009. Comparison of nonaqueous phase liquids' conductivity and air permeability of different soils. Communications in soil science and plant analysis, 40(1-6), 787-799.

Mangiacapra, A., Moretti, R., Rutherford, M., Civetta, L., Orsi, G., Papale, P., 2008. The deep magmatic system of the Campi Flegrei caldera (Italy). Geophysical Research Letters, 35(21).

Martel, C., Dingwell, D.B., Spieler, O., Pichavant, M., Wilke, M., 2000. Fragmentation of foamed silicic melts: an experimental study. Earth and Planetary Science Letters, 178(1), 47-58.

Mastin, L.G., 1995. Thermodynamics of gas and steam-blast eruptions. Bulletin of Volcanology, 57(2), 85-98.

Mastin, L.G., 2001. A simple calculator of ballistic trajectories for blocks ejected during volcanic eruptions: U.S. Geological Survey Open-File Report 01-45, 16p.

Mayer, K., Scheu, B., Gilg, H.A., Heap, M.J., Kennedy, B.M., Lavallée, Y., Letham-Brake, M., Dingwell, D.B., 2015. Experimental constraints on phreatic eruption processes at Whakaari (White Island volcano). Journal of Volcanology and Geothermal Research, 302, 150-162.

Montanaro, C., Scheu, B., Gudmundsson, M.T., Vogfjörd, K., Reynolds, H.I., Dürig, T., Strehlow, K., Rott, S., Reuschlé, T., Dingwell, D.B., 2016. Multidisciplinary constraints of hydrothermal explosions based on the 2013 Gengissig lake events, Kverkfjöll volcano, Iceland. Earth and Planetary Science Letters, 434, 308-319.

Moon, V., Bradshaw, J., Smith, R., de Lange, W., 2005. Geotechnical characterization of stratocone crater wall sequences, White Island Volcano, New Zealand. Engineering Geology, 81(2), 146-178.

Moon, V., Bradshaw, J., de Lange, W., 2009. Geomorphic development of White Island Volcano based on slope stability modelling. Engineering Geology, 104(1), 16-30.

Moretti, R., Arienzo, I., Civetta, L., Orsi, G., Papale, P., 2013. Multiple magma degassing sources at an explosive volcano. Earth and Planetary Science Letters, 367, 95-104.

Morgan, L.A., Shanks, W.P., Pierce, K.L., 2009. Hydrothermal processes above the Yellowstone magma chamber: Large hydrothermal systems and large hydrothermal explosions. Geological Society of America Special Papers, 459, 1-95.

Mormone, A., Tramelli, A., Di Vito, M.A., Piochi, M., Troise, C., De Natale, G., 2011. Secondary hydrothermal minerals in buried rocks at the Campi Flegrei caldera, Italy: a possible tool to understand the rock-physics and to assess the state of the volcanic system. Periodico di Mineralogia Vol. 80, 3 (Special Issue), 385-406.

Mormone, A., Troise, C., Piochi, M., Balassone, G., Joachimski, M., De Natale, G., 2015. Mineralogical, geochemical and isotopic features of tuffs from the CFDDP drill hole: Hydrothermal activity in the eastern side of the Campi Flegrei volcano (southern Italy). Journal of Volcanology and Geothermal Research, 290, 39-52.

Mueller, S., Melnik, O., Spieler, O., Scheu, B., Dingwell, D.B., 2005. Permeability and degassing of dome lavas undergoing rapid decompression: an experimental determination. Bulletin of Volcanology, 67(6), 526-538.

Mueller, S., Scheu, B., Spieler, O., Dingwell, D.B., 2008. Permeability control on magma fragmentation. Geology, 36(5), 399-402.

Mutlu, H., Sariiz, K., Kadir, S., 2005. Geochemistry and origin of the Şaphane alunite deposit, Western Anatolia, Turkey. Ore Geology Reviews, 26(1), 39-50.

Nairn, I., Hedenquist, J., Villamor, P., Berryman, K., Shane, P., 2004. The ~AD1315 Tarawera and Waiotapu eruptions, New Zealand: contemporaneous rhyolite and hydrothermal eruptions driven by an arrested basalt dyke system? Bulletin of Volcanology, 67: 186-193.

Nelson, C.E., Giles, D.L., 1985. Hydrothermal eruption mechanisms and hot spring gold deposits. Economic Geology, 80(6), 1633-1639.

Nesbitt, H.W., Young, G.M., 1982. Early Proterozoic climates and plate motions inferred from major element chemistry of lutites. Nature. 299, p. 715–717.

Nicholls, H.A.A., 1880a. The volcanic eruption in Dominica. Nature 21:372-373.

Nicholls, H.A.A., 1880b. Visit to the scene of the late volcanic eruption. The Dominican, January 17, 1880.

Nicholls, H.A.A., Watt, E., 1880. Dominica and it's Boiling Lake. The Dominican.

Nishi, Y., Sherburn, S., Scott, B.J., Sugihara, M., 1996. High-frequency earthquakes at White Island volcano, New Zealand: insights into the shallow structure of a volcano-hydrothermal system. Journal of Volcanology and Geothermal Research, 72(3), 183-197.

Orsi, G., De Vita, S., Di Vito, M., 1996. The restless, resurgent Campi Flegrei nested caldera (Italy): constraints on its evolution and configuration. Journal of Volcanology and Geothermal Research, 74(3), 179-214.

Orsi, G., Civetta, L., Del Gaudio, C., De Vita, S., Di Vito, M.A., Isaia, R., Petrazzuoli, S., Ricciardi, G.P., Ricco, C., 1999. Short-term ground deformations and seismicity in the nested Campi Flegrei caldera (Italy): Journal of Volcanology and Geothermal Research, v. 91, p. 415–451.

Orsi, G., Di Vito, M.A., Isaia, R., 2004. Volcanic hazard assessment at the restless Campi Flegrei caldera. Bulletin of Volcanology, 66(6), 514-530.

Peltier, A., Scott, B., Hurst, T., 2009. Ground deformation patterns at White Island volcano (New Zealand) between 1967 and 2008 deduced from levelling data. Journal of Volcanology and Geothermal Research, 181(3), 207-218.

Piochi, M., Mormone, A., Balassone, G., Strauss, H., Troise, C., De Natale, G., 2015. Native sulfur, sulfates and sulfides from the active Campi Flegrei volcano (southern Italy): Genetic environments and degassing dynamics revealed by mineralogy and isotope geochemistry. Journal of Volcanology and Geothermal Research, 304, 180-193.

Pirajno F., 2009. Hydrothermal Processes and Mineral Systems. Springer Netherlands, 1250 pages.

Pola, A., 2011. Physical and mechanical characterization of altered volcanic rocks for the stability of volcanic edifices (Doctoral dissertation, Ph. D Thesis, University of Milano—Bicocca, Milano).

Pola, A., Crosta, G., Fusi, N., Barberini, V., Norini, G., 2012. Influence of alteration on physical properties of volcanic rocks. Tectonophysics, 566, 67-86.

Pola, A., Crosta, G.B., Fusi, N., Castellanza, R., 2013. General characterization of the mechanical behavior of different volcanic rocks with respect to alteration. Engineering Geology 169, 1–13.

Possemiers, M., Huysmans, M., Peeters, L., Batelaan, O., Dassargues, A., 2012. Relationship between sedimentary features and permeability at different scales in the Brussels Sands. Geologica Belgica, 15(3).

Putz, H., Brandenburg, K., 2003. Match! Phase identification from powder diffraction. Crystal Impact. Bonn, Germany.

Rager, A.H., Smith, E.I., Scheu, B., Dingwell, D.B., 2013. The effects of water vaporization on rock fragmentation during rapid decompression: Implications for the formation of fluidized ejecta on Mars. Earth and Planetary Science Letters 385, 68–78.

Rao, S. M., 1996. Role of apparent cohesion in the stability of Dominician allophane soil slopes. Engineering Geology, 43(4), 265-279.

Richard, D., Scheu, B., Mueller, S.P., Spieler, O., Dingwell, D.B., 2013. Outgassing: Influence on speed of magma fragmentation. Journal of Geophysical Research: Solid Earth, 118(3), 862-877.

Robb, L., 2005. Introduction to ore-forming processes. Blackwell Publishing, Oxford.

Rodgers, K.A., Browne, P.R.L., Buddle, T.F., Cook, K.L., Greatrex, R.A., Hampton, W.A., Herdianita, N.R., Holland, G.R., Lynne, B.Y., Martin, R., Newton, Z., Pastars, D., Sannazzaro, K.L., and Teece, C.I.A., 2004. Silica phases in sinters and residues from geothermal fields of New Zealand. Earth-Science Reviews, 66(1), 1-61.

Roobol, M.J., Smith, A.L., 2004. Geological map of Dominica, West Indies. Geology Department, University of Puerto Rico at Mayaquez.

Rouse, W.C., Reading, A.J., Walsh, R.P.D., 1986. Volcanic soil properties in Dominica, West Indies. Engineering Geology, 23(1), 1-28.

Rouwet, D., Morrissey, M.M., 2015. Mechanisms of crater lake breaching eruptions. In Volcanic Lakes (pp. 73-91). Springer Berlin Heidelberg.

Ruxton B.P., 1968. Measures of the degree of chemical weathering of rocks. Journal of Geology, 76, p. 518-527.

Rye, R.O., 2005. A review of the stable-isotope geochemistry of sulfate minerals in selected igneous environments and related hydrothermal systems. Chemical Geology, 215(1), 5-36.

Rye, R.O., Bethke, P.M., Wasserman, M.D., 1992. The stable isotope geochemistry of acid sulfate alteration. Economic Geology, 87(2), 225-262.

Rye, R.O., Breit, G.N., Zimbelman, D.R., 2003. Preliminary mineralogic and stable isotope studies of altered summit and flank rocks and Osceola Mudflow deposits on Mount Rainier, Washington. US Department of the Interior, US Geological Survey.

Sapper, K., 1903. Ein Besuch von Dominica. Zentralblatt für Mineralogie, Geologie und Paleontolgie, 305-314.

Scher, S., Williams-Jones, A.E., Williams-Jones, G., 2013. Fumarolic activity, acid-sulfate alteration, and high sulfidation epithermal precious metal mineralization in the crater of Kawah Ijen volcano, Java, Indonesia. Economic Geology, 108(5), 1099-1118.

Scheu, B., Spieler, O., Dingwell, D.B., 2006. Dynamics of explosive volcanism at Unzen volcano: an experimental contribution. Bulletin of Volcanology, 69(2), 175-187.

Scheu, B., Kueppers, U., Mueller, S., Spieler, O., Dingwell, D.B., 2008. Experimental volcanology on eruptive products of Unzen volcano. Journal of Volcanology and Geothermal Research, 175(1), 110-119.

Scheu, B., Serr, F., Dingwell, D.B., 2011. Phreatic and hydrothermal explosions – A lab approach. Geophysical Research Abstracts, Vol. 13, EGU2011-1669.

Seki, K., Kanda, W., Ogawa, Y., Tanbo, T., Kobayashi, T., Hino, Y., 2015. Imaging the hydrothermal system beneath the Jigokudani valley, Tateyama volcano, Japan: implications for structures controlling repeated phreatic eruptions from an audio-frequency magnetotelluric survey. Earth Planets Space 67, 6.

Sherburn, S., Scott, B.J., Nishi, Y., Sugihara, M., 1998. Seismicity at White Island volcano, New Zealand: a revised classification and inferences about source mechanism. Journal of Volcanology and Geothermal Research, 83(3), 287-312.

Simkin, T., Siebert, L., 1994. Volcanoes of the World: A Regional Directory, Gazetteer, and Chronology of Volcanism During the Last 10,000 Years, Geoscience, Press, Inc. (Tucson, Arizona), in association with the Smithsonian Institute, 349 pages.

Smith, T., 2000. Mathematical modelling of underground flow processes in hydrothermal eruptions. Unpublished PhD thesis, Massey University, Manawatu, New Zealand.

Smith, T., McKibbin, R., 2000. An investigation of boiling processes in hydrothermal eruptions. In Proceeding world geothermal congress (pp. 699-704).

Smith, A.L., Roobol, M.J., Mattioli, G.S., Fryxell, J.E., Daly, G.E., Fernandez, L A., 2013. The volcanic geology of the mid-arc Island of Dominica (Vol. 496). Geological Society of America.

Smith, V.C., Isaia, R., Pearce, N.J.G., 2011. Tephrostratigraphy and glass compositions of post-15 kyr Campi Flegrei eruptions: Implications for eruption history and chronostratigraphic markers: Quaternary Science Reviews, v. 30, p. 3638–3660.

Sneed, E.D., Folk, R.L., 1958. Pebbles in the lower Colorado River, Texas a study in particle morphogenesis. Journal of Geology, 66, 114-150.

Spieler, O., Alidibirov, M., Dingwell, D.B., 2003. Grain-size characteristics of experimental pyroclasts of 1980 Mount St. Helens cryptodome dacite: effects of pressure drop and temperature. Bulletin of Volcanology, 65(2-3), 90-104.

Spieler, O., Kennedy, B., Kueppers, U., Dingwell, D. B., Scheu, B., Taddeucci, J., 2004. The fragmentation threshold of pyroclastic rocks. Earth and Planetary Science Letters, 226(1), 139-148.

Steven, T.A., Ratté, J.C., 1960. Geology and ore deposits of the Summitville district, San Juan Mountains, Colorado (No. 343). US Government. Print. Off.

Stoffregen, R., 1987. Genesis of acid-sulphate alteration and Au-Cu-Ag mineralization at Summitville, Colorado. Economic Geology 82:1575-1591.

Thiery, R., Mercury, L., 2009. Explosive properties of water in volcanic and hydrothermal systems. Journal of Geophysical Research: Solid Earth, 114(B5).

Traineau, H., Lasne, E., Coppo, N., Baltassa, J.M., 2015. Recent Geological, Geochemical and Geophysical Surveys of the Roseau Valley, High-Temperature Geothermal Field in Dominica, West Indies. Proceedings World Geothermal Congress 2015 Melbourne, Australia, 19-25 April 2015.

Troiano, A., Di Giuseppe, M.G., Patella, D., Troise, C., De Natale, G., 2014. Electromagnetic outline of the Solfatara–Pisciarelli hydrothermal system, Campi Flegrei (Southern Italy). Journal of Volcanology and Geothermal Research, 277, 9-21.

Valentino, G.M., Cortecci, G., Franco, E., Stanzione, D., 1999. Chemical and isotopic compositions of minerals and waters from the Campi Flegrei volcanic system, Naples, Italy. Journal of Volcanology and Geothermal Research, 91(2), 329-344.

Vanorio, T., Kanitpanyacharoen, W., 2015. Rock physics of fibrous rocks akin to Roman concrete explains uplifts at Campi Flegrei Caldera. Science, 349(6248), 617-621.

Vignaroli, G., Aldega, L., Balsamo, F., Billi, A., De Benedetti, A.A., De Filippis, L. Giordano, G., Rossetti, F., 2015. A way to hydrothermal paroxysm, Colli Albani volcano, Italy. Geological Society of America Bulletin, B31139-1.

Vikre, P.G., Henry, C.D., 2011. Quartz-alunite alteration cells in the ancestral southern Cascade magmatic arc. In Great Basin Evolution and Metallogeny, Proceedings, Geological Society of Nevada, 2010 Symposium Reno, Nevada (pp. 701-745).

Vilardo, G., Isaia, R., Ventura, G., De Martino, P., Terranova, C., 2010. InSAR Permanent Scatterer analysis reveals fault reactivation during inflation and deflation episodes at Campi Flegrei caldera: Remote Sensing of Environment, v. 114, p. 2373–2383.

Wadge, G., 1984. Comparison of volcanic production rates and subduction rates in the Lesser Antilles and Central America. Geology, 12(9), 555-558.

Wadsworth, M.E., 1880. The volcanic dust from Dominica. Nature, July 22 1880, pp 266-267.

Watt, E., 1880. The Recent Volcanic Eruption in Dominica. Nature, 22, 77.

Waythomas, C.F., 2012. Landslides: Landslides at stratovolcanoes initiated by volcanic unrest. In: Clague, J.J., Stead, D., 2012. Landslides: types, mechanisms and modeling. Cambridge University Press.

Werner, C., Hurst, T., Scott, B., Sherburn, S., Christenson, B.W., Britten, K., Cole-Baker, J., Mullan, B., 2008. Variability of passive gas emissions, seismicity, and deformation during crater lake growth at White Island Volcano, New Zealand, 2002–2006. Journal of Geophysical Research: Solid Earth (1978–2012), 113(B1).

White, N.C., Hedenquist, J.W., 1995. Epithermal gold deposits: styles, characteristics and exploration. SEG newsletter, 23(1), 9-13.

Williams-Jones, A.E., Heinrich, C.A., 2005, Vapor transport of metals and the formation of magmatic-hydrothermal ore deposits. Economic Geology, V. 100, p. 1287–1312.

Wohletz, K.H., 1983. Mechanisms of hydrovolcanic pyroclast formation: grain-size, scanning electron microscopy, and experimental studies. Journal of Volcanology and Geothermal Research, 17(1), 31-63.

Wohletz, K., Heiken, G., 1992. Volcanology and geothermal energy (p. 432). Berkeley: University of California Press.

Wood, C.P., Browne, P.R.L., 1996. Chlorine-rich pyrometamorphic magma at White Island volcano, New Zealand. Journal of volcanology and geothermal research, 72(1), 21-35.

Wyering, L.D., Villeneuve, M.C., Wallis, I.C., Siratovich, P.A., Kennedy, B.M., Gravley, D.M., Cant, J.L., 2014. Mechanical and physical properties of hydrothermally altered rocks, Taupo Volcanic Zone, New Zealand. Journal of Volcanology and Geothermal Research, 288, 76-93.

Zimanowski, B., Fröhlich, G., Lorenz, V., 1991. Quantitative experiments on phreatomagmatic explosions. Journal of Volcanology and Geothermal Research, 48(3), 341-358.

Zimbelman, D.R., Rye, R.O., Breit, G.N., 2005. Origin of secondary sulfate minerals on active andesitic stratovolcanoes. Chemical Geology, 215(1), 37-60.

Zimbone, S.M., Vickers, A., Morgan, R.P.C., Vella, P., 1996. Field investigations of different techniques for measuring surface soil shear strength. Soil Technology, 9(1), 101-111.

Further reading:

Smithsonian Institution, 2013.White Island. Volcanoes of the World 4.0: The volcano and eruption database of Smithsonian's Global Volcanism Program Retrieved 2 Oct. 2013 from: http://www.volcano.si.edu/volcano.cfm?vn=241040.

Umwelt-Geräte-Technik, 2012. PL-300 User's manual. Version18.03.2014. Müncheberg. www.ugt-online.de/fileadmin/media/products/01%20bodenkunde/downloads/PL-300/PL_300_en_Ver02.pdf

Appendix A1

Volcanological history of Whakaari (White Island volcano). Events and periods of activity used in Figure 3.2, modified after Letham-Brake, 2013.

Date	Type of activity	Erupted Volume (m3)	References
1. Dec. 1826	Phreatic tephra eruption	5.0x106	Williams, 1826; cited in Hamilton and Baumgart, 1959; Smithsonian Institution, 2013
1836 (± 2 y)	Phreatom. tephra eruption	5.0x106	Polack, 1838; cited in Hamilton and Baumgart, 1959; Smithsonian Institution, 2013
Oct. 1885	Phreatic tephra eruption	5.0x106	NZ Herald, 1885; cited in Hamilton and Baumgart, 1959; Smithsonian Institution, 2013
16. Sep. - Dec. 1886	Phreatom. tephra eruption	5.0x106	Smith, 1887; cited in Hamilton and Baumgart, 1959; Smithsonian Institution, 2013
13. May 1909	Phreatic tephra eruption	5.0x106	NZ Herald, 1909; cited in Hamilton and Baumgart, 1959; Smithsonian Institution, 2013
Dec. 1922	Phreatic tephra eruption	5.0x106	Evening Post, 1923;cited in Hamilton and Baumgart, 1959; Smithsonian Institution, 2013
Sep. 1924	Phreatic tephra eruption	5.0x106	Evening Post, 1924; cited in Hamilton and Baumgart, 1959; Smithsonian Institution, 2013
3. Feb. 1926	Phreatic tephra eruption	5.0x106	Grange, 1927; cited in Hamilton and Baumgart, 1959; Smithsonian Institution, 2013

Appendix A2

Volcanological history of Whakaari (White Island volcano). Events and periods of activity used in Figure 3.2, modified after Letham-Brake, 2013.

Date	Type of activity	Erupted Volume (m3)	References
1. - 3. Sep. 1928	Phreatic tephra eruption	5.0x105	NZ Herald, 1928; cited in Hamilton and Baum gart,1 959; Smithsonian Institution, 2013
2. Apr. 1933	Phreatic tephra eruption	5.0x107	Goosman, 1933; cited in Hamilton and Baumgart, 1959; Smithsonian Institution, 2013
before Jan. 1947	Phreatic tephra eruption	5.0x106	Cole and Nairn, 1975; Smithsonian Institution, 2013
Jan. 1955	Phreatic tephra eruption	5.0x106	Cole and Nairn, 1975; Smithsonian Institution, 2013
11. Dec. 1957	Phreatic tephra eruption	5.0x106	Cole and Nairn, 1975; Smithsonian Institution, 2013
Dec. 1958	Phreatic tephra eruption	5.0x105	Cole and Nairn, 1975; Smithsonian Institution, 2013
14.- 20. Dec. 1959	Phreatic tephra eruption	5.0x106	Cole and Nairn, 1975; Smithsonian Institution, 2013
15. Dec. 1962	Phreatic tephra eruption	5.0x107	Cole and Nairn, 1975; Smithsonian Institution, 2013
13. Nov. 1966 - Mar. 1967	Phreatic tephra eruption	5.0x107	Cole and Nairn, 1975; Smithsonian Institution, 2013
27. Jan. 1968 - Feb. 1969	Phreatic tephra eruption	5.0x107	Cole and Nairn , 1975; Smithsonian Institution, 2013
Aug. - Sep. 1969	Phreatic tephra eruption	5.0x106	Cole and Nairn, 1975; Smithsonian Institution, 2013
30. Jun. 1970 (±30 d)	Phreatic tephra eruption	5.0x106	Cole and Nairn, 1975; Smithsonian Institution, 2013

Appendix A3

Volcanological history of Whakaari (White Island volcano). Events and periods of activity used in Figure 3.2, modified after Letham-Brake, 2013.

| Date	Type of activity	Erupted Volume (m3)	References
9. Apr. 1971 (± 3 d)	Phreatic tephra eruption	5.0x106	Cole and Nairn, 1975; Smithsonian Institution, 2013
19.- 20. Jul. 1971	Phreatic tephra eruption	5.0x106	Cole and Nairn, 1975; Smithsonian Institution, 2013
8. Sep. 1974 (± 10 d)	Phreatic tephra eruption	5.0x106	Clark and Cole, 1976 cited in Clark and Cole, 1989; Smithsonian Institution, 2013
18. Dec. 1976 - 29 Jan. 1982	Phreatic, phreatom. and strombolian tephra eruption	5.0x107	Houghton and Nairn, 1989a; Houghton and Nairn,1991; Smithsonian Institution, 2013
26. Dec. 1983 - 12. Feb. 1984	Phreatic tephra eruption	5.0x106	Houghton and Nairn, 1989a; Houghton and Nairn,1991; Smithsonian Institution, 2013
1. Feb. 1986 - 28. Jul.1994	Phreatic and phreatom. tephra eruption	5.0x107	Smithsonian Institution, 2013
28.- 29. J un. 1995	Phreatic tephra eruption	5.0x105	Smithsonian Institution, 2013
28.- 29. Mar. 1998	Phreatic tephra eruption	5.0x105	Smithsonian Institution, 2013
22. Aug. 1998 - Aug. 1999	Phreatom. tephra eruption	5.0x106	Smithsonian Institution, 2013

Appendix A4

Volcanological history of Whakaari (White Island volcano). Events and periods of activity used in Figure 3.2, modified after Letham-Brake, 2013.

Date	Type of activity	Erupted Volume (m3)	References
7. Mar. 2000 - 5 Sep. 2000	Phreatom. tephra eruption	$5.0x10^7$	Smithsonian Institution, 2013
19. Feb . 2001	Phreatic tephra eruption	$5.0x10^6$	Global Volcanism Program 2014; Smithsonian Institution, 2013
5. Aug. 2012 – 2013	Phreatic and phreatom. tuff-cone forming tephra and magmatic dome-forming eruption	$5.0x10^5$	Global Volcanism Program 2014

Appendix B

Bulk X-ray diffractograms of investigated samples from Solfatara crater (S1-S3) and Pisciarelli fumarole (P1-P3).
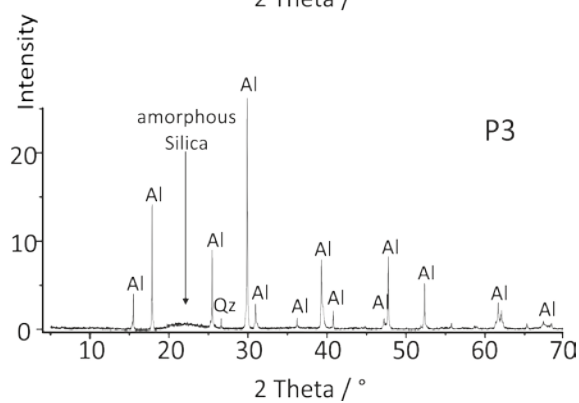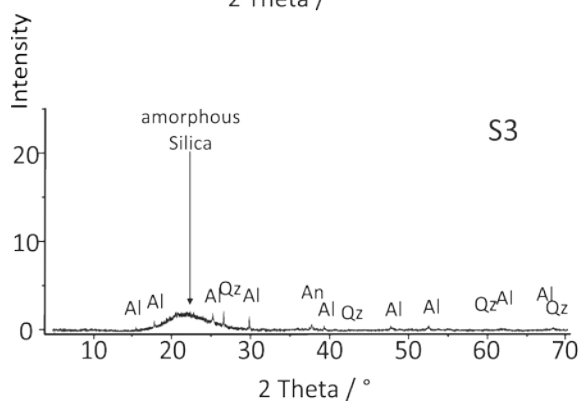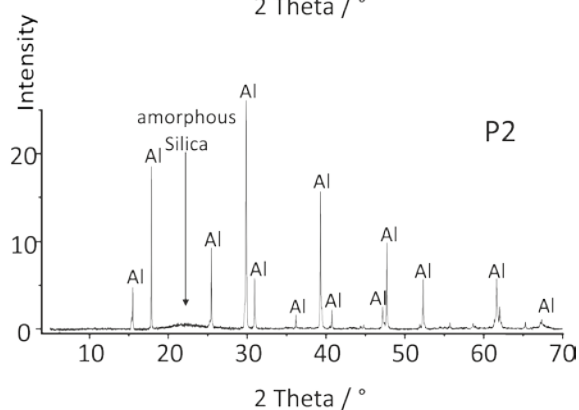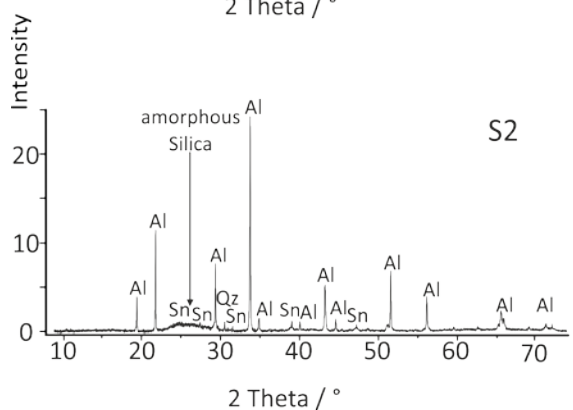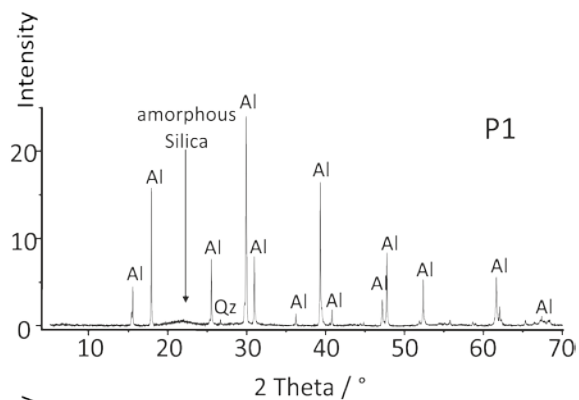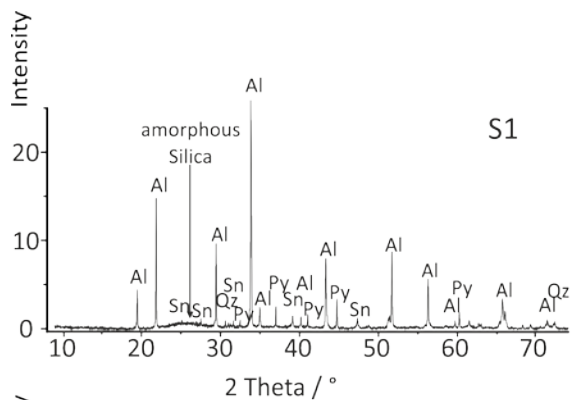
CURRICULUM VITAE

Klaus Mayer

PhD student in Experimental Volcanology

Ludwig-Maximilians-Universität
Dept. für Geo- u. Umweltwissenschaften
Theresienstr. 41 / III, D-80 333 München
+49 (0)89 2180 4272
+40 (0)176 38576842
klaus.mayer@min.uni-muenchen.de

Born February 29, 1984
German citizenship

Education	
Since 2012	PhD candidate, Ludwig-Maximilians-Universität (LMU) Munich, Germany PhD thesis : Phreatic eruptions and the influence of hydrothermal alteration on the processes Supervised by PD Dr. Bettina Scheu & Prof. Dr. Donald B. Dingwell
2005 – 2011	Diploma degree Hydrogeology, Technische Universität München (TUM) Munich, Germany Diploma thesis: Zur Hydrogeologie des Doggersandsteins in der Mittleren Frankenalb Supervised by Dr. Thomas Baumann (TUM) Diploma mapping: Geologische Kartierung in der Umgebung von Teplá, Westböhmen Supervised by Dr. Gerhard Lehrberger (TUM)
1994 – 2003	Abitur (higher education entrance qualification) Gymnasium Dorfen, Germany
1990 – 1994	Elementary school Grund- und Teilhauptschule Moosen / Vils, Germany
Professional experiences	
Since 2012 2011 – 2012	Scientific staff (Section 3.2, Groundwater & Hydrogeology) Federal Institute for Geosciences and Natural Resources (BGR), Hannover, Germany
2006 – 2011	Student trainee for Hydrogeological Consulting - Sachverständigenbüro Prösl (SVB) Dr. Karl-Heinz Prösl, Hintelsberg, Germany
2009 – 2010	Internship at geothermal probe drilling company, GTB Erdbohrungen, Andi Schüpbach, Spiez, Switzerland
2003 – 2004	Alternative civilian service, BKK Taufkirchen / Vils, Germany Technical service, electrician & plumbing